UNIVERSITA' DEGLI STUDI DI PARMA

Dottorato di Ricerca in Fisica

Ciclo XXVIII

Vibrational dynamics and structure of natural feldspars

Coordinatore:
Chiar.mo Prof. Cristiano Viappiani

Tutor:
Chiar.mo Prof. Danilo Bersani
Chiar.mo Prof. Pier Paolo Lottici

Dottorando: Aliatis Irene

Grant information

The research reported in this thesis was financially supported by Fondazione Cariparma.

Stones are mute teachers; they silence the observer,

and the most valuable lesson we learn from them

we cannot communicate.

J. W. Goethe

Contents

List of Figures

List of Tables

1. INTRODUCTION

Feldspars (general formula MT_4O_8), together with pyroxenes (general formula $M2M1T_2O_6$), are the most abundant rock-forming minerals, and therefore they have a long history of scientific investigation into their physical properties and structure. Feldspars are the most common group of minerals in planetary crusts:

- on Earth they comprise ~60% of the total volume of the Earth's crust and occur in many types of metamorphic, igneous and sedimentary rocks. The whole spectrum of their possible structural states can be found in rocks with different cooling histories, providing an opportunity to study the way a structure responds to a changing geological environment;
- on the Moon, plagioclases ($(Na,Ca)Al(Al_xSi_{1-x})Si_2O_8$) are the most abundant minerals;
- feldspars are one of the main minerals in Martian meteorites and have been identified as a widespread component of basaltic rocks on the Martian surface.

Feldspars are one of the archetypical families of framework silicates, but at the same time they are among some of the most structurally complicated minerals. The structure of sanidine ($KAlSi_3O_8$), the aristotype of the feldspar group, was discovered in 1933 by Taylor[1].

Feldspars have several applications in industrial field: as a flux in the ceramic industry (in the manufacture of abrasives, floor tiles and pottery) and in the production of glass and enamels; as fillers in paints, coatings, plastics and rubber; as dating elements in Earth Sciences and Archaeology (K-Ar dating); for biomedical applications (as dental porcelains), as constituent of advanced

ceramic materials. Italy is the world largest producer of feldspars, with about 4,700,000 metric tons/year, which is 22.5% of worldwide production (based on British Geological Survey in 2011).

Although feldspars have been deeply studied and a great number of publications has been accumulated in the literature, some issues are still open. In particular, it was highlighted that different analytical techniques applied on feldspars (*e.g.*, optical microscopy, X-ray diffraction, Raman and infrared spectroscopies, scanning electron microscope equipped with X-ray microprobe) give sometimes inconsistent results. The lack of multianalytical approaches, especially in Cultural Heritage, could cause difficult diagnostics of ceramic objects and misunderstandings. Moreover, in the sedimentary petrography the identification of feldspars is still a crucial point.

The aim of this PhD thesis is to define the variation of the Raman spectra of Na-feldspar and plagioclases as function of pressure, the Al-Si degree of order and the chemical composition. The presence of phase transitions, joined to the variation in the degree of order and to the deformation in the tetrahedral framework, makes the interpretation of the Raman spectrum a hard issue, unless a detailed mineralogical and structural characterization of the studied mineral is performed. After a brief introduction on feldspars (Chapter 2), the attention has been focused on the careful characterization of the Raman and infrared vibrational modes of the Na-feldspar (Chapter 3), comparing the experimental and computational results with previous studies found in literature. Then, the variations of the Raman spectrum, when Na-feldspar is stressed by pressure (Chapter 4) and by change in the Al-Si distribution in the tetrahedral sites (Chapter 5), have been investigated. The final objective of this PhD research is the comprehensive study of the Raman features of plagioclase minerals (Chapter 6). Previous researches[2–4] succeeded in the determination of some Raman features-chemical composition relations only for the K-, Na- and Ca-end members and for the alkali solid solution. In this thesis has been made a further step, suggesting a protocol for the determination of the plagioclase chemical composition from its Raman characteristic features.

This thesis represents a small portion of the on-going work contributing to the interpretation of Raman data from the planetary missions, as ExoMars mission.

2. THE FELDSPAR STRUCTURE

Feldspars are alumosilicates (coordination 4, not 6 as in the aluminosilicates) with a wide compositional range. They are generally classified in two groups, according to their principal substitutional elements:

- the *alkali feldspars*, forming the solid solution from the Na-end member ($NaAlSi_3O_8$, albite) to the K-end member ($KAlSi_3O_8$, microcline, orthoclase, sanidine)
- the *plagioclase* solid solution, ranging from albite to anorthite ($CaAl_2Si_2O_8$).

Feldspars are characterized by a 3D framework of corner-sharing TO_4 tetrahedra. Their general formula is MT_4O_8, where M indicates low-charge balancing cations, such as Na^+, K^+, Ca^{2+}, Ba^{2+}, etc., which occupy the larger voids in the tetrahedral framework; T stands for silicon and aluminium, in the ratio 3:1 with monovalent M cation, or 2:2 with divalent M. Al and Si atoms are quite similar in size and bonding, so they form quasi perfect structures, when they randomly occupy the tetrahedral sites in disordered structures.

Many minerals and synthetic compounds fit this description, such as paracelsian and hexacelsian (both $BaAl_2Si_2O_8$, the first one monoclinic, the latter pseudoexagonal), slawsonite ($SrAl_2Si_2O_8$, monoclinic) or $RbAlSi_3O_8$ (pseudoexagonal), but they are not feldspars. Indeed, it is the particular topology of the linkage scheme that uniquely defines a feldspar.

2.1 The topology of the feldspars framework

The monoclinic C2/*m* feldspar structure is the aristotype of the family, from which all feldspathic low symmetry structures (*i.e.*, *I*2/*c*, $C\bar{1}$, $I\bar{1}$ and $P\bar{1}$) can be derived.

In 1928, Machatschki[5] proposed that the feldspar structure is based on a framework of linked TO_4 tetrahedra, but the true topology of the framework structure was envisaged by Taylor on Christmas Day, 1932, followed by a comprehensive survey of the structural variants[1]. He suggested a division of the unit cell of the sanidine structure into boxes by use of pseudotetragonal axes [100], [010] and [102]. Each box consists of four tetrahedra linked together in only one way for space group *C*2/*m*. K atoms are placed on mirror plane at reasonable bond distances to the oxygen atoms and the atomic coordinates are adjusted by trial-and-error to obtain agreement between observed and calculated X-ray diffraction intensities. The prototype positions for a sanidine, along with the labelling of the atoms inherited by the work of Taylor, are listed in Table 2.1.

Table 2.1: Atomic parameters of a sanidine. Data taken from Smith[6].

Atom	x	y	z	Point symmetry
$O_A(1)$	0	0.1472(6)	0	2
$O_A(2)$	0.6343(10)	0	0.2858(12)	m
O_B	0.8273(10)	0.1469(6)	0.2253(12)	1
O_C	0.0347(10)	0.3100(6)	0.2579(12)	1
O_D	0.1793(10)	0.1269(6)	0.4024(12)	1
T_1	0.0097(3)	0.1850(2)	0.2233(4)	1
T_2	0.7089(3)	0.1178(2)	0.3444(4)	1
M	0.2840(3)	0	0.1352(4)	m

The principal topological feature in feldspar is the occurrence of chains of tetrahedra, shaped like double crankshafts, cross-linked in a special way to form elliptical 8-membered rings of tetrahedra. It is of key importance, first because it allows a simple explanation of the anisotropy of the physical properties and secondly because the principal structural change caused by substitution of larger M cations by smaller ones is a shortening of the double crankshaft by crumpling[6]. The

idealized double crankshaft consists of four-membered rings alternately parallel and nearly perpendicular to *a*-axis (Figure 2.1).

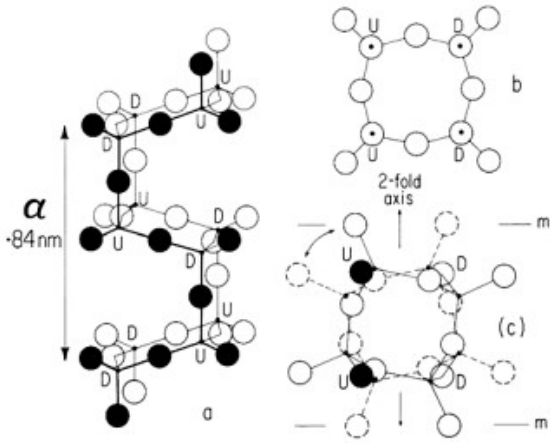

Figure 2.1: (a) The double crankshaft chain of the four-membered rings running parallel to the *a*-axis in all feldspars; (b) projection down the *a*-axis of an idealized crankshaft; (c) projection down the *a*-axis of a real crankshaft in sanidine showing the distortion of the crankshaft. Image taken from Smith[6].

Smith and Rinaldi[7] developed an algebraic code to describe the topological relations: a tetrahedron pointing up is denoted U and one pointing down is denoted D. The double crankshaft can be specified by the code UUDD with the understanding that each ring of type UUDD is bonded to rings DDUU by joining U of a lower ring to D of an upper ring. In real feldspars, the rings do not superimpose in projection along *a*, and a misfit is measured (*e.g.*, in sanidine there is a rotation of about 38° and a tilt from the *a*-axis (Figure 2.1)). Figure 2.2 shows how the feldspar structure can be described as a series of sheets composed of 4- and 8-membered rings of tetrahedra. There are two types of elliptical 8-rings: UUUUDDDD and DUUDUDDU. These combinations of U and D distinguish feldspars from other minerals, as paracelsian ($BaAl_2Si_2O_8$). Each sheet of tetrahedra lies parallel to the $(20\bar{1})$ plane and at angle of about 100° to the *a*-axis (~ the direction of the double crankshaft chains).

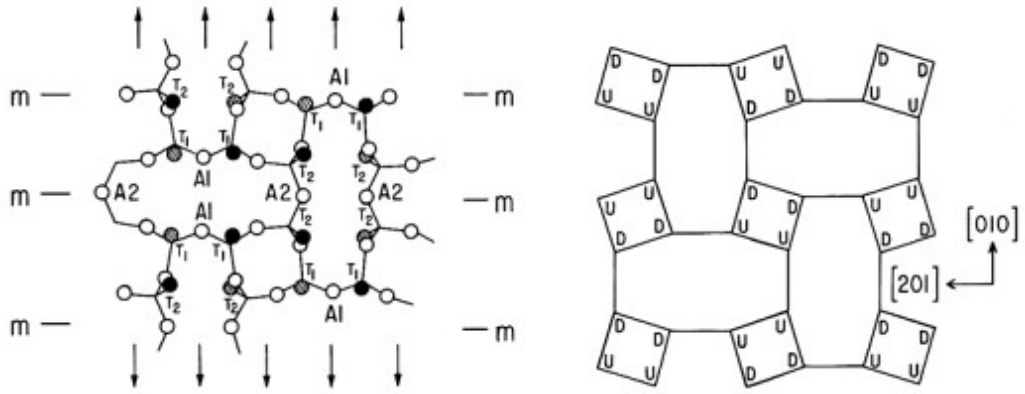

Figure 2.2: Nature of the sheets of tetrahedra lying perpendicular to the double crankshaft chains in feldspars. Image taken from Smith[6].

2.2 General features of feldspar structures

The monoclinic unit cell contains four formula units of MT_4O_8 (see Figure 2.3).

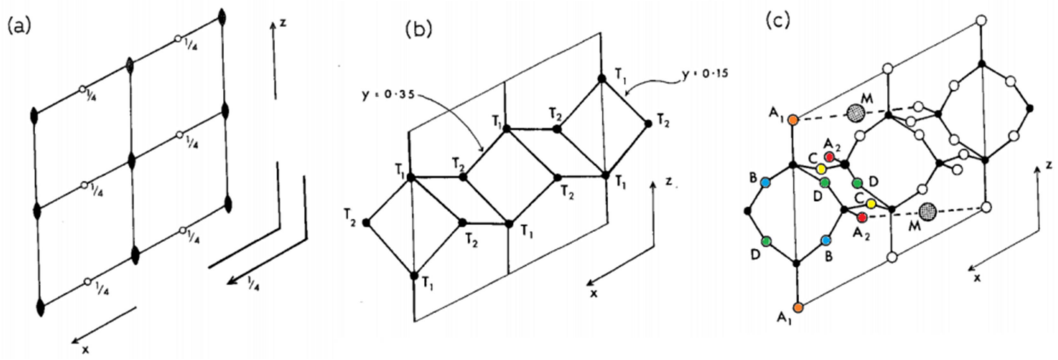

Figure 2.3: (010) projection of the aristotype unit-cell[8]. (a) Symmetry elements of the aristotype; (b) T atoms and linkage; (c) complete T-O framework and M cations.

The 16 T atoms are divided into two groups of 8, labelled as T_1 and T_2, because in the space group *C*2/*m* the general position of symmetry-equivalent atoms is 8-fold. The 32 O atoms are grouped in four sets of 8, labelled as O_A, O_B, O_C, O_D. In particular, O_A atoms form two sets of 4,

known as $O_A(1)$ and $O_A(2)$, because they lie in special positions: $O_A(1)$ on the diad axis and $O_A(2)$ on the mirror plane. The other three groups occupy general positions. The 4 M atoms lie in a 4-fold set of special positions on the mirror planes. The aforementioned nomenclature is taken from Taylor[1].

Table 2.2 lists the general features, such as chemical composition, approximate cell dimension, space group, topochemical symmetry, tetrahedral order, of the principal structures of feldspar end member compositions. The term *topochemical* symmetry describes the symmetry of the idealized framework when the chemical occupancy of the nodes is considered, in contrast to *topological* symmetry, which is used to describe the symmetry of the aluminosilicate framework when it is idealized into its most regular shape, obtained by displacements that preserve the topological relationships between nodes. The topochemical and topological symmetries must be identical for a fully disordered chemical distribution, but for an ordered one the topochemical symmetry may be lower than or equal to the topological symmetry. All feldspars have topological symmetry $C2/m$, but the topochemical symmetry is lowered to $C\bar{1}$ and $I2/c$ in the fully ordered varieties.

Table 2.2: *General features of common feldspars.*

Name	End member composition	Cell parameters						Space group	Topochemical symmetry	Tetrahedral order
		a	b	c	α	β	γ			
			(nm)			(°)				
Sanidine	$KAlSi_3O_8$	0.860	1.303	0.718	90.0	116.0	90.0	*C*2/*m*	*C*2/*m*	Disordered
Microcline	$KAlSi_3O_8$	0.859	1.297	0.722	90.6	115.9	87.7	$C\bar{1}$	$C\bar{1}$	Ordered
High albite	$NaAlSi_3O_8$	0.816	1.287	0.711	93.5	116.4	90.3	$C\bar{1}$	*C*2/*m*	Disordered
Low albite	$NaAlSi_3O_8$	0.814	1.279	0.716	94.3	116.6	87.7	$C\bar{1}$	$C\bar{1}$	Ordered
P-anorthite	$CaAl_2Si_2O_8$	0.818	1.288	1.417	93.2	115.8	91.2	$P\bar{1}$	*I*2/*c*	Ordered

2.2.1 Normal conventions applied to feldspars

In Figure 2.4, the bridging O anions within the ring, forming a square, are labelled as O_B and O_D. The apices of the T_1 tetrahedra that link the ring to other four-rings are $O_A(1)$ (to another T_1) and O_C (to a T_2). O_C and $O_A(2)$ atoms form the outer edge of the T_2 tetrahedra, with the $O_A(2)$ atoms forming the link to the T_2 tetrahedra of adjacent four-rings.

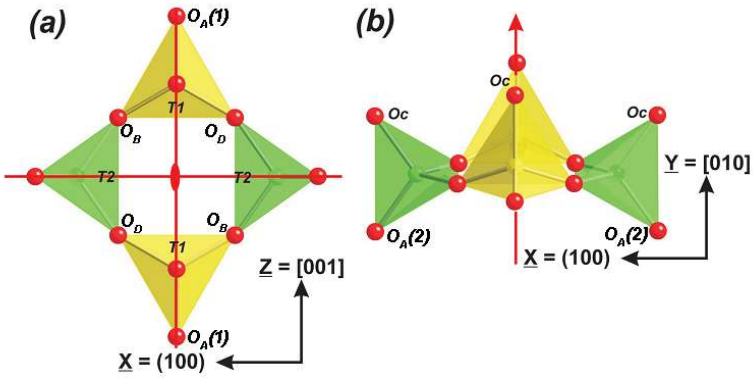

Figure 2.4: The atom labelling in feldspars[9].

2.3 Construction of the feldspar framework from tetrahedra

The basic building block of the feldspar structure is the four-membered ring of corner-sharing tetrahedra. A schematic building by steps, as suggested by Dr H. D. Megaw[8] in 1974, is proposed in the following (Figure 2.5.).

- *1st step*

  Making the approximation that all the tetrahedra are regular and identical in size, we can build a four-ring. We take four edges of different tetrahedra and form a square lying in (010) with them. Each tetrahedron T_1, related by the

diad axis, has a face lying in (010) and a vertex pointing upward from it, whereas each tetrahedron T_2 has an edge perpendicular to (010).

- *2nd step*

  The four-rings are joined together forming a folded chain, running parallel to [100], known as *crankshaft chain*. To make it, we have to take a four-ring, turn it upside down and slide it until its lower vertices coincide with the two upper vertices of the first ring. A T_1-T_2 join is formed. Repeating this operation, the crankshaft chain is build.

- *3rd step*

  Double the crankshaft chain: the mirror plane generates another crankshaft, above (or below) the first one, and connected to it by T_2-T_2 join. The double crankshaft chain is complete.

- *4th step*

  Finally, the *c*-translation on the crankshaft generates sheets of chains joined through $O_A(2)$ oxygens. Successive sheets are linked through $O_A(1)$ by T_1 tetrahedra pointing upwards and downwards along *c* direction.

- *5th step*

  Such a 3D framework has tetrahedral voids inside it. Monovalent or divalent M cations are placed in these cages. In an ideal structure, M has seven possible neighbouring atoms: one $O_A(2)$, two $O_A(1)$, two O_B and two O_D.

Summarizing, T_2 tetrahedra have bonds only within the sheets, connecting the double crankshaft chains, whereas T_1 tetrahedra link the sheets: each T_2 tetrahedron is therefore joined by one T_2 and three T_1 tetrahedra, and vice versa, each T_1 tetrahedron by one T_1 and three T_2 tetrahedra.

In real monoclinic feldspars, we have to add the two O_C atoms, which are brought nearer to M by the T_2 tilt (see Figure 2.5, *5th step*[8]). In all feldspars, the M-$O_A(2)$ distance is the shortest one. When the mirror plane is lost, as in the triclinic structure, the coordination number of M cation is reduced from 9 to 7.

1st step

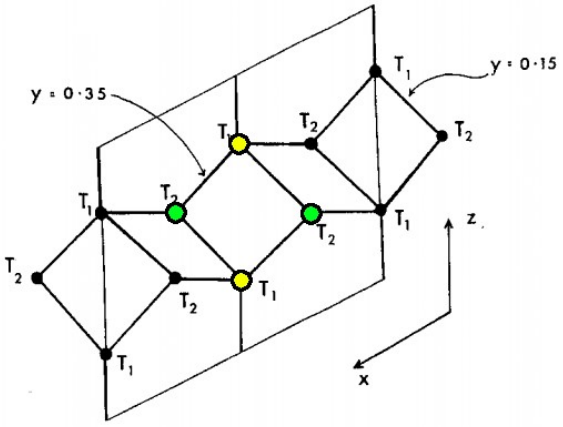

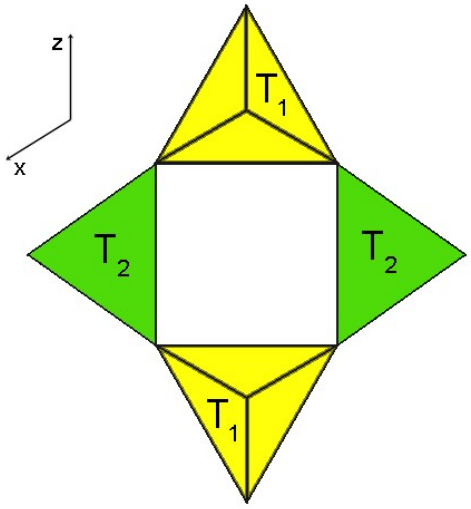

Image taken from Megaw[8].

2nd step

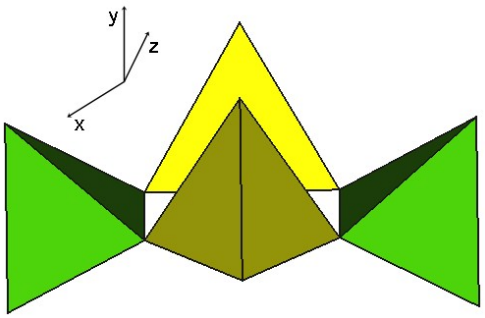

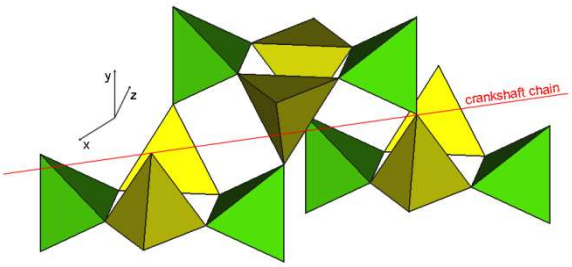

3rd step

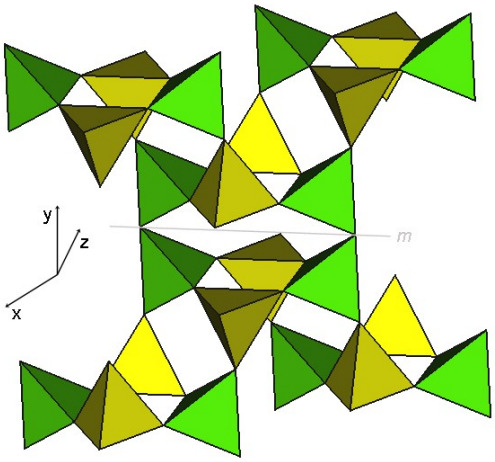

4th step

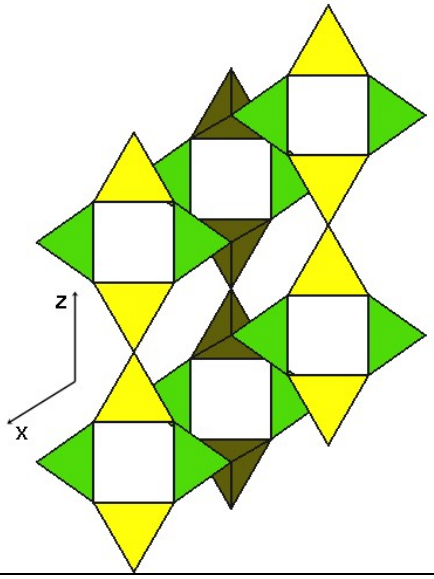

5th step

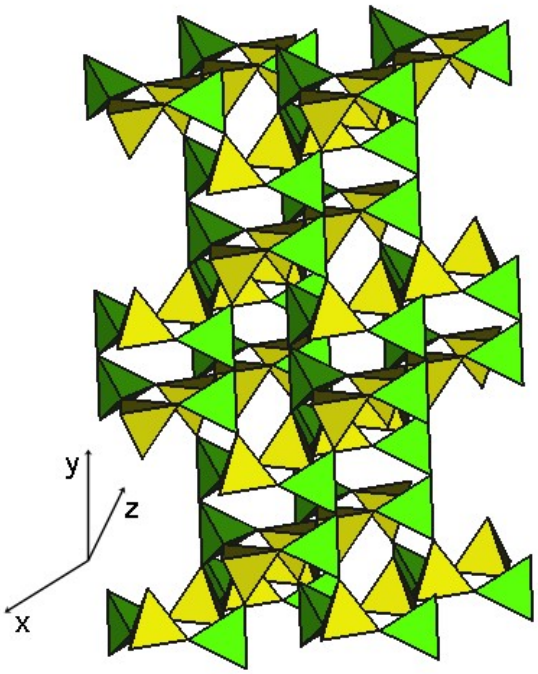

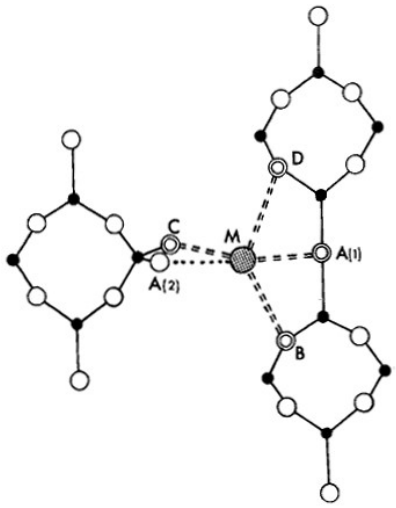

Image taken from Megaw[8].

Figure 2.5: Schematic building of the feldspar framework from tetrahedra by steps.

2.3.1 Calculation of an idealised cell

All the lattice parameters of an idealised feldspar structure can be calculated from the tetrahedron edge length l. The unit-cell parameters depend on the size of the tetrahedron and can be expressed as:

$$a = \left(2/\sqrt{3} + \sqrt{3}\right) l$$

$$d(100) = (1 + \sqrt{2})\, l$$

$$b = \left(3 + 2\sqrt{2/3}\right) l$$

$$c = (1 + \sqrt{3})\, l$$

$$\tan\beta = \frac{-(1 + \sqrt{2})}{(1 + 1/\sqrt{3})}$$

The unit-cell parameters can also be expressed in terms of the T-O bond length d, because $d = l\sqrt{3/8}$ for a regular tetrahedron. The volume of the monoclinic cell is given as a product $b \cdot c \cdot d(100)$. For an average T-O bond length of $AlSi_3$ feldspars, d = 1.6500 Å, corresponding to a tetrahedral edge-length l = 2.6944 Å, the estimated unit-cell distances are:

$$a = 7.77 \text{ Å}; b = 12.48 \text{ Å}; c = 7.36 \text{ Å}.$$

The β angle is independent of the size of the tetrahedra and is always equal to 123.159°. All the O-T-O bond angles have the ideal value of 109.47°, whereas the covalent character of the T-O bonds in framework silicates keeps the T-O-T angles generally in the range 130-150°. T-O-T bond angles are listed in Table 2.3 for an ideal monoclinic feldspar. The small value of T_2-$O_A(2)$-T_2 angle results in a simple tilting of the T_2 tetrahedra, which leads the $O_A(1)$-$O_A(1)$, O_B-O_B and O_D-O_D distances across the mirror plane being equal to the O-O distances that form the edges of the tetrahedra[9] (see Figure 2.6).

Table 2.3: T-O-T angles found in an ideal monoclinic feldspar.

T-O-T angle	Value (°)
T_1- $O_A(1)$ - T_1	141.06
T_2- $O_A(2)$ - T_2	109.47
T_1 - O_B - T_2	148.90
T_1 - O_C - T_2	144.73
T_1 - O_D - T_2	148.90

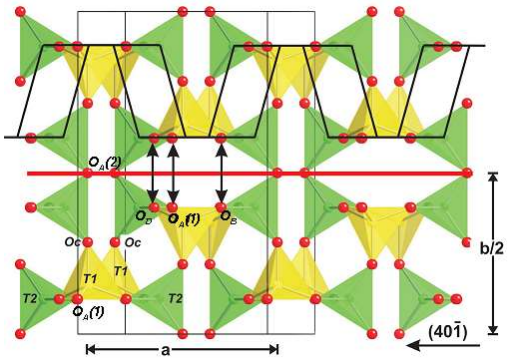

Figure 2.6: Framework of an ideal monoclinic feldspar, viewed down the [104] direction[9]. Black arrows indicate the short O-O distances across the mirror plane. Atoms of a four-membered ring are labelled as in (a) and (b) plots in Figure 2.4.

2.4 The distribution of Al and Si inside the T sites

Hitherto we have simply considered the monoclinic structure, without taking into account the Al-Si distribution inside each tetrahedron. Monovalent feldspars have an Al:Si ratio of 1:3, that means 4 Al atoms and 12 Si atoms in the unit-cell. For space group *C*2/*m*, both T_1 and T_2 sites need 8 equivalent atoms, but this symmetry request is not possible for an ordered distribution. Three possible solutions may be adopted by the structure and each can be found in feldspars[8]:

1) complete random distribution of Al and Si atoms in the T sites, keeping monoclinic symmetry;
2) different amounts of Al in the four T sites;
3) complete ordering of Al in one T site (*i.e.*, T_1(o) in an ideal ordered feldspar), reducing the symmetry to triclinic.

For the space group $C\bar{1}$, the general position of symmetry equivalent atoms is 4-fold. Each T site breaks up into two independent sets, labelled as "o" (*original*) and "m" (*mirror*, *i.e.*, having a near-mirror-plane relation to the original). In triclinic monovalent feldspars, T_1(o) is not symmetry-related to T_1(m), as T_2(o) and T_2(m); therefore they can have different occupancies by Al. Moreover, the Al-Si distribution has to satisfy the "aluminium avoidance rule", which forbids the corner-sharing of two Al-rich tetrahedra, because of the unfavourable energetic effect of Al occupying neighbouring tetrahedral sites. Conventionally, the average Al content of a tetrahedron, also called "Al site occupancy", is denoted with t_i, where t_i is the number of Al atoms occupying T_i tetrahedra divided by the number of tetrahedra. t_i ranges between 0 and 1. The average Si content is $1 - t_i$. In triclinic monovalent feldspars the proportion of each site, averaged over the whole structure, occupied by Al is designated as t_1(o), t_1(m), t_2(o) and t_2(m).

In divalent feldspars, the Al:Si ratio is 1:1. If we consider the previous monoclinic 7 Å unit-cell, the aforementioned rule prevents the expected Al distribution into T_1 and the Si distribution into T_2. To satisfy the "aluminium avoidance rule", Al and Si must regularly alternate throughout the structure, but to do this, a 14 Å *c*-spacing unit-cell must be used. The structure ceases to be *C*-face centred and becomes *I*-body centred. The comparison of a 7 Å and 14 Å unit-cells is drawn in Figure 2.7. The independent sets of atoms have new labels: T_1(o) splits into two new sets, known as T_1(oo) and T_1(oz). The name of the latter refers to a site derived from T_1(oo) by half a lattice

translation in the z direction, *i.e.*, $\frac{1}{2}c$. Similar splits occur for the other sets of sites. The new structure will have a *c*-glide plane, instead of a mirror plane. This means that $T_1(oo)$ and $T_1(mo)$ belong to independent sets, whereas $T_1(oo)$ and $T_1(mz)$ belong to the same symmetry-related set. In anorthite, $CaAl_2Si_2O_8$, and celsian, $BaAl_2Si_2O_8$, the ordered form is the normal one; incomplete disorder is produced by rapid quenching from high temperature.

The nomenclature of all the possible site positions was standardized by Megaw in 1954, starting from the work of Taylor.

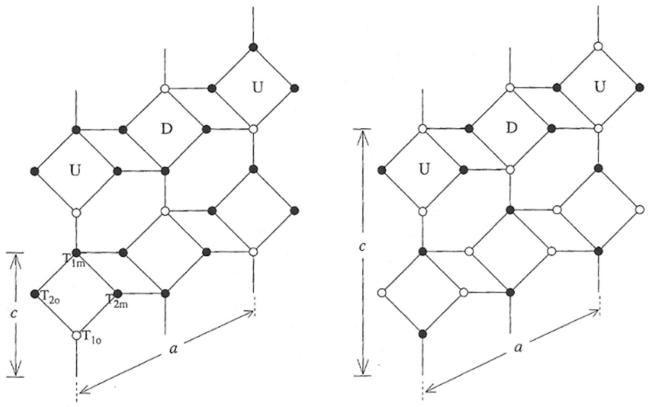

Figure 2.7: Schematic diagrams of linkage pattern of tetrahedra found in monovalent and divalent feldspars, respectively[10]. Black circles indicate Si, empty circles indicate Al.

2.5 The effect of the M cation size

The M cation is bonded to 5-11 neighbouring atoms depending on its effective size[11]. As shown in Table 2.4 and Figure 2.8, K^+ cation is larger enough to let nine oxygens atoms bond it, whereas it is not the case for Na^+ and Ca^{2+} cations. In triclinic structures, where the mirror plane is lost, one of the four O_B and O_D atoms moves appreciably away and brings the other three closer to M. This reduction from a three-point rather than a four-point influences more the geometry of the structure than does the Al-Si occupation; indeed, we could ignore the difference in size between Al and Si (*i.e.*, 0.67 Å and 0.54 Å, respectively).

Table 2.4: Ionic radii (Å) of the most common cations found in natural feldspars.

	K	Na	Ca
6-coordination	1.38	1.02	1.00
8-coordination	1.51	1.16	1.12

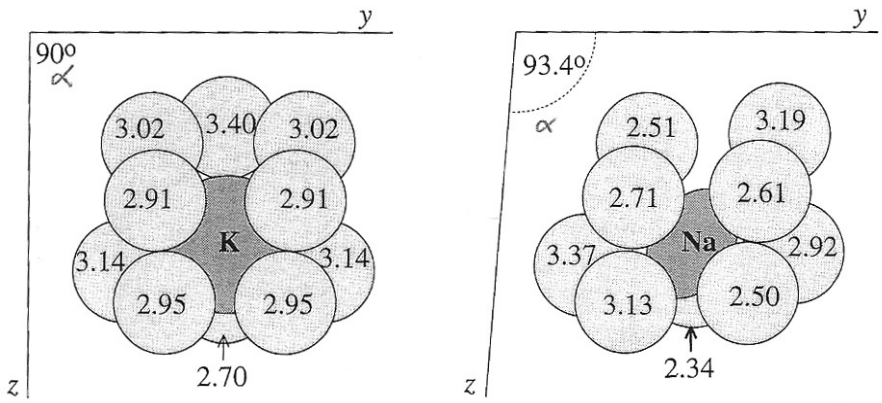

Figure 2.8: Drawing of the neighbouring atoms of K and Na cations from Putnis[10]. The number inside the atoms is the M-O distance (in Å).

2.6 Solid Solutions

In Figure 2.9 the two possible ternary representations of the most common feldspar compositions are shown.

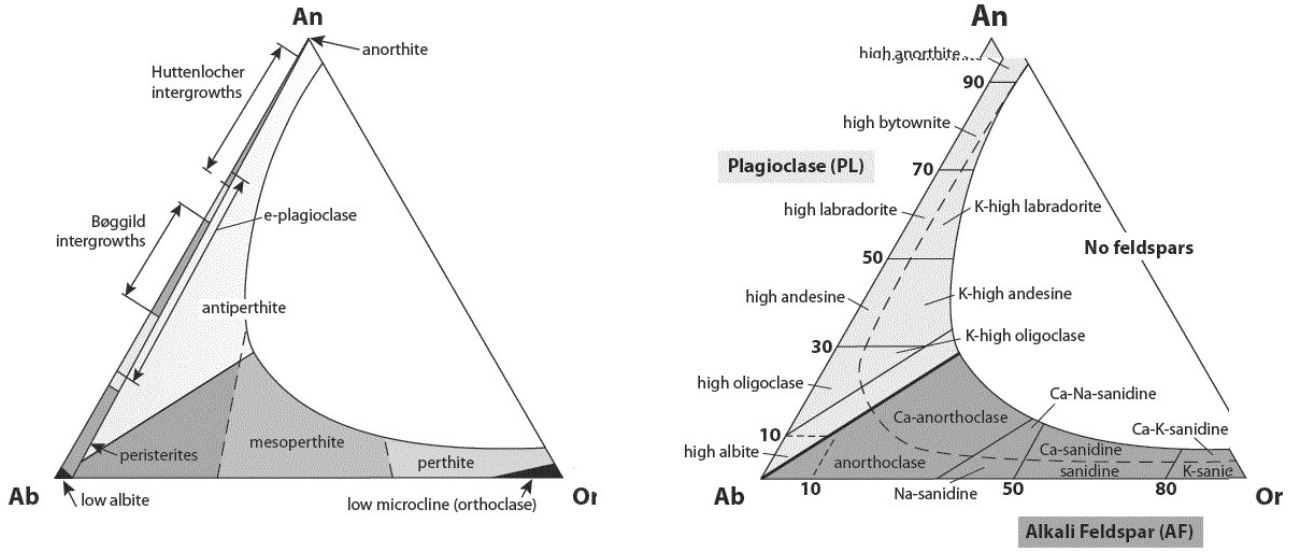

Figure 2.9: *LT* (*left*) and *HT* (*right*) ternary diagrams for feldspars, showing intergrowths and solid solutions.

2.6.1 Alkali-feldspars

The structures of the alkali-feldspars consist of a framework of 3D linked (Si,A)-O tetrahedra, whose interstices are occupied by Na and K ions. The distribution of Si and Al can ideally be fully ordered or have varying degrees of disorder, but their over-all ratio is Si_3Al. The symmetry of most alkali feldspars is triclinic, but those of high temperature origin (sanidines, monoalbites) can be monoclinic. Therefore, the characterization of an alkali feldspar requires specification of its chemical composition, the symmetry of the structure and the extent to which Al and Si occupy the available tetrahedral sites (T) in an ordered or disordered manner[12]. The nomenclature, symmetry and Al distributions for end members and near end members compositions are set out in Table 2.5 and Table 2.6.

Table 2.5: Oder-disorder and nomenclature of Na-feldspars.

Nomenclature	Space group	Al distribution (ti)
Monoalbite	*C*2/*m*	$2t_1 = 2t_2 = 0.5$ (*full disorder*)
Analbite	$C\bar{1}$	$t_1(o) = t_1(m) = t_2(o) = t_2(m) = 0.25$ (*full order*) *or* $t_1(o) = t_1(m) > t_2(o) = t_2(m)$ (*partial order*)
High Albite	$C\bar{1}$	$t_1(o) > t_1(m) > t_2(o) = t_2(m)$ (*high disorder*)
Intermediate Albite	$C\bar{1}$	$t_1(o) > t_1(m) = t_2(o) = t_2(m)$
Low Albite	$C\bar{1}$	$t_1(o) = 1.0$, $t_1(m) = t_2(o) = t_2(m) = 0$ (*full order*)

Table 2.6: Oder-disorder and nomenclature of K-feldspars.

Nomenclature	Space group	Al distribution (t_i)
High Sanidine	*C*2/*m*	0.5 (*full disorder*) < $2t_1$< 0.66*
Low Sanidine	*C*2/*m*	0.667 < $2t_1$ < 0.74*
Orthoclase	*C*2/*m*	0.74 < $2t_1$< 1.0*
Intermediate Microcline	$C\bar{1}$	$t_1(o) > t_1(m) > t_2(o) = t_2(m)$
Low Microcline	$C\bar{1}$	$t_1(o) = 1.0$, $t_1(m) = t_2(o) = t_2(m) = 0$ (*full order*)

* Limits suggested by Ribbe[13].

At composition $NaAlSi_3O_8$, increasing temperature and disorder is followed by the sequence: low albite (LA) → intermediate albite (IA) → high albite (HA) (all triclinic $C\bar{1}$), and then by transition to monoalbite (MA, monoclinic *C*2/*m*). The term analbite (AA) is used for the high-temperature Na-feldspar, topochemically monoclinic ($t_1(o) = t_1(m)$), but still topologically triclinic, which inverts to monoalbite on heating.

At composition $KAlSi_3O_8$, the corresponding sequence is: low microcline (LM, triclinic $C\bar{1}$) → low sanidine (LS) → high sanidine (HS) (both monoclinic $C2/m$).

At low temperatures there is little solid solution between the Na and K end members (Figure 2.10). Bulk compositions lying between are therefore represented by intergrowth of two components, known as *perthites*, *microperthites* or *cryptoperthites* (the terms describe the scale of intergrowth: *i.e.*, if they are visible by naked eye, under a microscope or are sub-microscopic)[12]. At high temperatures (T > 600 °C) there is solid solution between high albite and sanidine.

In completely disordered alkali feldspar, since there are 3 Si and 1 Al in the formula unit, $t_1(o) = t_1(m) = t_2(o) = t_2(m) = 0.25$ (triclinic) and $2t_1 = 2t_2 = 0.5$ (monoclinic). In a completely ordered triclinic feldspar, with all of its Al in $T_1(o)$, $t_1(o) = 1.0$ and $t_1(m) = t_2(o) = t_2(m) = 0$. In a fully ordered monoclinic alkali feldspar, because there cannot be more than one Al per four T sites ($AlSi_3$), the maximum content of either T_1 or $T_2 = 0.5$ ($2t_i = 1.0$) and the other t value would be zero.

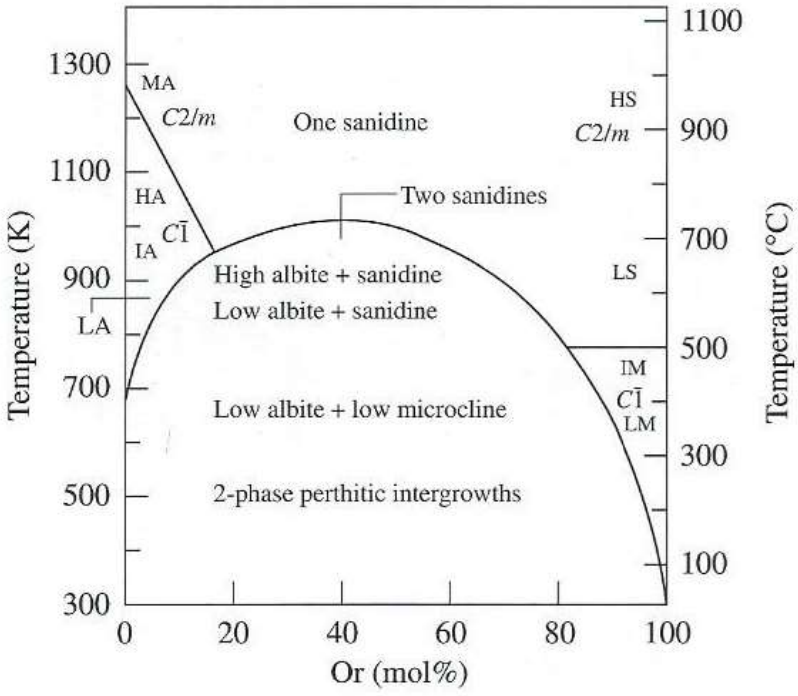

Figure 2.10: *T-X* diagram from Deer *et al.*[12] for Na-K alkali feldspars showing possible equilibrium relationships, nomenclature and space groups of the various phases.

2.6.2 Plagioclases

Plagioclases can be described as a solid solution ranging from the Na-endmember, albite ($NaAlSi_3O_8$), to the Ca-endmember, anorthite ($CaAl_2Si_2O_8$), in which the Si:Al ratio varies. A common formula to depict easily their chemical composition is Ab_xAn_{100-x}. On the basis of the anorthite content x ("An_x" in the following), plagioclases are generally classified as: *albite* (An_0-An_{10}), *oligoclase* (An_{10}-An_{30}), *andesine* (An_{30}-An_{50}), *labradorite* (An_{50}-An_{70}), *bytownite* (An_{70}-An_{90}) and *anorthite* (An_{90}-An_{100}). The complete solid solution is obtained only above 650 °C[10,14].

High-temperature plagioclases occur in some volcanic rocks, while low-temperature plagioclases are mostly found in igneous and metamorphic rocks and occur in sediments both as primary and authigenic minerals.

All plagioclases have similar tetrahedral linkage pattern, which may undergo different kinds of distortions and hence lower the symmetry. In particular, the Na-Ca substitution in the tetrahedral framework of plagioclases is fast, whereas the Al-Si substitution in the tetrahedral sites is extremely difficult, because the internal atom is highly bonded with the surrounding oxygens. The variation in the Al-Si content causes the change of the ordering scheme of the structure.

Plagioclases show a very complex mixing behaviour because of the various compositional-driven phase transitions and the Al-Si order/disorder reactions. They exhibit triclinic symmetry $\bar{1}$, but the space group and the unit cell change according to composition and cooling rate[15,16]. Natural Ab-rich plagioclases exhibit the average $C\bar{1}$ structure with no Al-Si order (*i.e.* the high albite structure), whereas on the anorthite-rich side (from ~An_{50} up to An_{90}) the structures have $I\bar{1}$ average symmetry, due to the increasing tendency to order Al and Si atoms as the Al:Si ratio approaches to 1. The complete order with strictly alternating Al-Si is achieved only in pure anorthite ($P\bar{1}$). The "aluminium avoidance rule" forbids the Al occupancy in adjacent tetrahedra, being energetically unfavourable, so framework structures with Si:Al ~ 1 have to be heated at very high temperatures before total disorder occurs (in pure anorthite, the disordering temperature is estimated higher than 2000 °C).

At low temperatures, the plagioclase solid solution contains three different ordered structures: low albite, the intermediate or "*e* structure" (the e_2 and e_1 incommensurate phases) and

anorthite[16]. Moreover, there are three miscibility gaps in the plagioclase system, associated with breaks in the ordering behaviour as a function of composition:

- the *peristerite (Pe)* gap, between composition of $An_{\sim 0}$ and $An_{\sim 25}$ (e_2 structure);
- the *Bøgglid (Bø)* gap, with two kinds of *e* structures (*i.e.*, e_1 and e_2) occurring at the labradorite composition (An_{40}-An_{60});
- the *Huttenlocher (Hu)* gap, showing lamellar intergrowths with composition between An_{65} (e_1 structure) and An_{95} (*I*-anorthite structure).

Incommensurate structures giving diffuse *e* reflections have been observed in pure anorthite produced experimentally from glasses[17], suggesting that the Ca-Na partitioning is not of primary importance in *e* plagioclases, but that Al-Si ordering and elastic effects are the controlling factors.

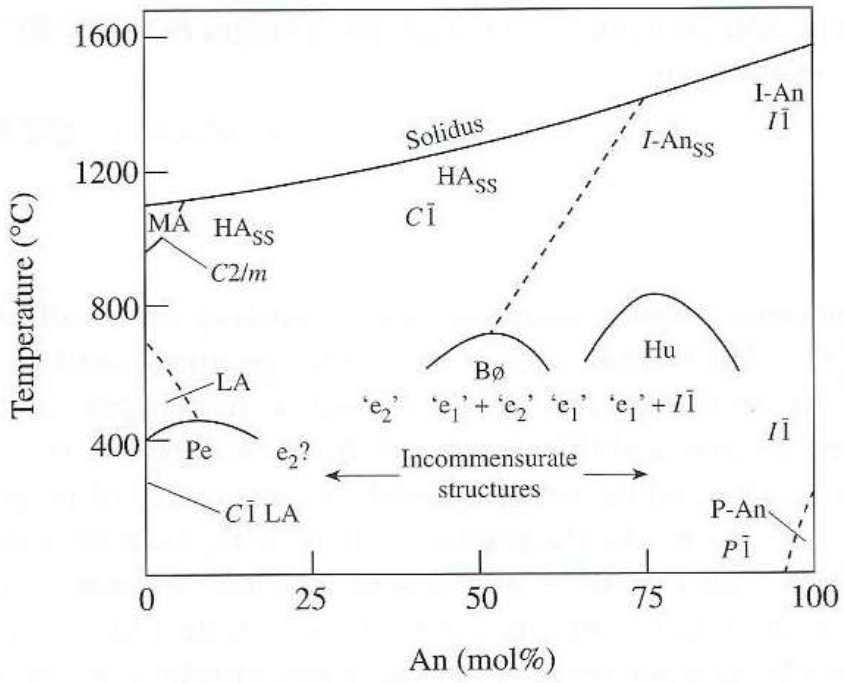

Figure 2.11: *T-X* diagram for plagioclase from Deer *et al.*[12]. "ss" stands for solid solution.

3. THE REVISED RAMAN and INFRARED SPECTRA OF LOW ALBITE

Albite is one of the most common minerals in the Earth's crust, and its polymorphs can be found in rocks with different cooling histories. It is found widely in greenschist facies metamorphic rocks; in igneous rocks, it occurs principally in pegmatites and in alkali-rich rocks, such as nepheline, syenites and other feldspathoidal types. Albite is a common constituent of ceramic objects, both modern and archaeological. It is used as flux in glazes to lower the high melting point of the glass former silica and in clay bodies to limit and control the amount of glass, which works to cement crystalline components together. It is employed in gemmology, as colourless gem, or it can be treated by irradiation to turn its colour into blue, green or black, if lead and water impurities are present.

The mineral was named *albite*, from the Latin word "albus", white, in 1815 by Johan Gottlieb Gahn and Jöns Jacob Berzelius, because its usual colour is pure white. It is the sodic endmember of both alkali and plagioclase solid solutions.

Albite occurs in rocks mainly as low albite (LA), where all Al atoms occupy the $T_1(o)$ tetrahedra. This is because albite is most common in slowly cooled rocks, where cooling time is long enough to allow a complete ordering of feldspars[18]. Albite crystallizes with triclinic pinacoidal forms. It shows generally tabular (*e.g.*, pericline) or platy crystals (*e.g.*, cleavelandite variety). It can be often found as fine parallel segregations alternating with pink microcline in perthite as a result of

exolution on cooling. Common twinning is around [010] or perpendicular {010}, giving polysynthetic striae on {001} or {010}[19]. The cleavage is perfect on {001}, good on {010} and imperfect on {110}. Its specific gravity is about 2.6-2.65 g/cm^3 and it has a Mohs hardness of 6-6.5. Its colour can vary from colourless to white or grey, bluish, greenish and reddish and it has vitreous lustre.

In this chapter, Raman and infrared frequencies of low albite will be studied and compared to those calculated at the hybrid Hartree–Fock/density functional theory (HF/DFT) level. The WC1LYP Hamiltonian has been employed in the calculation, as it has proven to give excellent agreement between theoretical and experimental vibrational wavenumbers and intensities in silicate minerals, such as beryl[20], lizardite[21], diopside[22], jadeite[23] and grossular[24]. For clarity, the Raman and infrared spectra will be discussed separately. Part of this work was published in I. Aliatis, E. Lambruschi, L. Mantovani, D. Bersani, S. Andò, G. D. Gatta, P. Gentile, E. Salvioli-Mariani, M. Prencipe, M. Tribaudino, and P. P. Lottici, *A comparison between ab initio calculated and measured Raman spectrum of triclinic albite ($NaAlSi_3O_8$)*, Journal of Raman Spectroscopy (2015), 46: 501-508 [25].

3.1 Selection of a natural sample of low albite

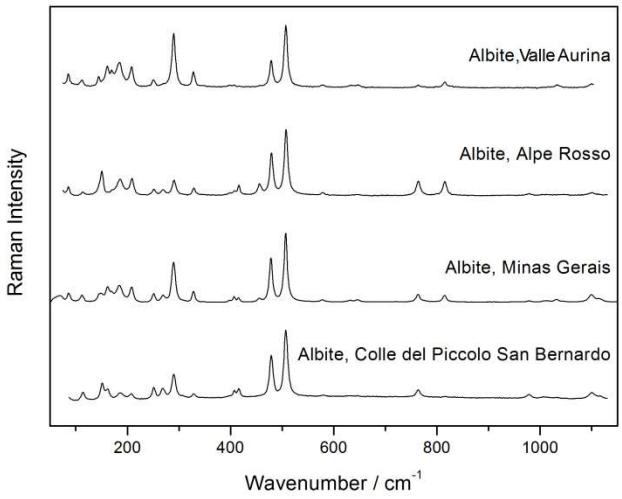

Figure 3.1: Raman spectra collected on different albite samples.

Several Raman spectra have been collected on different albites, in order to find the one most similar to the ideal Na-endmember used in the calculation. In Figure 3.1, some of the Raman spectra are displayed (*i.e.*, an albite from Colle del Piccolo San Bernardo, an albite from Minas Gerais (cleavelandite variety), an albite from Alpe Rosso and an albite from Valle Aurina (pericline variety)).

The albite from Minas Gerais was selected as reference. The cleavelandite variety is characterized by well crystallized platy crystals, twinned on (010). Because of its large crystals, the perfect cleavage on (010) face and the clearly visible striae, the orientation of crystal under the microscope of the Raman spectrometer is easier and more reproducible than the other candidates. Chemical analyses indicate an almost end member composition ($K_{0.02}$,$Na_{0.97}$)$Ca_{0.009}Al_{1.01}Si_{2.99}O_8$) and unit cell parameters (a = 8.1395(5) Å, b = 12.7838(7) Å, c = 7.1597(6) Å, α = 94.242(6)°, β = 116.590(7)°, γ = 87.674(5)°, V = 664.35(9) $Å^3$) agree very well with those of an ideal albite. For more detailed data about chemistry and structure about this sample see Appendix A and Appendix B .

3.2 Description of the experimental setups

3.2.1 The Raman measurements

Raman spectra have been collected by a Horiba Jobin-Yvon LabRAM apparatus in backscattering geometry. The spectrometer (300 mm focal length) is equipped with an Olympus BX40 confocal microscope with objectives up to 100× and a motorized x–y stage. A He–Ne laser at 632.8 nm (maximum power of 20 mW) or a Nd:YAG laser at 473.1 nm (maximum power of 100 mW) can be used for excitation. The power on the sample can be limited by a set of neutral density filters. The Rayleigh radiation is blocked by reflective volume Bragg grating notch filters (BragGrateTM by OptiGrate), which enable Raman measurements down to 5-10 cm^{-1} from the laser

line. The backscattered Raman light is dispersed by a 1800-groove/mm holographic grating onto a Peltier cooled CCD (1024 × 256 pixels). The entrance slit width can be set between 900 and 50 μm.

For these measurements, the He–Ne laser was used for excitation. The entrance slit width was fixed at 150 μm. Samples were mounted on a backlash-free goniometer stage (accuracy of 0.5°) and oriented under the 50× ultralong working distance (ULWD) objective (numerical aperture (NA) = 0.55, working distance (WD) = 8 mm and lateral spatial resolution ~ 2 μm).

Unpolarized Stokes and anti-Stokes Raman spectra have been collected on loose crystals of low albite, previously crushed and milled in a mortar. Due to the cleavelandite shape, the powdered sample behaves as micas and the majority of the crystals orient on the (010) faces.

Polarized Stokes Raman spectra have been measured on the (010), (001) and ~(100) crystallographic faces of a well-formed crystal. All the selected faces have not been properly cut, but they are natural faces of the crystal. For this reason, the real (100) face is not visible, and a face cutting the *a* axis has been chosen for the measurement and labelled as ~(100) (Figure 3.2).

The crystal was oriented under the microscope as follows:

• (010) face: the incident beam polarization was made to correspond to the *a* crystallographic axis, which is easily recognizable as the cleavage traces on this face are parallel to *a* axis;

• (001) face: the *a* crystallographic axis is parallel to the edge between (010) and (001) faces. The laser polarization was made again to coincide with the *a* axis;

• ~(100) face: the incident beam is approximately along the *a* axis; hence, the laser polarization was made to correspond with the *b* axis.

The orientation angles were measured from the laser polarization direction. On each face, measurements were collected at $\theta = 0°$ and $\theta = 90°$. Directional Raman measurements have been collected in parallel and cross polarizations, to get the diagonal (XX, YY, ZZ) and off diagonal (XY, XZ, YZ) elements of the Raman tensor, respectively.

Typical exposures of the Raman measurements were 60–180 s, repeated three to six times. The scattered light polarization was controlled by means of polarizing filters with efficiency better than 97 %. The acquisition time for crossed polarization was determined to take into account the polarization dependent response of the diffraction gratings. The correction was calculated by measuring the known depolarization ratio of the CCl_4 molecule.

The system was calibrated on the silicon Raman peak at 520.6 cm^{-1}. Spectra were collected in the range of 50–1200 cm^{-1} with a spectral resolution of about 1.5 cm^{-1}. The baseline subtraction with a second degree polynomial curve and the peak fitting were made with LABSPEC 5.78.24 software package, Jobin Yvon/Horiba, subdividing each spectrum in four spectral ranges.

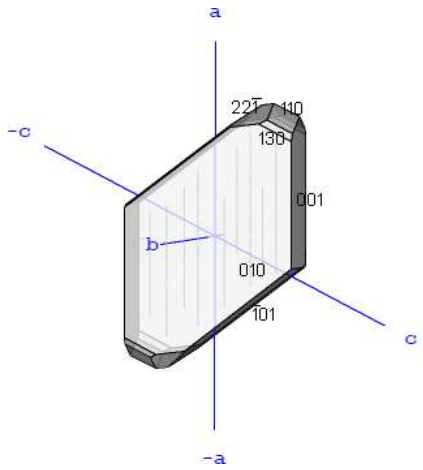

Figure 3.2: A schematic crystallographic picture of albite. Image taken from Goldschmidt[26].

3.2.2 The infrared absorption measurements

Infrared absorption spectra have been obtained by means of a high resolution Fourier Transform spectrometer BOMEM DA8 on albite crystals from Minas Gerais. Measurements have been performed by A. Baraldi (DIFEST Department, University of Parma). The sample was crushed and milled in an agate mortar. Two type of pellets were used for different frequency ranges: albite polycrystalline powder was diluted in CsI pellet (7.5 mg $NaAlSi_3O_8$ and 113 mg CsI) for the 100-6000 cm^{-1} spectral range, whereas it was loaded between two thin polyethylene foils and pressed together for the 40-200 cm^{-1} range. A CsI pellet (120 mg) was used as reference. Two IR sources were employed: a Globar (200-10000 cm^{-1}) and a Hg-arc lamp (5-200 cm^{-1}); and different beam splitters: KBr (450-10000 cm^{-1}), Mylar 3 μm (125-850 cm^{-1}), Mylar 6 μm (75-450 cm^{-1}) and Mylar 12 μm (40-200 cm^{-1}). Spectra were collected using a liquid nitrogen cooled MCT detector for the

500-6000 cm^{-1} spectral range and a room temperature DTGS detector for the 40-700 cm^{-1} range. Spectra have been recorded at 9 and 298 K. For low temperature measurements, the sample was assembled in a 21SC model Cryodine Cryocooler of CTI-Cryogenics. All the experimental details used are summarized in Table 3.1.

The spectral resolution was set to 1 cm^{-1}. Each spectrum was calculated by Fourier transformation of 2000 interferometer scans. All spectra were recorded as absorbance A, with $A = -\log_{10}(I_{sample}/I_{reference})$, where I is the single-beam transmission intensity. Profile analysis of the spectra was performed by fitting of Lorentzian peak profiles (LABSPEC 5.78.24 software package).

Table 3.1: Experimental details for the various infrared absorption measurements.

Reference	Temperature (K)	Source	Beam splitter	Detector	IR Region (cm^{-1})
Polyethylene	298	Hg arc	Mylar 12 μm	DTGS	40-200
CsI	298	Hg arc	Mylar 12 μm	DTGS	120-230
CsI	298	Globar	Mylar 12 μm	DTGS	120-370
CsI	298	Globar	Mylar 6 μm	DTGS	220-450
CsI	298	Globar	Mylar 3 μm	DTGS	220-700
CsI	298	Globar	KBr	MCT	500-6000
CsI	9	Globar	KBr	MCT	500-6000

3.3 Brief background of the computational method

Geometry optimization and spectral calculations on low albite were performed by M. Prencipe (University of Torino), by means of the *ab initio* CRYSTAL14 program[27], which employs an *all electron* Gaussian-type basis set. Computations were made at the hybrid Hartree–Fock/Density Functional Theory (HF/DFT) level employing the WC1LYP exchange–correlation functional. The latter is based on the relatively new DFT Generalized Gradient Approximation (GGA) exchange functional proposed by Wu and Cohen[28], mixed to the exact nonlocal HF exchange (16%) and coupled with Lee-Young-Parr correlation functional of Lee *et al*.[29]. The HF exchange is added in order to correct for the self-interaction error, *i.e.*, the interaction of an electron with itself, which is typical of purely DFT local density approximation (LCA) or GGA functionals. Although not being extensively tested, the WC1LYP Hamiltonian proved to be very successful in the reproduction of elastic and vibrational properties of minerals.

The atomic basis set employed consists of a 8-511G(1d) for Na, 8-511G(1d) for Al, 88-31G(2d) for Si and 8-411G(2d) for O, where the symbols 1d and 2d stand for the presence of one and two polarization functions, respectively. They are derived from the CRYSTAL online library (www.crystal.unito.it/basis-sets.php). Such basis sets have been chosen as being successfully employed in previous calculations of structure and properties of silicates; in particular, the same basis sets were used for the calculation of the Raman spectrum of jadeite ($NaAlSi_2O_6$)[23].

The DFT exchange and correlation contributions to the total energy have been evaluated by numerical integration, over the cell volume, of the appropriate functionals; a pruned 991454 grid, consisting of 99 radial points and 1454 angular points in the region of interest has been used (XXLGRID of the CRYSTAL14 user manual[27]). Such a grid corresponds to a total of 631097 points in the primitive unit cell. A measure of the excellent numerical accuracy provided by such a grid is the evaluation of the total number of electrons in the unit cell, by the numerical integration of the electron density over the cell volume: 259.999995 electrons out of 260. The thresholds controlling the accuracy of the calculation of Coulomb and exchange integrals were set to 8 (ITOL1 to ITOL4[27]) and 18 (ITOL5[27]). The diagonalization of the Hamiltonian matrix was performed at 36 independent **k** vectors in the reciprocal space (Monkhorst net[30]), by setting to 4 the shrinking factor (IS parameter[27]).

Cell parameters and fractional coordinates have been optimized by analytical gradient methods, as implemented in CRYSTAL14[27,31]. Geometry optimization was considered converged when each component of the gradient (TOLDEG parameter[27]) was smaller than 0.00003 hartree/bohr and displacements (TOLDEX[27]) were smaller than 0.00012 bohr with respect to the previous step. The calculated equilibrium lattice parameters, optimized at the WC1LYP level, without zero point and thermal effects included, are reported in Table 3.2 (static values, *column a*). Zero point and thermal pressures at 300 K and their impact on the calculated structure of low albite have been estimated by calculating the full vibrational spectrum at the Γ point at different unit cell volumes, according to the procedure described by Prencipe *et al.*[32]. Cell parameters at 300 K are reported in Table 3.2 (*column b*). The calculation also provided an estimation for the bulk modulus K_0 of low albite of 54.1 GPa at 300 K ($\partial K_0/\partial P = K' = 6.4$), from the fit of a third-order Birch-Murnaghan[33] equation of state to the computed pressure–volume data in the 0-7 GPa pressure range. These elastic parameters are in excellent agreement with the experimental findings of Benusa *et al.*[34], who reported a K_0 of 54.2(7) GPa and K' = 5.3(6), at least in the low pressure range. As usual with DFT calculations at the GGA level, even in the case of hybrid functionals like WC1LYP, the cell parameters and volumes are somewhat overestimated with respect to the experimental data (see Table 3.2).

Table 3.2: Comparison between low albite experimental and calculated unit-cell parameters at 0 K (a) and 300 K (b). Calculated (b) vs experimental % differences are reported. Table published in Aliatis *et al.*[25].

	Experimental	Calculated		% Differences
		(a)	(b)	
a (Å)	8.1395(5)	8.1745	8.2199	1.0
b (Å)	12.7838(7)	12.8510	12.8604	0.6
c (Å)	7.1597(6)	7.2075	7.2136	0.8
α (°)	94.242(6)	94.306	94.278	0.04
β (°)	116.590(7)	116.775	116.547	-0.04
γ (°)	87.674(5)	87.791	87.646	-0.03
V (Å^3)	664.35(9)	674.06	680.23	2.4

The optimized structure at the cell volume of 680.23 Å^3 (Table 3.2, *column b*), corresponding to the calculated geometry of low albite at 300 K, is the one employed in the

calculation of the vibrational modes. Vibrational wavenumbers and normal modes have been calculated within the limit of the harmonic approximation, by diagonalizing a mass weighted Hessian matrix[35], whose elements are the second derivatives of the full potential of the crystal with respect to mass-weighted atomic displacements. Relative intensities of the Raman and infrared signals are computed using fully analytical approaches[36,37], formulated and implemented in the CRYSTAL14 program. The Raman intensities are calculated under the Placzeck approximation. Non-resonant Raman intensity for an oriented single crystal (consider, for instance the XY directions) associated with the mode of wavenumber ω_i is:

$$I_{xy}^{i} \propto C\left(\alpha_{xy}^{i}\right)^2$$

where $\alpha_{xy}^{i}$is the XY element of the Raman tensor for the *i*-th mode; the prefactor *C* depends on the laser frequency ω_L and temperature *T* as follows:

$$C \sim \frac{1+n(\omega_i)}{\omega_i}(\omega_L-\omega_i)^4$$

where the Bose occupancy factor $n(\omega_i, T)$ is given by:

$$n(\omega_i, T) = \frac{1}{e^{\hbar\omega_i/kT}-1}.$$

For a powder, the integral intensity is averaged over the possible directions of crystallites:

$$G_i^{(0)} = 1/3\,(\alpha_{ixx}+\alpha_{iyy}+\alpha_{izz})^2$$

$$G_i^{(1)} = 1/2\left[\left(\alpha_{xy}^{i}-\alpha_{yx}^{i}\right)^2+\left(\alpha_{xz}^{i}-\alpha_{zx}^{i}\right)^2+\left(\alpha_{zy}^{i}-\alpha_{yz}^{i}\right)^2\right]$$

$$G_i^{(2)} = 1/2\left[\left(\alpha_{xy}^{i}+\alpha_{yx}^{i}\right)^2+\left(\alpha_{xz}^{i}+\alpha_{zx}^{i}\right)^2+\left(\alpha_{zy}^{i}+\alpha_{yz}^{i}\right)^2\right] + 1/3\left[\left(\alpha_{xx}^{i}-\alpha_{yy}^{i}\right)^2+\left(\alpha_{xx}^{i}-\alpha_{zz}^{i}\right)^2+\left(\alpha_{yy}^{i}-\alpha_{zz}^{i}\right)^2\right].$$

For the 90° and backscattering geometries, a laser beam and a scattered radiation analyser in use, the intensity for the powder can be expressed as:

$$I_{i\parallel}^{powder} \sim (\omega_L-\omega_i)^4\frac{1+n(\omega_i)}{\omega_i}\left[10G_i^{(0)}+4G_i^{(2)}\right]$$

$$I_{i\perp}^{powder} \sim (\omega_L-\omega_i)^4\frac{1+n(\omega_i)}{\omega_i}\left[5G_i^{(1)}+3G_i^{(2)}\right]$$

$$I_{iTOT}^{powder} = I_{i\parallel}^{powder} + I_{i\perp}^{powder}$$

where subscripts ∥ and ⊥ correspond to the polarized and depolarized light, respectively.

The computed Raman intensities refer to the experimental conditions T = 300 K, P = 1 atm and λ = 632.8 nm, as laser excitation line. All values have been normalized to the most intense peak.

The integrated IR intensity for the *p*-th mode, in units of Km/mol, is computed, under the hypothesis of isotropic response (*i.e.*, powder sample), according to:

$$I_p = \frac{\pi}{3}\frac{N_A}{c^2} d_p \left|\vec{Z}_p\right|^2$$

where N_A is the Avogadro's number, c is the speed of light, d_p is the degeneracy of the mode, $\vec{Z}_p$ is the mass-weighted effective mode Born charge vector.

The attribution of each mode to a pattern of motion of the atoms of the structure has been made by direct inspection of the eigenvectors and their components, on the basis of the weighted atomic coordinates. Each vibration can be visualized by looking at animations of the normal modes generated on the basis of such eigenvectors, by means of MOLDRAW software (http://www.moldraw.unito.it). The vibrational modes in silicates are usually classified either as internal (*e.g.*, stretching or bending modes of the constitutive atoms) or external (*e.g.*, modes involving the motion of extra-framework cations, or rotations and translations of the tetrahedra, behaving like rigid units). The building unit decomposition of the vibrational modes (keyword BUNITSDECO[27]) has been used to describe each vibrational mode in terms of internal and external motions of different units defined by input (*i.e.*, the Al-tetrahedron, the three Si-tetrahedra and the Na-cage). The atomic contribution of each atom type to the internal modes is supplied too.

Finally, to help in the determination of the nature of the vibrational modes, the isotopic shifts induced by changes in the cation masses have been calculated (ISOTOPES keyword[27]). The isotopic shift is a general tool useful to understand the contribution of the various ions in each normal mode, just changing by some amount (about 20% in our case) the masses of different nuclei in the structure. This tool can be generated at essentially no additional computational cost in the simulation, because, when the isotopic mass of one atom symmetry related to others is modified, the symmetry of the electronic wave function is not modified, as the mass of the atoms is not present in the single particle electronic Hamiltonian. Such procedure was followed for Na, Al and Si.

3.4 Results

The structure of low albite is generally described in a nonstandard space group $C\bar{1}$ in order to preserve the axial orientations among the feldspar group of minerals, although a primitive cell $P\bar{1}$ could be used. The number of atoms in the primitive cell is 26 (13 atoms for formula unit, Z = 2). The Al, Si and Na cations, along with the O anions, sit on the 2i Wyckoff positions.

According to the factor group analysis, the vibrational modes at the Brillouin zone-centre **k**=0 (Γ point) can be classified as:

$$\Gamma_{vib} = 39A_g + 39A_u .$$

39 Raman-active modes, 36 IR-active modes and 3 acoustic modes at zero frequency are therefore expected.

3.4.1 The 39 Raman-active modes

3.4.1.1 Backscattering on powder

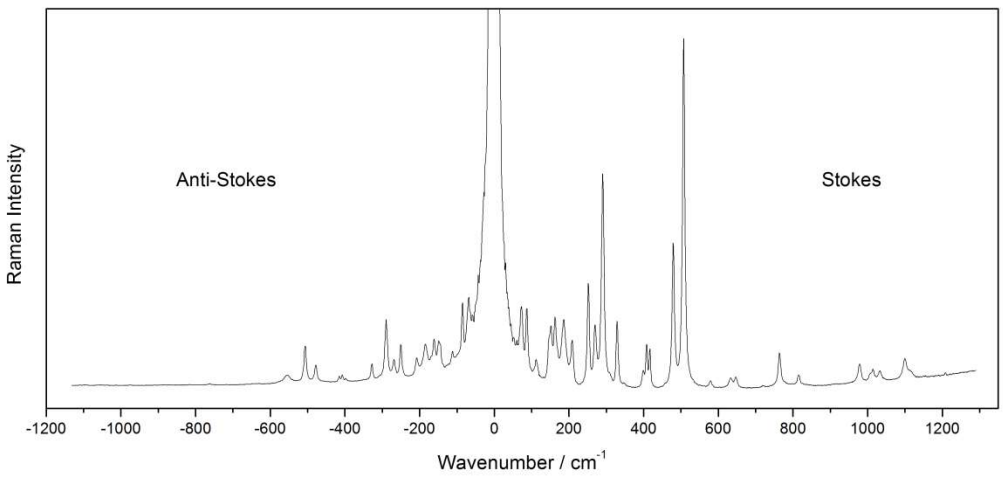

Figure 3.3: Unpolarized anti-Stokes and Stokes Raman spectra collected on loose crystals of low albite (Minas Gerais).

Figure 3.3 shows the unpolarized Stokes and anti-Stokes Raman spectra collected on loose crystal of low albite. The experimental wavenumbers, found by peak fitting procedure of the unpolarized Raman Stokes spectrum, along with the 39 computed Raman frequencies and their relative intensities, are reported in Table 3.3, where they are compared with those obtained in previous experimental works[2,38]. The observed wavenumbers in our spectra are in very good agreement with the 39 A_g modes predicted by CRYSTAL14: the mean absolute difference $\overline{|\Delta\upsilon|}$ over the 39 modes is 3.4 cm^{-1}. The largest differences ($|\Delta\upsilon_{max}|$ = 10.1 and 10.3 cm^{-1}) are due to the modes #21 (466 cm^{-1}) and #31 (825 cm^{-1}), respectively.

Table 3.3: Comparison between calculated and experimental Raman shifts with respect to experimental data from literature[2,38]. Raman spectra have been measured on a low albite from Minas Gerais[25], a low albite from Amelia Corthouse[38], a low albite (first column)[2] and a high albite (second column)[2]. Wavenumbers are in cm^{-1}. Calculated Raman intensities *I* are normalized to the most intense peak at 513 cm^{-1} and refer to the experimental conditions T = 300 K, P = 1 atm and λ = 632.8 nm on powder (polycrystalline isotropic intensities). Measured Raman wavenumbers are obtained by peak fitting procedure through LABSPEC 5.78.24. Differences Δυ are with respect to our calculated data. N_{exp} is the total number of observed Raman modes; $\overline{|\Delta\upsilon|}$ and $|\Delta\upsilon_{max}|$ are the mean absolute difference and the absolute maximum difference evaluated over the set of N_{exp} peaks, respectively. Table published in Aliatis *et al.*[25].

			Experimental							
	This work				McKeown (2005)		Freeman *et al.* (2008)			
Mode	ν_{calc}	I_{calc}	ν_{obs}	Δν	ν_{obs}	Δν	ν_{obs}	Δν	ν_{obs}	Δν
1	66	0.11	63	3.4	67	-0.6				
2	73	0.23	72	1.1						
3	92	0.13	86	5.6	89	2.6				
4	118	0.20	112	5.6	111	6.7				
5	148	0.13	144	3.9	140	7.9	140	7.9		
6	151	0.15	149	1.6	150	0.6				
7	161	0.35	162	-1.3	160	0.7			156	4.7
8	168	0.13	169	-0.7	168	0.4				
9	176	0.04	179	-3.1						
10	187	0.57	185	2.0	183	4.1	186	1.1	182	5.1
11	207	0.37	208	-1.0	207	0.0	209	-2.0	206	1.0
					216					
12	254	0.08	251	3.6	250	4.5	252	2.5	254	0.5
13	271	0.25	269	1.8	268	2.9	269	1.9	266	4.9
14	290	0.57	290	0.0	289	0.8	291	-1.2	287	2.8

15	310	0.06	308	2.3	307	3.3				
16	329	0.10	328	1.4	327	2.3	329	0.3	327	2.3
17	350	0.05	353	-3.4	346	3.6	349	0.6	346	3.6
					346					
					367					
18	398	0.05	398	-0.5	396	2.0	400	-2.0	399	-1.0
19	410	0.07	407	2.5	406	3.5	408	1.5	406	3.5
20	419	0.09	416	2.9	414*		416	2.5		
21	466	0.07	456	10.1	455	11.1	457	9.1	452	14.1
22	485	0.82	478	6.5	477	7.8	479	5.8	476	8.8
23	492	0.02	494	-1.6						
24	513	1.00	507	6.8	505	8.5	507	6.5	507	6.5
					528					
25	579	0.03	578	0.3	578	0.8	580	-1.2	578	0.8
26	634	0.01	632	1.6	632	1.9	634	-0.1	636	-2.1
27	649	0.04	646	2.8	645	4.1	646	3.1	651	-1.9
28	724	0.01	720	4.3	720	4.5	721	3.5	737	-12.5
					720					
29	768	0.22	763	5.3	762	6.5	764	4.5	762	6.5
30	784	0.02	776	8.1	770*					
31	825	0.14	815	10.3	814	11.0	815	10.0	812	13.0
32	972	0.05	978	-6.2	977	-5.4	978	-6.4	977	-5.4
33	1001	0.02	1006	-5.0	1005	-3.8	1008	-6.8		
34	1012	0.04	1014	-1.8	1010*		1013	-0.7		
35	1037	0.04	1032	4.6	1030	6.8	1033	3.8	1030	6.8
36	1044	0.01	1046	-1.5	1046	-1.5	1046	-1.5		
37	1102	0.20	1100	1.7	1098	3.7	1099	2.7	1098	3.7
38	1117	0.10	1115	2.1	1116	1.0	1113	4.0	1106	11.0
39	1156	0.01	1152	4.2	1151	5.0	1152	4.0	1139	17.0
					1170					
		N_{exp}	39		39		28		24	
		$\overline{\lvert\Delta\upsilon\rvert}$	3.4		4.1		3.5		5.8	
		$\lvert\Delta\upsilon_{max}\rvert$	10.3		11.1		10.0		17.0	

From Figure 3.4 one can notice the agreement, for both positions and intensities, between *ab initio* calculations and experimental results: the simulated spectrum for a polycrystalline isotropic sample, calculated at excitation wavelength of 632.8 nm and temperature of 300 K, assuming an overall Lorentzian broadening of 8 cm^{-1}, is compared with an experimental spectrum obtained by averaging the spectra taken on randomly oriented powdered crystals of low albite. A more detailed comparison between our measured and computed Raman wavenumbers is reported in paragraph 3.4.1.3.

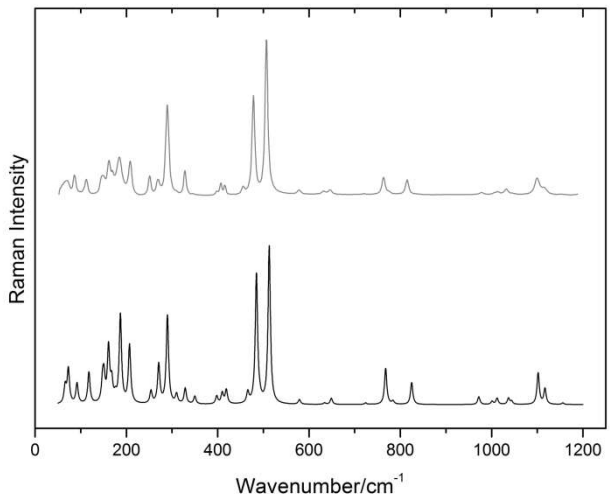

Figure 3.4: Averaged Raman spectrum of albite (*in grey*) compared with the simulated spectrum (*in black*) for polycrystalline isotropic powder, calculated at 632.8 nm wavelength laser light at 300 K. Figure published in Aliatis *et al.*[25].

3.4.1.2 Backscattering on an oriented crystal

In order to describe the directionality of Raman scattering in space, the Raman activity and the selection rules of the vibrational modes are described through the Raman tensor, a second-rank symmetric tensor, relating the polarization relationships (and therefore the selection rules) between the incident light with the scattered light. The Raman tensor is referred to orthogonal crystalline axes $X_{crys}Y_{crys}Z_{crys}$ defined for each crystallographic system. In triclinic structures, the choice of the axes is not standardized. In our measurements the *b* crystallographic axis is nearly taken as Y_{crys}. X_{crys} and Z_{crys}, mutually perpendicular, lie in the plane nearly perpendicular to *b*, but at some angle

to the crystallographic axes *a* and *c*. For albite crystals, the angles between the $X_{crys}Y_{crys}Z_{crys}$ system and the *a*, *b*, *c* axes are given by the matrix:

$$\begin{matrix} 2.31450 & 89.95841 & 116.47062 \\ 87.68734 & 0.04229 & 94.25207 \\ 89.90773 & 90.00767 & 26.86330 \end{matrix}$$

The X_{crys} axis forms an angle of about 2° with the *a* crystallographic axis, and Z_{crys} is nearly perpendicular to the *ab* plane at ~27° from the *c* axis (see Figure 3.5).

If we refer to the crystallographic orthogonal system, we obtain the following second-rank Raman tensor, corresponding to the A_g **k**=0 modes under the C_i point group:

$$\begin{matrix} a & d & e \\ d & b & f \\ e & f & c \end{matrix}$$

As a general rule[39], the intensity *I* of a given Raman mode is obtained by:

$$I \propto |\mathbf{e_i} \cdot \boldsymbol{R} \cdot \mathbf{e_s}|^2$$

where $\mathbf{e_i}$ and $\mathbf{e_s}$ are the unit polarization vectors of the electric field of the incident and scattered laser beams, respectively, and $\boldsymbol{R}$ is the Raman scattering tensor of the particular mode. The proportionality sign arises from the dependence of the Raman intensity on instrumental configuration and on thermal and frequency factors (see paragraph 3.3).

When the laboratory $X_{Lab}Y_{Lab}Z_{Lab}$ frame coincides with the crystallographic orthogonal system $X_{crys}Y_{crys}Z_{crys}$, we can use the Raman tensor as it is. If the laboratory frame does not coincide with the crystallographic orthogonal reference system, one must "rotate" the Raman tensor according to the rule:

$$\boldsymbol{R^*} = \boldsymbol{T}\,\boldsymbol{R}\,\boldsymbol{T^{-1}}$$

where $\boldsymbol{T}$ is the appropriate orthogonal rotation matrix.

The definite crystal faces of the sample are (010), (001) and an approximate face ~(100). Raman backscattering has been performed on all the three faces.

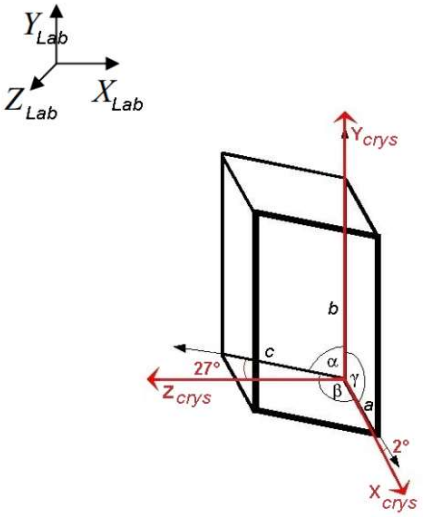

Figure 3.5: Cartesian $X_{crys}Y_{crys}Z_{crys}$ axes with respect to the triclinic crystallographic cell (*a b c* crystallographic axes). $X_{Lab}Y_{Lab}Z_{Lab}$ axes show the laboratory frame. Figure published in Aliatis *et al.*[25].

3.4.1.2.1 Backscattering along the (010) face

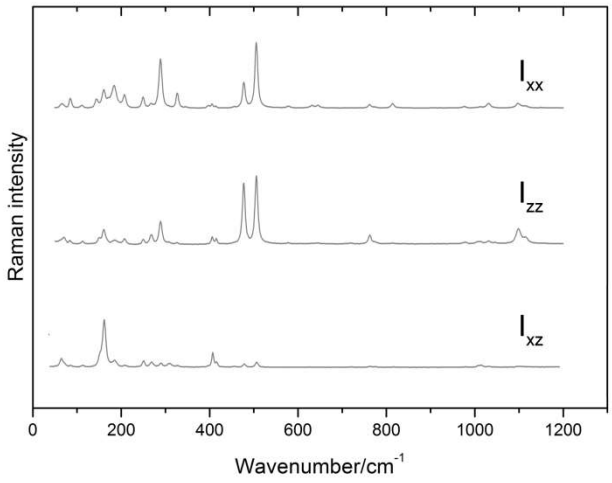

Figure 3.6: Experimental I_{XX}, I_{ZZ} and I_{XZ} spectra measured on the (010) face of the albite crystal.

The XX, ZZ and XZ elements of the Raman tensor are expected to determine the spectra taken on the (010) crystallographic face (Figure 3.6), at least as a first approximation. To have further insight into the Raman intensities and to compare experimental results with Crystal14 predictions, we have performed Raman measurements by rotating the sample around the *b* ($\sim Y_{crys}=Y_{Lab}$) direction. The crystallographic orthogonal axes X_{crys} and Z_{crys} are identified in the plane nearly perpendicular to *b* (X_{crys} is nearly in the *a* direction, which is clearly visible on this face because the major striae are along the *a* axis direction). The sample was then rotated from $\vartheta = 0°$ to $\vartheta = 180°$ (step 15°), ϑ being the angle between the polarization direction of the excitation light (along X_{Lab}) and the crystallographic *a* axis. For each value of the angle ϑ, the Raman spectra were taken with parallel polarizers (PP=XX) and crossed polarizers (PV=XZ). To roughly describe the angular variation of the spectra taken on the (010) face, we could imagine the scattering geometry as for a monoclinic crystals, *i.e.*, assuming $\alpha = \gamma = 90°$.

According to the rule $I \sim |e_i\ R\ e_s|^2$, where *R* is the Raman tensor defined in the $X_{crys}Y_{crys}Z_{crys}$ system, and e_i and e_s are the unit polarization vectors of the incident and scattered laser beams, respectively, whose components depend on the angle ϑ or, equivalently, by rotating the Raman tensor according to the rule $R^* = T\ R\ T^{-1}$, where *T* is the rotation matrix:

$$\begin{matrix} \cos\vartheta & 0 & \sin\vartheta \\ 0 & 1 & 0 \\ -\sin\vartheta & 0 & \cos\vartheta \end{matrix}$$

we expect, in the "monoclinic approximation" the following dependence of the Raman intensity of the A_g mode on the rotation angle ϑ:

$$I_{PP} \sim |a * cos^2\vartheta\ +\ c * sin^2\vartheta +\ e * sin2\vartheta|^2$$

$$I_{PV} \sim |(c-a)/2 * sin2\vartheta + e * cos2\vartheta|^2$$

a, *c* and *e* being the elements of the Raman tensor for the A_g symmetry modes in the orthogonal crystallographic system $X_{crys}Y_{crys}Z_{crys}$.

The PP and PV spectra as a function of the rotation angle ϑ are reported in Figure 3.7.

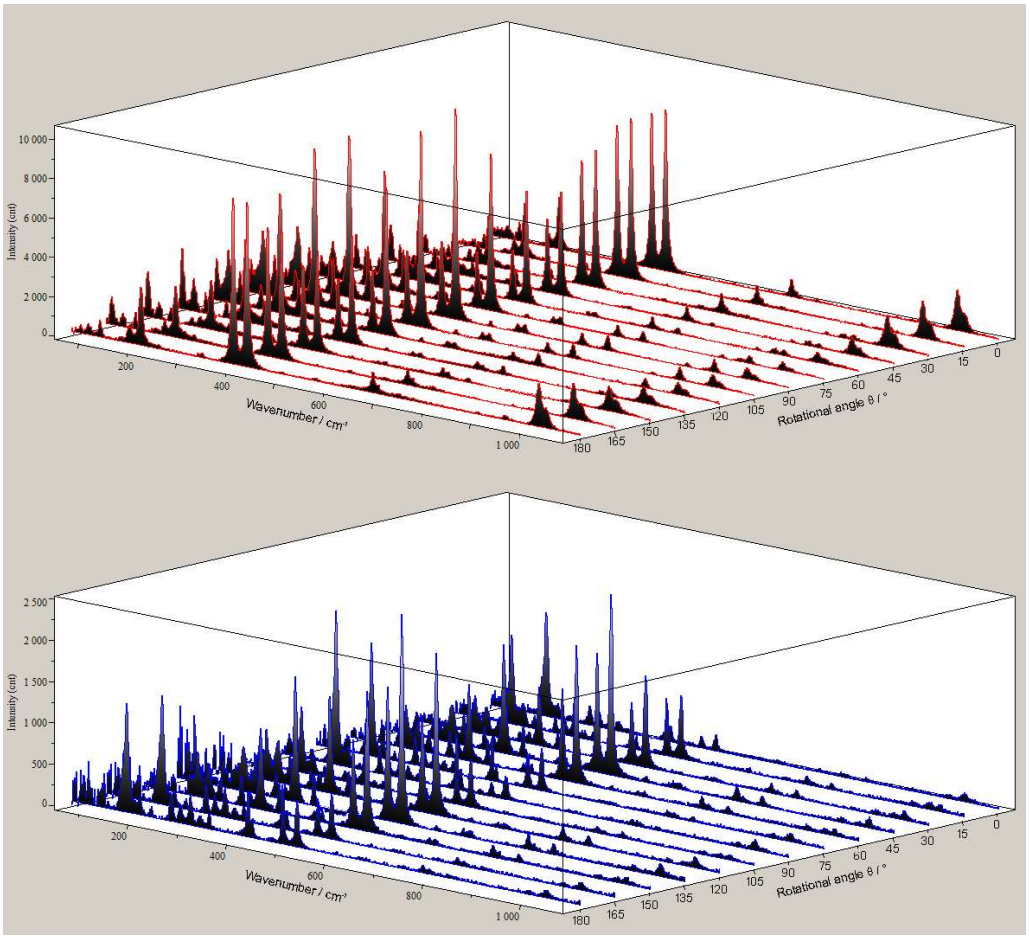

Figure 3.7: PP and PV spectra collected on the (010) face of albite crystal as a function of the rotation angle ϑ (0-180°).

3.4.1.2.2 Backscattering on the other faces of the crystal

Approximate YY and XY polarization geometries on the (001) face of the crystal and YZ on the ~(100) face give some indications on the corresponding elements of the Raman tensors (see Figure 3.8). In these scattering geometries obviously one observes leakages from the strongest modes.

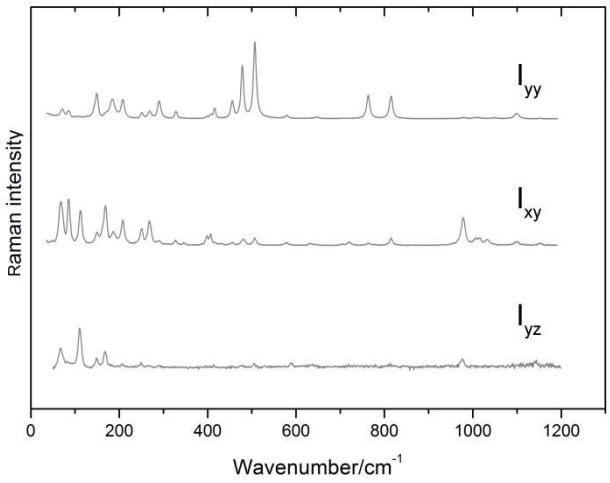

Figure 3.8: Experimental I_{YY}, I_{XY} and I_{YZ} spectra measured on the (001) and ~(100) faces of the albite crystal.

3.4.1.3 Comparison with CRYSTAL14 ab initio calculations

A closer comparison between computed and experimental Raman spectra allows a reliable characterization of doubtful modes (see Table 3.3). The calculation of the Raman intensities is essential for a correct and unambiguous assignment of the eigenmodes to the corresponding measured features, especially in complex silicates, such as open-framework silicates, where overlapping modes within narrow spectral ranges are very frequent. We notice that the experimental broad band centred at ~68 cm^{-1} is the convolution of the calculated modes #1 and #2, whose experimental maxima may be deconvoluted at 63 and 72 cm^{-1} by the fitting procedure. Moreover, the six Raman bands in the range from 130 to 190 cm^{-1}, corresponding to the modes from #5 to #10, have been resolved in the measured spectrum as three maxima centred at 149, 162 and 185 cm^{-1} and three shoulders at 144, 169 and 179 cm^{-1}. The mode #21, calculated at 466 cm^{-1} and measured at 456 cm^{-1}, is observed (with medium intensity) only in the spectra collected on the (001) crystallographic face, whereas it is very weak on the (010) face. Finally, the broad bands around 1010 and 1040 cm^{-1} are due to the overlap of the modes #33-#34 and #35-#36, respectively, which have been found by fitting at 1006, 1014, 1032 and 1046 cm^{-1}. The strong Raman band at 1099 cm^{-1} and its shoulder at 1115 cm^{-1} correspond to the modes #37 and #38.

On the contrary, the very weak mode #23, computed at 492 cm^{-1}, cannot be exactly resolved between the two strong bands observed at 478 and 507 cm^{-1} in the experimental spectra.

A more significant comparison may be made referring to the single non-vanishing XX, YY, ZZ, XY, YZ and XZ components of the Raman tensor. The calculated single crystal directional intensities, as reported by CRYSTAL14 output, are listed in Table 3.4. From the theoretical intensities, we simulated the spectra corresponding to the six RTE, assuming a Lorentzian broadening of 8 cm^{-1} for each computed wavenumber. In Figure 3.9, the six independent single crystal directional spectra obtained from our calculations are compared with the experimental ones. The six measured spectral profiles agree very well with the simulated ones. Some leakage is obviously present: for example, in the XY spectrum, the strongest A_g modes at 478 and 507 cm^{-1} are still observed even though, according to the intensities calculated by CRYSTAL14, they should have negligible intensities.

Table 3.4: Single crystal directional intensities, as reported by CRYSTAL14 output. Intensities are in arbitrary units.

Modes (cm^{-1})	I_{xx}	I_{xy}	I_{xz}	I_{yy}	I_{yz}	I_{zz}
66	60	12	74	32	0	112
73	15	36	10	121	108	217
92	42	49	75	138	7	19
118	25	37	79	2	205	32
148	366	2	0	57	1	0
151	28	11	5	385	23	1
161	335	4	223	12	27	379
168	3	55	23	13	77	106
176	5	8	16	12	19	26
187	1000	7	1	448	6	26
207	419	58	1	307	0	121
254	2	21	82	5	19	33
271	34	42	45	131	5	346
290	924	0	30	109	2	379
310	100	4	18	16	1	21
329	67	30	59	4	40	2

350	72	0	3	25	4	11
398	9	9	36	24	5	12
410	79	9	39	4	0	57
419	20	0	36	82	3	97
466	9	5	6	179	8	12
485	536	0	44	517	2	917
492	0	6	0	48	2	2
513	956	0	3	562	11	956
579	26	8	0	34	0	7
634	20	2	3	0	2	4
649	41	1	5	16	2	21
724	0	8	0	1	3	23
768	105	1	2	284	1	173
784	13	1	5	2	0	18
825	100	6	7	247	1	15
972	3	37	1	7	27	24
1001	1	9	0	27	5	20
1012	4	9	15	15	7	62
1037	41	4	26	1	2	40
1044	7	10	1	13	2	0
1102	140	19	19	86	4	218
1117	94	0	28	1	7	137
1156	7	1	3	13	0	10

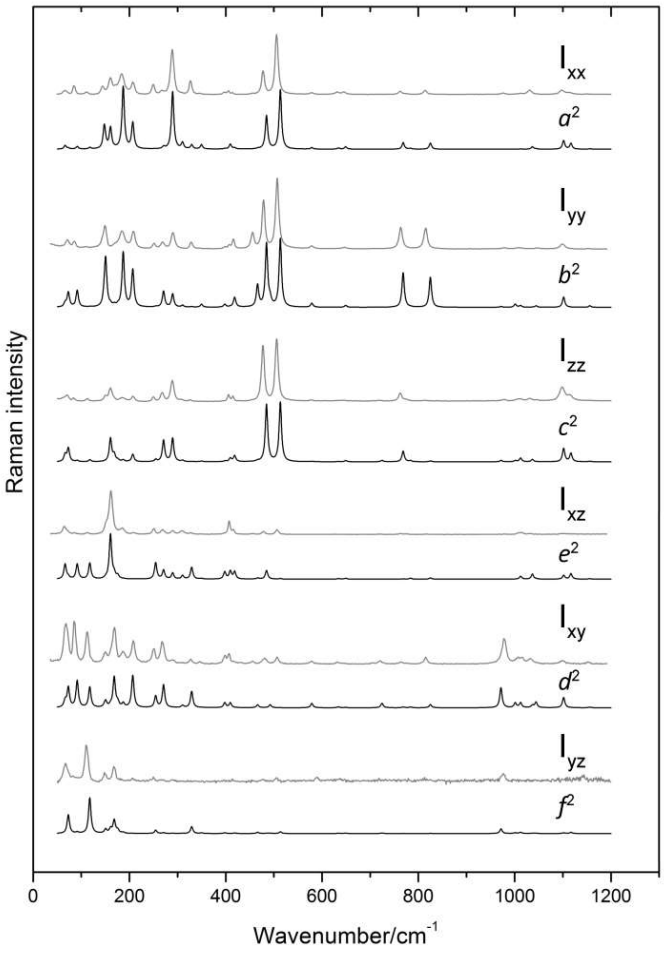

Figure 3.9: Experimental directional spectra measured on the (010), (001) and ~(100) faces of the albite crystal (*in gray*) along with the corresponding calculated Raman spectra (*in black*). Each measured spectrum is scaled so that the intensity of the strongest peak agrees with the theoretical intensity of the corresponding calculated mode. Figure published in Aliatis *et al.*[25].

Figure 3.10 shows the comparison between experimental and calculated angular dependencies, in parallel and cross-polar polarizations, of the Raman scattering intensities for spectral lines at 507, 478 and 290 cm^{-1} corresponding to A_g vibration modes at 513, 485 and 290 cm^{-1} by HF/DFT simulation. The experimental intensities have been determined by the peak areas by spectral fitting, according to Lorentzian peak functions after subtraction of a suitable baseline. All the three modes, as expected, show PP and PV curves with a periodicity of 180° and 90°, respectively. The experimental behaviour may be reproduced fairly well with theoretical curves (see

equations in paragraph 3.4.1.2.1), if one assumes for the RTE *c* a negative value $-(I_{zz})^{½}$, whereas *a* = $(Ixx)^{1/2}$ and *e* = $(I_{XZ})^{1/2}$.

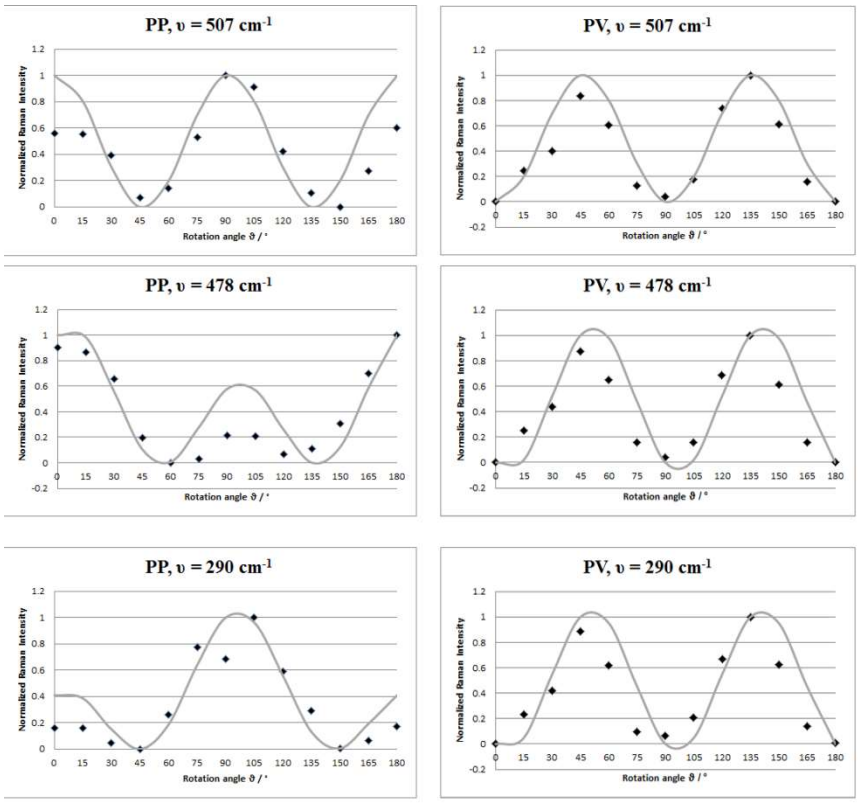

Figure 3.10: Experimental and theoretical plots of the angular dependencies in parallel (PP) and cross-polar (PV) polarization for the 507, 478 and 290 cm^{-1} observed A_g Raman modes, corresponding to predicted modes at 513, 485 and 290 cm^{-1} by HF/DFT simulation. Solid curves are the calculation; dots are the experimental results.

3.4.1.4 Analysis of the normal modes

First of all, all the 39 normal modes have been approximately classified in five groups, as suggested by Freeman *et al.*[2]:

- Group I (in the range of 450 and 520 cm^{-1}) is characterized by the two strongest peaks due to the breathing modes of the four membered tetrahedral rings;
- Group II (200-400 cm^{-1}) includes bands due to rotation–translation modes of the rings;
- Group III (below 200 cm^{-1}) is characterized by cage–shear modes;
- Group IV (600-900 cm^{-1}) describes the deformation modes of the tetrahedra;
- Group V (900-1200 cm^{-1}) includes the vibrational stretching modes of the tetrahedra.

From the analysis of the eigenvectors and by looking at the animations of the corresponding normal modes (Figure 3.11), the attributions made in previous works[2,38] have been revised. In Table 3.5, we report a short description of the main contributions to the atomic displacements for each A_g Raman-active mode.

Table 3.5: Brief description of the 39 A_g Raman-active modes.

Modes (cm^{-1})	Description of the vibrational eigenvectors
66	translation of the Na^+ cations along the *a* direction, rigid rotations of SiO_4;
73	translation of the Na^+ cation parallel to the *a* axis;
92	translation of the Na^+ cations along the *a* direction, rigid rotations of TO_4;
118, 148	rotations of the four tetrahedra, translation of Na^+ cations;
151,161, 168	Na^+ translations, rigid translations of TO_4 (tetrahedral cages deformations);
176, 187	Na^+ cations translations in the cages: parallel and perpendicular to the *b* axis;

207	rigid translation of the tetrahedra, Na^{+} motion along the *b* direction;
254	rigid rotations of SiO_4, deformation of AlO_4;
271, 290	rotations of the tetrahedra;
310, 329, 350, 398, 410 , 419	deformations of the tetrahedra (mainly bending modes of the Al-O-Si and Si-O-Si bonds);
466	deformation of the tetrahedra; Si atoms contribute to the motion, in particular in the $T_2(0)$ tetrahedra;
485, 490	deformation of the tetrahedra, mainly O-Si-O and Si-O-Si (or Al) bending. The first one is a clear cage breathing mode;
513	bending deformation of the Al-O-Si and Si-O-Si bonds, with the central cations of the tetrahedra almost stationary;
579	deformation of the tetrahedra, with a strong contribution of $T_1(m)$;
634, 649, 724	bending-deformation of the tetrahedra;
768	bending deformation of $T_2(m)$ tetrahedra;
784, 825	deformation of the four tetrahedra. The $T_i(o)$ tetrahedra give a major contribution to the motion at 784 cm^{-1};
972, 1001, 1012	stretching of the T_2 tetrahedra;
1037	stretching of $T_2(m)$ tetrahedra;
1044	anti-symmetric stretching of the $T_1(m)$ and $T_2(m)$ tetrahedra;
1102	anti-symmetric stretching for all the SiO_4 tetrahedra;
1117	anti-symmetric stretching of the $T_1(m)$ and $T_2(o)$;
1156	symmetric stretching of the $T_i(m)$ tetrahedra.

Figure 3.11: Vibrational patterns of the modes corresponding to the seven more prominent peaks in the Raman spectrum of albite, shown in the *ab* and *ac* planes. Calculated wavenumbers are indicated. Atomic displacements are shown by black arrows. Atom types are: Na (yellow), Si (red), Al (green) and O (blue).

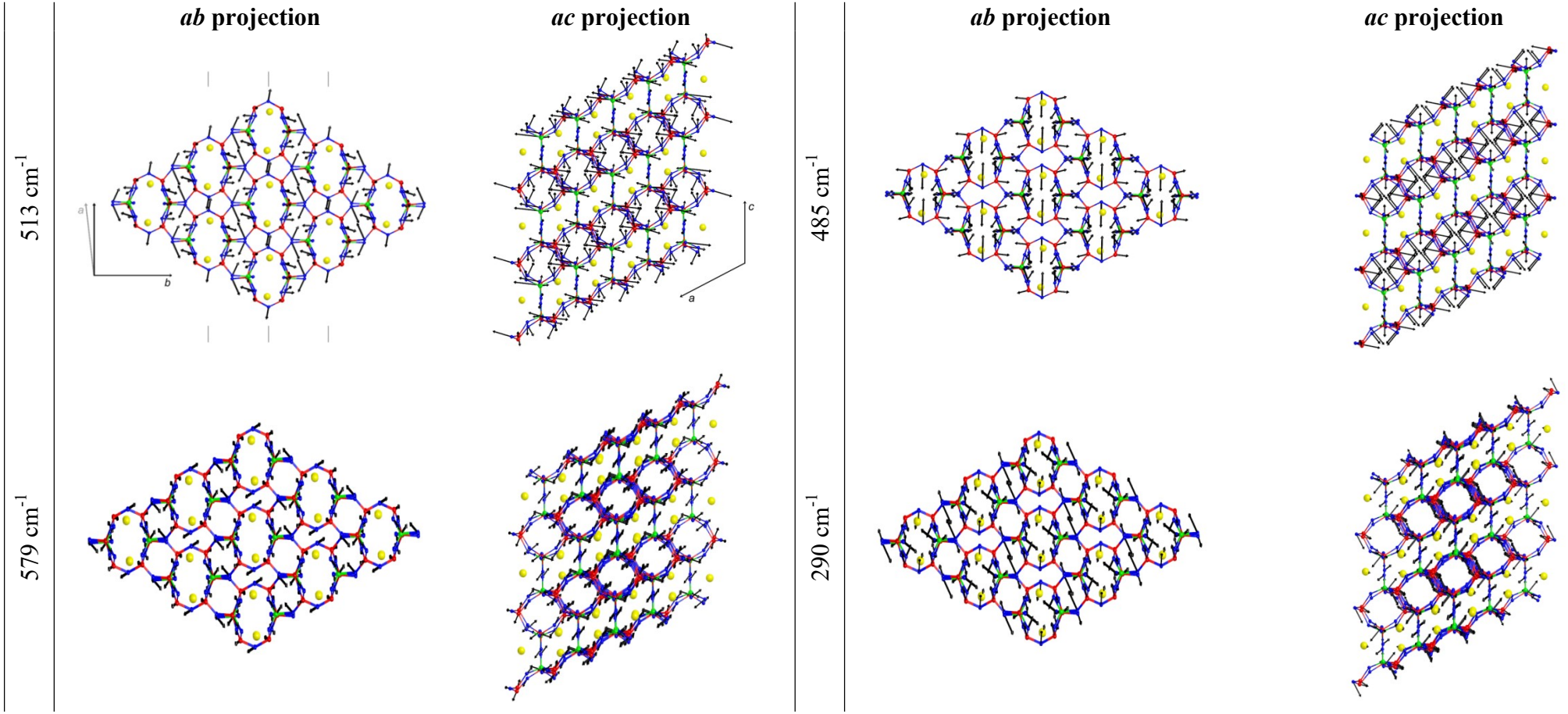

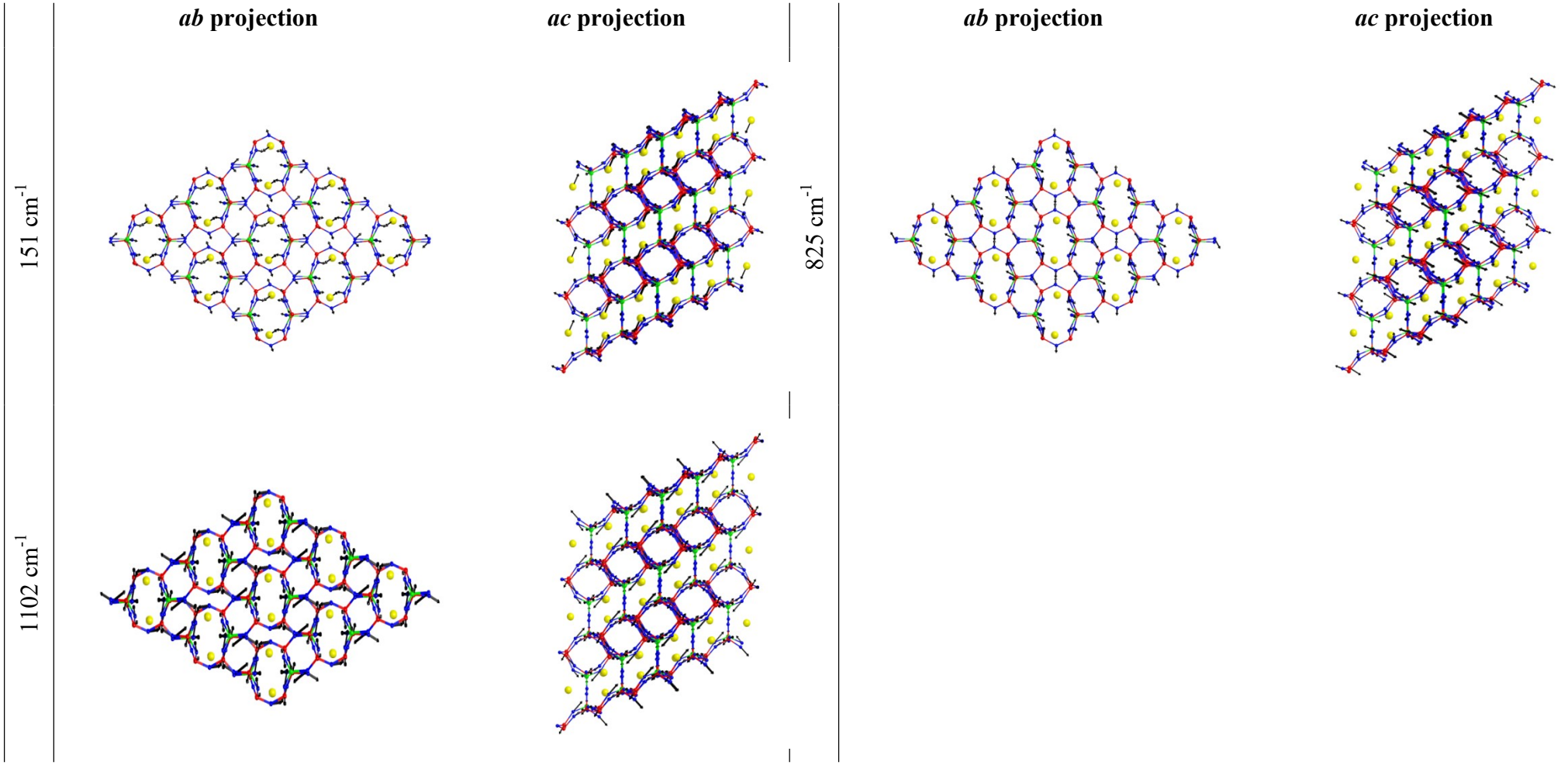
ab projection
ac projection
ab projection
ac projection
151 cm-1
1102 cm-1
825 cm-1

The calculated isotope-dependent frequency shifts allow estimating the contribution of the different cations (*i.e.*, Na, Al and Si) to the vibrational pattern motion for each Raman mode (see Figure 3.12). We have observed that the Na^+ cations contribute only to the modes below 210 cm^{-1}, whereas Al predominates mainly in the spectral range of the group IV and Si is most involved above 400 cm^{-1}. The specific contribution of the cations differs with respect to previous assignments: *e.g.*, the Na atoms are involved only in low-wavenumber modes, and not contribute significantly to further modes as reported in the LD simulation[38].

The isotope calculation on the Si atoms suggests that the three non-equivalent tetrahedra T_1(m), T_2(o) and T_2(m) are randomly involved in the majority of the Raman peaks (Figure 3.13).

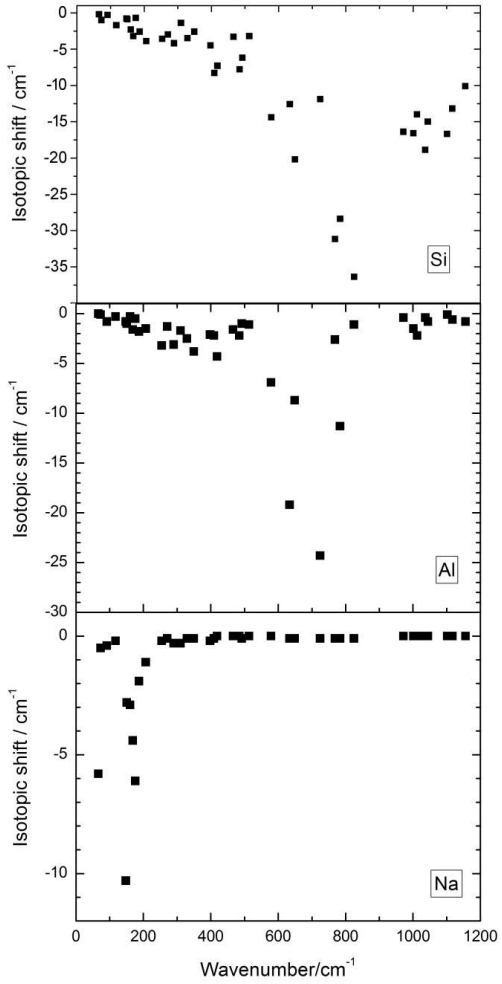

Figure 3.12: Calculated isotopic shift of the Raman mode frequencies of albite when Si, Al or Na masses are increased by ~20%. Figure published in Aliatis *et al.*[25].

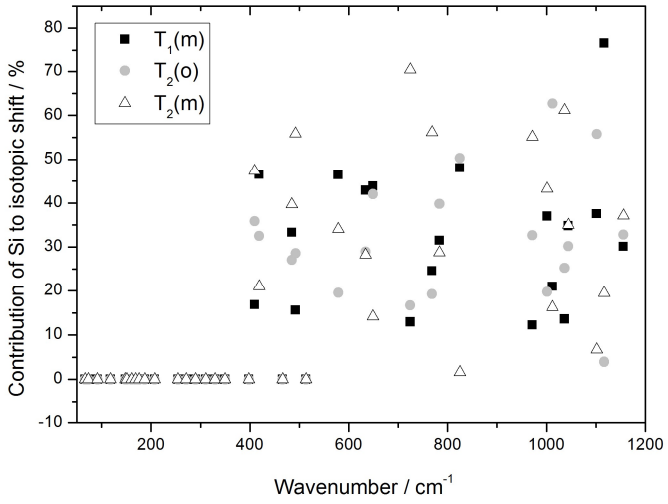

Figure 3.13: Percentage contribution of Si to the isotopic shift by the three occupied atomic positions. Figure published in Aliatis *et al.*[25].

3.4.2 The 36 infrared-active modes and the comparison with CRYSTAL14

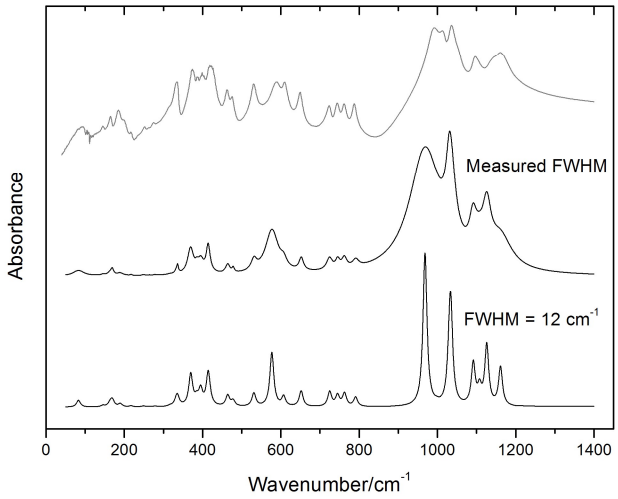

Figure 3.14: Experimental infrared absorption spectrum of albite (*in grey*) compared with the simulated spectra (*in black*), obtained setting a bandwidth of 12 cm^{-1} or experimental bandwidths for each peak.

The infrared absorption spectrum of low albite in a CsI pellet has been recorded for comparison with calculated infrared data (see Figure 3.14). The IR spectrum simulated with pure Lorentzian band shapes with constant linewidth of 12 cm^{-1} is shown along with a more faithful spectrum, obtained giving the corresponding measured FWHMs to each calculated peak.

The experimental and calculated frequencies are listed in Table 3.6. The correspondence between calculated and experimental modes was determined on the basis of both frequencies and intensities. The absolute maximum and the average absolute differences between an experimental band and the calculated band are 24.9 cm^{-1} and 5.1 cm^{-1}, respectively. More than half of the predicted bands are within 6 cm^{-1} of the experimental values. The observed experimental bands agree very well with those reported in literature[38,40].

An attempt to better discriminate among the measured bands in the 900-1200 cm^{-1} spectral range has been performed at 9 K (see Figure 3.15), but without any significant improvement of the spectral resolution.

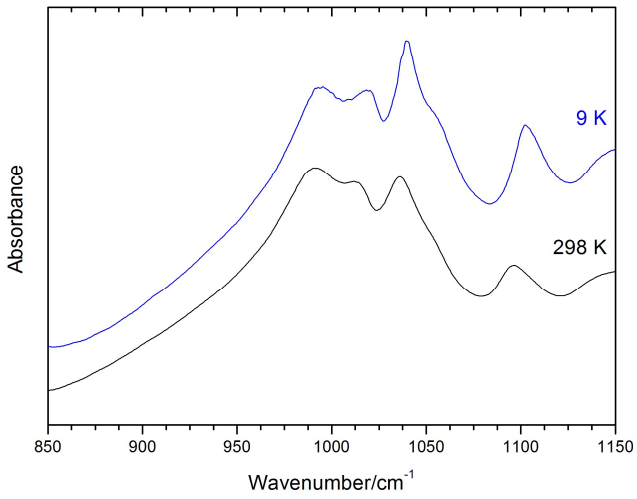

Figure 3.15: Experimental infrared spectra recorded at 298 K and at 9 K in the 850-1150 cm^{-1} spectral range.

Table 3.6: Comparison between calculated and experimental infrared band wavenumbers in cm^{-1} with respect to experimental data from literature[38,40]. Calculated integrated infrared intensities *I* are normalized to the most intense peak at 968 cm^{-1} and are computed under the hypothesis of isotropic response (*i.e.*, powdered sample). Measured infrared wavenumbers are obtained by peak fitting procedure through LABSPEC software. Differences Δυ are with respect to our calculated data. N_{exp} is the total number of infrared wavenumbers; $\overline{|\Delta\upsilon|}$ and $|\boldsymbol{\Delta\upsilon_{max}}|$ are the average absolute difference and the absolute maximum difference evaluated over the set of N_{exp} peaks, respectively.

			Experimental					
	This work				Von Stengel (1977)		Zhang *et al*. (1996)	
Mode	ν_{calc}	I_{calc}	ν_{obs}	Δν	ν_{obs}	Δν	ν_{obs}	Δν
1	80	0.003	72	8.0				
2	83	0.042	90	-7.0	92	-9.0	90	-7.0
3	145	0.009	146	-1.1	146	-1.1	145	-0.1
4	164	0.026	164	-0.2	165	-1.2	164	-0.2
5	169	0.042	184	-14.7	186	-16.7	185	-15.7
6	189	0.020	200	-10.6	200	-10.6	201	-11.6
7	217	0.007	217	0.1	217	-0.1	216	0.9
8	249	0.006	250	-1.4	252	-3.1	251	-2.1
9	264	0.003	261	3.0				
10	278	0.004	274	4.3	276	2.3	276	2.3
11	317	0.006	316	1.3			318	-1.2
12	333	0.031	330	2.8				
13	336	0.053	335	0.2	336	-0.3	334	1.7
14	369	0.208	373	-3.4	375	-5.6	374	-4.6
15	385	0.042	387	-2.2	387	-2.4	387	-2.4
16	395	0.100	399	-4.1	400	-5.2	400	-5.2
17	414	0.216	415	-1.1			429	-14.9
18	419	0.010	425	-6.1	426	-7.3	416	2.7
19	464	0.071	462	1.7	462	1.9	462	1.9
20	478	0.036	475	2.5	474	3.8	476	1.8
21	531	0.087	531	-0.1	530	0.8	531	-0.2
22	577	0.352	587	-9.8	589	-12.3	589	-12.3
23	607	0.062	611	-4.2	607	-0.2	611	-4.2
24	652	0.102	649	2.8	648	3.6	650	1.6
25	724	0.096	722	2.6	722	2.5	732	-7.5
26	745	0.071	744	0.9	742	2.6	744	0.6
27	762	0.085	762	0.8	760	2.4	761	1.4
28	791	0.060	788	2.8	786	4.8	781	9.8
29	968	1.000	993	-24.9	988	-19.9	994	-25.9

30	998	0.009	1014	-15.6	1004	-5.9	1018	-19.9
31	1030	0.194	1037	-7.1	1032	-2.1	1040	-10.1
32	1034	0.598	1051	-17.1	1048	-14.1	1058	-24.1
33	1091	0.271	1096	-4.3	1096	-4.5	1102	-10.5
34	1107	0.104	1109	-1.7	1106	1.5		
35	1126	0.391	1137	-10.8	1142	-16.2	1142	-16.2
36	1161	0.251	1162	-1.0	1160	1.0	1162	-1.0
		N_{exp}	39		39		28	
		$\overline{\lvert\Delta\upsilon\rvert}$	5.1		5.3		6.3	
		$\lvert\Delta\upsilon_{max}\rvert$	24.9		19.9		25.9	

3.5 Discussion

3.5.1 Previous calculations of the low albite Raman frequencies

In the last 40 years, several research groups reported on the Raman spectra of feldspars[2,4,38,41–48]. The first normal mode calculations on albite, based on valence potential force constant model, were presented by Von Stengel[49], but no vibrational assignment was attempted. The first detailed description of each vibrational mode appeared in 2005, when McKeown[38] classified the full set of 39 A_g modes by lattice dynamics (LD) calculations and compared his results with those presented by Von Stengel[49]. In particular, he reported the unpolarized Raman spectrum of a triclinic crystal of ordered albite at room temperature and studied the evolution of the Raman features from 25 °C to temperature above the melting at 1118 °C, through the triclinic-to-monoclinic displacive phase transition at 980 °C. He used a sixty-three atom cluster to simulate the albite triclinic structure for the LD calculation at zero wavevector. The potential energy model used to describe the bonding within the structure model is based on a valence force potential consisting of Si-O, Al-O and Na-O bond stretching as well as O-Si-O, O-Al-O and O-Na-O bond bending interactions. The LD calculation used a total of 190 interactions described by seven force constants that adequately describe the bonding environment in the structure. The seven force constants were varied to provide the best fit between the calculated and observed frequencies in the Raman spectrum. The assignments by McKeown[38] were employed in 2008 by Bendel and Schmidt[4] and by Freeman *et al*.[2], who proposed to group the feldspar spectral characteristics as follows: Group I, in the 450-520 cm^{-1} spectral region, assigned to the ring-breathing modes of the four-membered rings of tetrahedra; Group-II, between 200 and 400 cm^{-1} and Group-III, below 200 cm^{-1}, corresponding to rotation-translation modes of the four-membered rings and cage-shear modes, respectively; the mid- to weak-strength Group-IV in the 700-900 cm^{-1} region describing the deformation modes of the tetrahedra; and finally Group-V in the 900-1200 cm^{-1} range, assigned to the vibrational stretching modes of the tetrahedra.

Lattice dynamics calculations are, however, not fully satisfactory because are based on classical models of atomic interactions and require *a priori* knowledge of the fundamentals modes with respect to combination and overtones in the spectrum. Nowadays, *ab initio* approaches aim to

reproduce the properties of crystals, at any T/P condition, with the least possible amount of *a priori* empirical information. In principle, no information other than the chemical composition of the material should be required; in practice, an approximated starting structure of the crystal (*i.e.*, symmetry, cell parameters and atomic fractional coordinates) is often a mandatory prior information for a successful simulation. The first *ab initio* calculations on albite were performed by Méheut and Schauble[50] in 2014. Authors determined the isotope fractionation factors for oxygen and silicon in phyllosilicates (pyrophyllite and talc), albite and pyrope, from harmonic partition functions, which require the knowledge of the phonon frequencies. They used first-principle methods based on DFT and employed the PBE functional[51].

In Table 3.7, the comparison between our calculated frequencies, obtained by an hybrid HF/DFT method using the WC1LYP Hamiltonian[25], and the previous LD[38] and DFT-PBE[50] results, with respect to their respective experimental data, is reported. Overall, all the authors computed 39 Raman modes, out of which 33 are common. Six Raman modes (at 221, 349, 362, 526, 728 and 1173 cm^{-1}), computed by LD calculations, are not expected in *ab initio* calculations. In particular, the LD computation provided two doublets, at 344 and 349 cm^{-1} and at 725 and 728 cm^{-1}, respectively, which are unresolved in the Raman spectrum and attributed to the same experimental features at 346 and 720 cm^{-1}, respectively. Five Raman modes are present only in DFT calculations, but the differences are very large (up to 46 cm^{-1}), except for the mode at 176 cm^{-1}. The first and the third columns in Table 3.7 report also measured wavenumbers at 414, 770 and 1010 cm^{-1} (labelled by asterisks), attributed by McKeown[38] to overtones, but used by Méheut and Schauble[50] as fundamental modes. The fundamental nature of the aforementioned bands is supported by our calculation, which gives normal modes at 419, 784 and 1012 cm^{-1}, respectively. The DFT-PBE computed wavenumber at 60 cm^{-1} has no correspondence in our HF/DFT-WC1LYP calculation. Further, the wavenumber at 73 cm^{-1}, expected in all the calculations, has not been assigned to the same observed band. These discrepancies are due to the fact that McKeown[38] observed only two bands at low wavenumbers (*i.e.*, 67 and 89 cm^{-1}), instead of three (*i.e.*, 63, 72 and 86 cm^{-1}). Therefore, our calculated Raman modes at 66 and 73 cm^{-1} should be compared with those of Méheut and Schauble[50] at 60 and 73 cm^{-1}, respectively.

If we look at the experimental data (see υ_{obs} in Table 3.7), we notice that our measured Raman shifts correspond well to those reported by McKeown[38], except for the features at 216, 367,

528 and 1170 cm^{-1}, which are absent in our spectra; in addition, as already mentioned, two sets of two modes each are reported at the same wavenumbers (*i.e.* 346 and 720 cm^{-1}).

Table 3.7: Comparison among three sets of calculated wavenumbers of the Raman features of low albite with respect to the experimental results. Wavenumbers are in cm^{-1}. Measurements used in DFT-PBE are from McKeown[38]. The correspondence between the three calculated datasets is obtained by a preliminary comparison of each one with the correspondig experimental data.

McKeown (2005)		Méheut *et al*. (2014)		This work	
LD		DFT-PBE		HF/DFT-WC1LYP	
υ_{obs}	υ_{calc}	υ_{obs}	υ_{calc}	υ_{obs}	υ_{calc}
		(2)	60		
67	69	67	73	63	66
				72	73
89	73	89	88	86	92
111	120	111	111	112	118
140	135	140	144	144	148
150	147	150	147	149	151
160	162	160	158	162	161
168	172	168	166	169	168
		(2)	176	179	176
183	189	183	181	185	187
207	201	207	202	208	207
216	221	216	(1)		
250	242	250	244	251	254
268	278	268	259	269	271
289	295	289	278	290	290
307	306	307	298	308	310
327	317	327	315	328	329
346	344	346	333	353	350
346	349				
367	362	367	(1)		
396	400	396	380	398	398
406	405	406	390	407	410
414*		414*	397	416	419
455	460	455	436	456	466

477	478	477	456	478	485
		(2)	460	494	492
505	506	505	481	507	513
528**	526				
578	578	578	550	578	579
632	627	632	600	632	634
645	633	645	617	646	649
720	725	720	688	720	724
720	728				
762	764	762	727	763	768
770*		770*	737	776	784
814	797	814	778	815	825
977	962	977	926	978	972
1005	994	1005	957	1006	1001
1010*		1010*	966	1014	1012
1030	1032	1030	987	1032	1037
1046	1056	1046	1001	1046	1044
1098	1099	1098	1052	1100	1102
1116	1111	1116	1067	1115	1117
1151	1159	1151	1108	1152	1156
1170	1173	1070	(1)		
$\overline{\lvert\Delta\upsilon\rvert}$	5.7		22.0		3.4
$\lvert\Delta\upsilon_{max}\rvert$	17		51.0		10.3

* The frequencies at 414, 770 and 1010 cm^{-1} are reported by McKeown[38] but attributed to overtones of stronger peaks.

** From White[52].

(1) McKeown[38] reported peaks at 216, 367 and 1070 cm^{-1} that cannot be attributed to any calculated frequencies.

(2) Calculated frequencies at 60, 176 and 460 cm^{-1} cannot be correlated to any experimental frequencies.

3.5.2 Previous calculations of the low albite infrared frequencies

Infrared spectroscopy has been employed more than Raman spectroscopy in the study of feldspars. It has been exploited to investigate the phase transitions and the Al-Si ordering in the alkali feldspars solid solutions. A simple relation has been suggested between the shift in the infrared positions, the degree order of the structure and the phase transition temperature[40,53–56]: $(\Delta\omega^2) \propto Q^2 \propto |T - T_c|^{2\beta}$, with β = ½. Furthermore, IR spectra of plagioclases were collected by Atkinson *et al.*[57] in order to investigate the local order and compare it with the macroscopic behaviour.

The first comparison between measured IR spectra and calculated IR fundamental mode frequencies is presented by Von Stengel[49] and then revised by McKeown[38], where the normal mode calculations were based on valence potential force constant models. The calculated IR modes have varying degrees of success to predict the observed mode frequencies. The description of the atomic motions involved in each vibrational mode is listed in McKeown[38]. More recent calculation was performed by Mèheut and Schauble[50] in 2014. Table 3.8 compares all the results.

Table 3.8: Comparison between three sets of calculated wavenumbers of the infrared active modes of low albite with respect to the experimental data. Wavenumbers are in cm^{-1}. Data for LD are from Von Stengel[38,49]; for DFT-PBE from Zhang *et al.*[40] and Couty *et al.*[58]. The correspondence between the three calculated datasets is obtained by a preliminary comparison of each one with the correspondig experimental data.

McKeown (2005)		Méheut *et al.* (2014)			This work	
LD		DFT-PBE			HF/DFT-WC1LYP	
υ_{obs}	υ_{calc}	υ_{obs}	υ_{calc} (TO)	υ_{calc} (LO)	υ_{obs}	υ_{calc}
			82	90	72	80
92	86	90	82	82	90	83
146	166	145	141	142	146	145
165	187	164	160	164	164	164
186	193	185	170	180	184	169
200	202	201	190	194	200	189
217	215	216	209	210	217	217
252	245	251	242	243	250	249

	267		254	254	261	264
276	280	276	266	267	274	278
	296*					
	307*	318	301	302	316	317
	315*				330	333
336	341	334	318	320	335	336
	353		322	327		
375	360	374	351	364	373	369
387	381	387	366	369	387	385
400	412	400	375	390	399	395
		429	394	416	415	414
426	439	416	396	410	425	419
462	470	462	440	455	462	464
474	502	476	445	455	475	478
530	556	531	504	507	531	531
589	570	589	550	580	587	577
607	628	611	575	585	611	607
648	643	650	620	626	649	652
722	713	732	688	693	722	724
742	725	744	707	714	744	745
760	749	761	725	727	762	762
786	792	781	752	758	788	791
988	969	994	923	961	993	968
1004	1007	1018	954	975	1014	998
1032	1036	1040	984	1028	1037	1030
1048	1054	1058	984	1028	1051	1034
1096	1098	1102	1046	1069	1096	1091
1106	1120		1053	1060	1109	1107
1142	1145	1142	1089	1149	1137	1126
1160	1175	1162	1107	1161	1162	1161
$\overline{\lvert\Delta\upsilon\rvert}$	10.9		30.8		5.1	
$\lvert\Delta\upsilon_{max}\rvert$	28		74.0		24.9	

* The frequencies at 296, 307 and 315 cm^{-1} are calculated by McKeown[38] and attributed to weak modes within the low-frequency shoulder of the 336 cm^{-1} band, while Von Stengel[49] did not place anything within this frequency range.

36 A_u modes are counted in both LD and DFT computations: 33 frequencies are common, two are listed only in DFT methods, and one (*i.e.*, 296 cm^{-1}) is presented only in LD calculation and has no correspondence with any experimental infrared bands. The mode at 315 cm^{-1} found in LD has been correlated with our calculated mode at 333 cm^{-1} (observed at 330 cm^{-1}). Finally, the computed modes at 353 (LD) and 322-327 cm^{-1} (DFT-PBE) do not correspond to any frequency in our calculation and they are not present in the experimental spectra reported in refs [38,40,49,58].

4. THE HP-RAMAN EXPERIMENT ON LOW ALBITE

The behaviour of feldspars upon compression has been deeply studied in order to understand the mechanisms that control the elastic properties of the crustal materials, in view of their abundancy in the Earth's crust (~ 60% of its total volume)[9,34,59–66]. A comprehensive knowledge of the response of the feldspar structure to temperature and pressure is a key-point to a deeper understanding of the geochemistry of igneous and metamorphic processes of the crust and the upper mantle of the planet. Feldspars are significantly stiffer than other framework silicates such as quartz[67] or zeolites[68], but among rock-forming minerals they are softer than (non-framework) olivine and pyroxenes[62]. The pressure range over which feldspars are thermodynamically stable is limited to ~1 GPa in geological environments[34,64], and they become metastable at higher pressures: in particular, albite and anorthite are restricted to the crust and uppermost mantle (pressure less than 2 GPa), whereas sanidine is stable to at least 4 GPa. Nevertheless, compressional studies at higher pressures (under non-equilibrium conditions) provide more accurate elastic data, necessary to model the thermodynamic properties of these minerals. In addition, numerous shock experiments have been carried out to investigate diaplectic glasses with feldspathic composition, as maskelenyte, which are commonly found in natural meteorites[43,47].

Among feldspars, the thermoelastic behaviour of albite has deserved special attention[69,70]: it shows significantly higher thermal expansion than other plagioclases, almost twice than anorthite, lower Einstein temperature and more anisotropic thermal deformation. Moreover, the unit-cell volume of albite is out of a linear trend respect to other plagioclase at almost any temperature. At

high pressure, recent determinations of the equation of state (EoS) data of plagioclases[34,62,71] revealed that albite shows an unusual compressional behaviour.

In this chapter, the results of an in-situ high-pressure Raman spectroscopic study on a single-crystal of low albite are presented, in order to describe the high-pressure spectroscopic features of this feldspar, and their potential correlations with its elastic anomalies previously reported by in-situ high-pressure X-ray diffraction experiments[34,72]. Potential correlations between structure (*e.g.*, bond length and angle variations) and spectra (*e.g.*, wavenumber shifts) are described.

4.1 The experimental setup

The high-Pressure micro-Raman experiment was performed using an ETH-type diamond anvil cell (DAC), along with our spectrometer.

DACs are devices designed to generate and maintain high hydrostatic pressure conditions in order to perform in-situ experiments by various experimental techniques (*e.g.*, single-crystal X-ray diffraction or infrared, Raman and UV spectroscopies). A schematic view of the DAC components is given in Figure 4.1. The sample under investigation is confined in a small pressure-chamber (diameter: 150-300 μm), usually obtained by spark-erosion in a metal foil (called "gasket", Fig. 4.1). The quasi-hydrostatic environment around the sample is ensured by a *P*-transmitting fluid, which fills the gasket hole. Pressure is applied by a system of screws, forcing the two opposite diamond anvils against the metal gasket. The gasket is deformed plastically and transmits the pressure to the *P*-fluid, which in turn compresses hydrostatically (or quasi-hydrostatically) the sample under investigation. The gasket shear strength and thickness, along with the diameter of the gasket-hole, affect the maximum pressure that can be reached. The pressure range is also limited by the fluid-glass transition of the media used (*e.g.*, it is close to 10 GPa for a 4:1 methanol-ethanol mix[73]). The pressure on the sample is calibrated by an internal pressure sensor, which is loaded in the pressure-chamber along with the sample. Ruby is usually used as *P*-sensor in H*P*-Raman

experiments (Figure 4.1), as the pressure can be estimated by the "ruby-fluorescence method" (*i.e.*, fluorescence peak shift in the Raman spectra, precision of ± 0.05 GPa)[74,75].

The DAC employed for the experiments of this thesis was designed by Miletich *et al.*[76]. Type-II diamonds were used as anvils (culet ∅ 600 μm). Stainless-steel T301 foil, 250 μm thick, pre-indented to a thickness of about 100 μm and with a 300 μm hole obtained by electro-spark erosion, was used as a gasket. Methanol:ethanol = 4:1 mixture was used as hydrostatic pressure-transmitting medium.

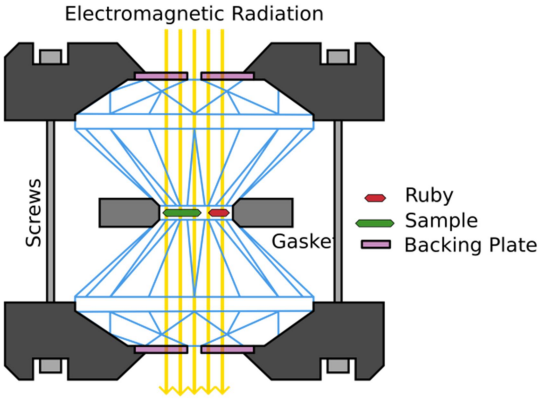

Figure 4.1: Schematics view of a diamond anvil cell[77].

The experiment was performed on a single crystal of low albite from Minas Gerais (Brazil), approximately 120x100x20 μm^3 large. Chemical analysis, unit-cell parameters and other structures details of the sample are listed in detail in Appendix A and Appendix B .

The crystal was placed in the gasket hole along with some ruby chips for pressure measurements. Raman spectra were collected in the pressure range 10^{-4} (P_{amb}) - 10.4 GPa: 16 measurements in compression mode and 6 in decompression mode. The sample and the ruby were excited with the 473.1 nm blue light of a Nd:YAG laser. The laser beam was focused on the sample with a spot diameter of nearly 2 μm (objective 50x ULWD, NA=0.55), using a confocal aperture of 150 μm. The spectral resolution was 3.5 cm^{-1}. Unpolarized Raman spectra were collected in backscattered geometry in the spectral range 100-2000 cm^{-1}, with 60-90 s counting time and 6-10 accumulations. Ruby fluorescent spectra were acquired for 5 s, accumulated 5 times. Both spectra were calibrated using the emission lines of a spectroscopic Zn lamp. At each pressure increase, the

Raman spectra were performed after a few minutes, in order to allow an elastic relaxation of the system.

The position of the Raman and fluorescence bands was determined by a pseudo-Voigt deconvolution procedure (LABSPEC 5.78.24 software package, Jobin Yvon/Horiba).

Albite crystal lays with the (010) cleavage face parallel to the culet face of the anvil. The laser polarization did not correspond to any rational crystallographic direction. The same orientation of the laser beam with respect to the crystal was kept for all the spectra.

Raman spectra of albite were analysed as follows:

- spectral range 120-900 cm^{-1},
- subtraction of a 6^{th} degree polynomial baseline,
- normalization to the intensity of the strong Raman band at 508 cm^{-1} (P_{amb}),
- peak fitting in the range 140-850 cm^{-1}, using as reference positions the Raman shifts of low albite calculated at ambient P,T (see Chapter 3).

4.2 Results

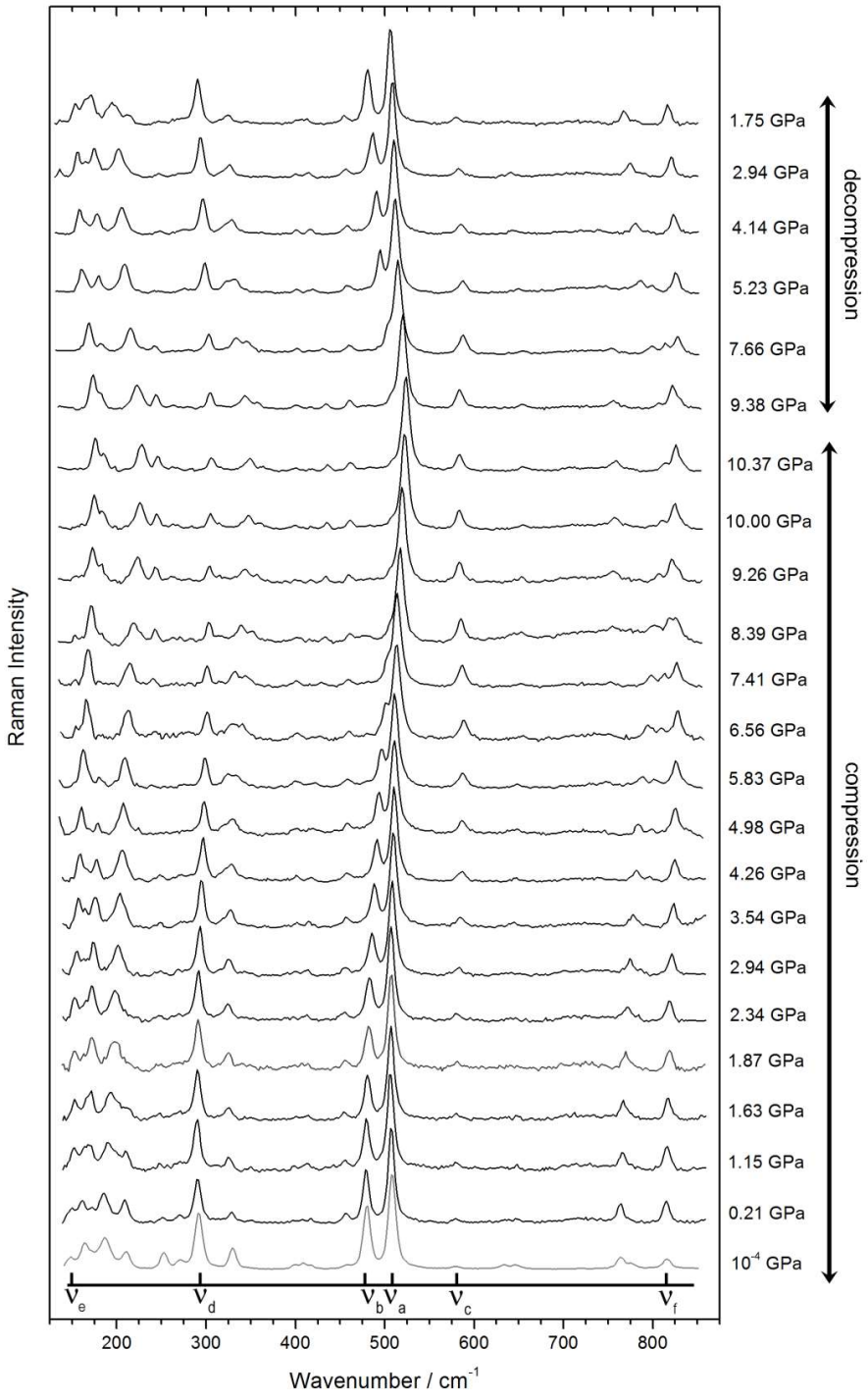

Figure 4.2: Pressure evolution of the low albite Raman spectrum during isothermal (T = 25 °C) compression and decompression, from 10^{-4} to 10.4 GPa and vice versa. Pressures are indicated in gigapascal at the right side of the graph. The spectrum at 10^{-4} GPa (P_{amb}) was collected on the crystal in air (*in grey*).

A total number of 16 + 6 *in situ* Raman spectra were collected on an unoriented albite crystal (Figure 4.2). Out of the 39 A_g modes expected by factor group analysis, only 25 modes were observed at P_{amb} when the sample is loaded in the DAC. The major features of the Raman spectra collected at ambient conditions were preserved at higher pressures and no evidence of amorphisation effects was observed neither at the highest pressure achieved in this experiment. A general blue-shift towards higher wavenumber is observed during compression, whereas a red-shift in decompression makes the experiment reversible.

The Raman setup did not enable the recognition of albite Raman features at wavenumbers below 140 cm^{-1} and above 850 cm^{-1}. Additional Raman bands at 880 and 1000 cm^{-1} were observed in raw data and assigned to the methanol-ethanol pressure-fluid, whereas the strong peak centred at 1330 cm^{-1} was due to the diamond. Some of the weakest Raman bands of low albite disappear when pressure increases, especially at low wavenumbers: *e.g.* the number of the observed Raman modes below 250 cm^{-1} decreases from 7 to 4 at 2.9 GPa, therefore, the pressure evolution of the Raman features in this range cannot be determined with certainty (see for example Figure 4.3). The lack of some Raman features in the spectra collected at higher pressures is due to a general deterioration of the Raman signals when pressure increases and to band overlapping. This phenomenon is well shown by the characteristic doublet peak which becomes a single band starting from about 8 GPa (see Figure 4.4).

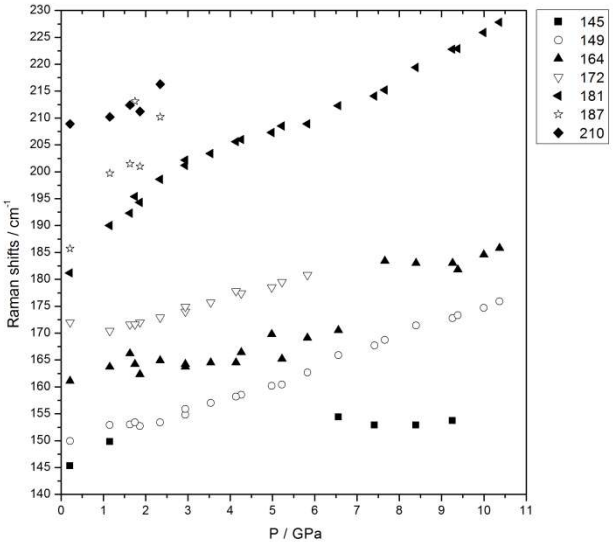

Figure 4.3: Pressure evolution of Raman bands below 230 cm^{-1}. Raman modes at 149 (ν_e) and 181 cm^{-1} show continuous and smooth trends, the other ones display discontinuities and their pressure evolutions are not easily identifiable.

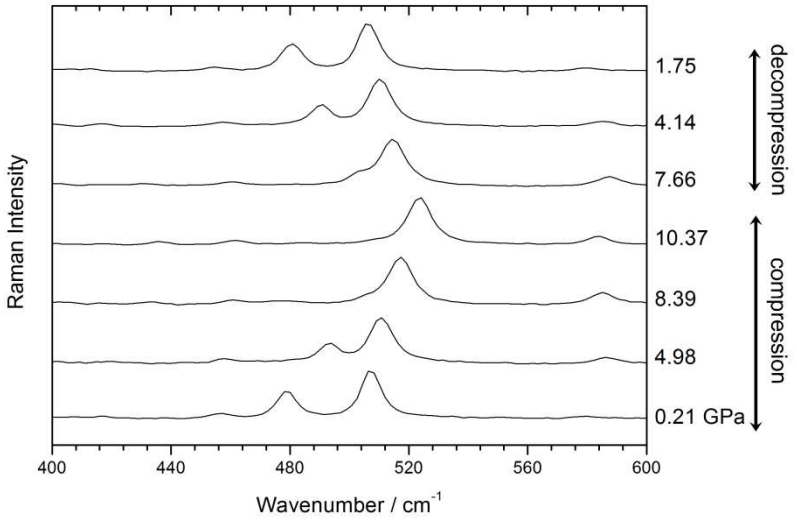

Figure 4.4: Evolution of the characteristic doublet peak at some selected pressures.

The evolution of some selected Raman modes with pressure is displayed in Figure 4.5. They correspond to the 507, 478, 578, 290, 149 and 815 cm^{-1} Raman modes (wavenumbers refer to those found in the Raman spectrum at RT and 1 atm) and will be labelled as υ_a, υ_b, υ_c, υ_d, υ_e and υ_f.

The observed maximum Raman shifts are: $\Delta\upsilon_a = 16.2\ cm^{-1}$, $\Delta\upsilon_b = 29.1\ cm^{-1}$, $\Delta\upsilon_c = 4.2\ cm^{-1}$, $\Delta\upsilon_d = 15.7\ cm^{-1}$, $\Delta\upsilon_e = 26.0\ cm^{-1}$ and $\Delta\upsilon_f = 17.3\ cm^{-1}$. In Figure 4.5 linear fits to the $\upsilon_i(P)$ curves are shown. Except for Raman band υ_e, which displays a constant $\Delta\upsilon/\Delta P$ slope over the entire pressure range, all the investigated Raman modes reveal an abrupt change at ~6.5 GPa (see Table 4.1). Moreover, Raman band υ_f shows a further change in $\Delta\upsilon/\Delta P$ slope at 8.5 GPa.

Table 4.1: Raman shifts as a function of pressure for six investigated Raman modes.

		Below 6.5 GPa		Above 6.5 GPa		Above 8.5 GPa	
Modes	$\lvert\Delta\upsilon\rvert_{0\text{-}10.4\ Gpa}$ (cm^{-1})	$\Delta\upsilon/\Delta P$ ($cm^{-1}GPa^{-1}$)	uncertainties ($cm^{-1}GPa^{-1}$)	$\Delta\upsilon/\Delta P$ ($cm^{-1}GPa^{-1}$)	uncertainties ($cm^{-1}GPa^{-1}$)	$\Delta\upsilon/\Delta P$ ($cm^{-1}GPa^{-1}$)	uncertainties ($cm^{-1}GPa^{-1}$)
υ_a	16.2	1.1	0.1	2.9	0.2		
υ_b	29.1	3.6	0.1	1.9	0.3		
υ_c	4.2	1.8	0.1	-1.4	0.2		
υ_d	15.7	1.9	0.1	1.3	0.1		
υ_e	26.0	2.7	0.1				
υ_f	17.3	2.2	0.1	-0.5	0.5	3.1	0.4

Peak linewidths of the investigated modes show an increase of about 2-2.5 cm^{-1} per GPa.

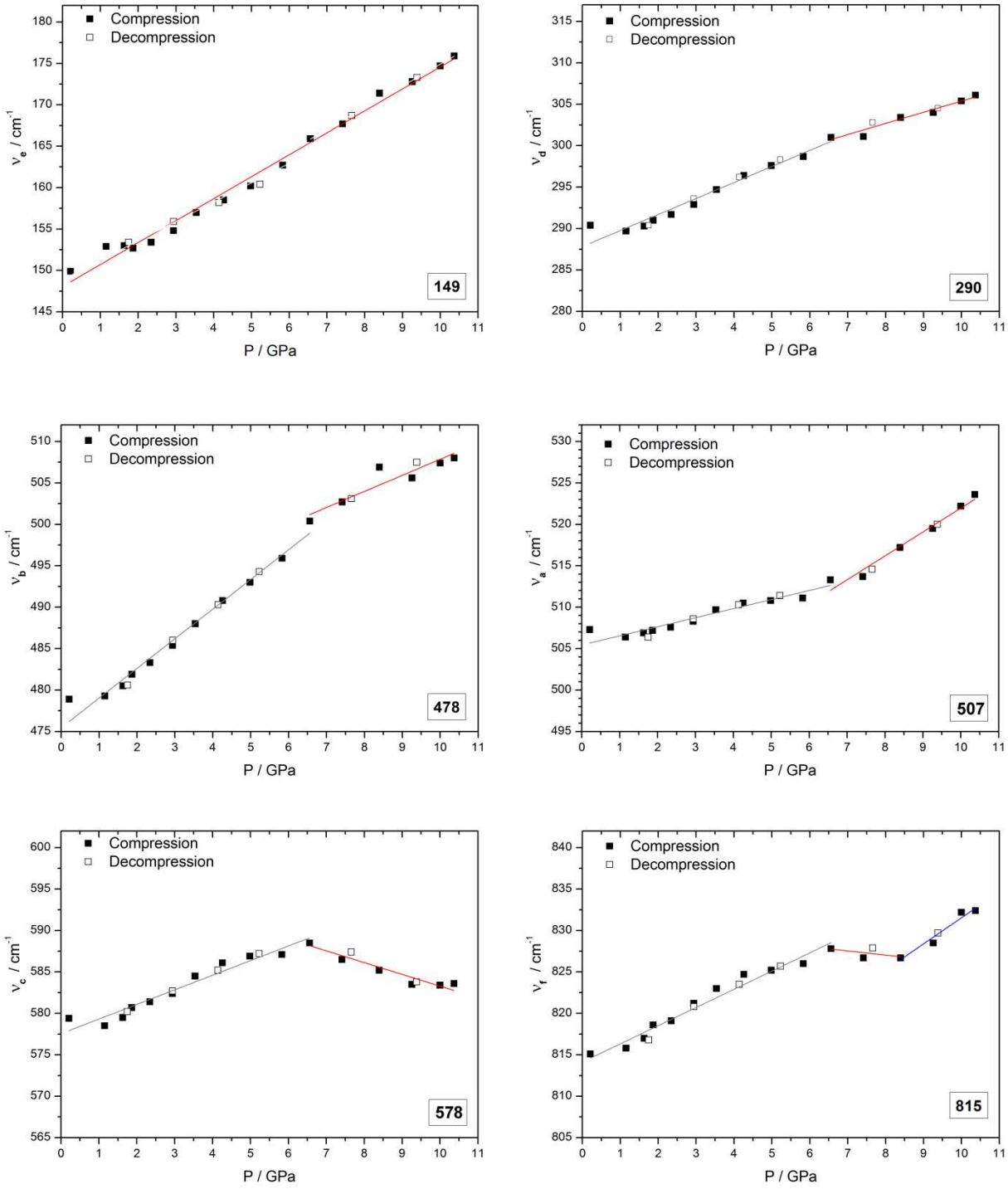

Figure 4.5: Pressure evolution of some selected Raman bands. Full and empty symbols correspond to the compression and decompression ramps, respectively. Lines are least square fits to data.

4.3 Discussion

When pressure increases, the distances between the building units forming the albite framework decrease and promote stronger Coulomb repulsion, which expresses in a general blue-shift of the Raman wavenumbers, as observed here. Such an increase occurs with different $\Delta\upsilon/\Delta P$ slopes for the different modes, and, for each mode, a change in slope at a given pressure is observed. This is likely due to differential compressional mechanisms for the building units involved in each of the Raman modes, and for the change of this mechanism at some "critical" pressure. In literature[9,63], these variations have been explained by the tilt of essentially rigid tetrahedra.

In order to describe the behaviour of the Raman modes, it is useful to consider first the mechanisms that govern the structural evolution of albite as deduced on the basis of the high-pressure X-ray structure refinements. Previous high-pressure single-crystal X-ray diffraction studies[34,64] showed that no phase transition occurs in low albite and its structure remains triclinic at least up to 9.43 GPa. The closing-up of the crankshaft chains within the structure is the dominant mechanism of compression and is responsible for the extreme anisotropy of compression that is typical for all feldspars[62,66]. Nevertheless, albite reveals a more complex behaviour that has previously observed in feldspars. Two secondary compression mechanisms act at different pressures: below 4 GPa, albite exhibits compression of the crankshaft chains, without rotation of T_1 tetrahedra, and consequent shear of the rings; above 4-5 GPa T_1 tetrahedra start to rotate around the [001] direction and albite becomes softer, as observed in plagioclases at lower pressures[62]. A further change is observed above 8 GPa, which causes a severe softening of the structure as a whole, while at the same time some directions tend to expand (*i.e.*, [110]). In Benusa *et al.*[34] this last behaviour has been interpreted as an elastic instability of albite at higher pressures, resulting in a phase transition or due to an impending pressure-induced amorphisation similar to that found in anorthite and quartz. Calculation of the strain tensor[78] from the unit-cell parameters showed that the direction of maximum compression is close to the (100) plane normal and that this direction accommodates about the 65% of the volume compression of the framework. This anisotropic behaviour can be ascribed to the response of the tetrahedral framework to pressure. Angel *et al.*[9,63] showed that all the essential features of the structures (*i.e.*, unit-cell parameters and volumes, their expansion and compression induced by changes in pressure, temperature, and composition) are generated by the

tetrahedral tilting and that the fundamental reason for feldspars anisotropy lies in the topology of the tetrahedral framework. In particular, they suggest that four tilts (Figure 4.6) are allowed in a ring of four corner-linked tetrahedra with point symmetry 2 [8,79] and that the O-O repulsions control the values of these tilts and, therefore, the anisotropy of the structure, because tilts maximize the shortest O-O distances in the structure.

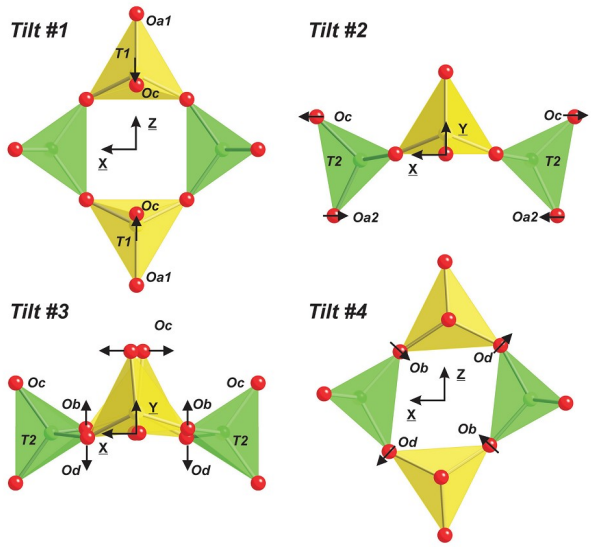

Figure 4.6: The four tilt patterns of the tetrahedra in a four ring from Angel *et al.*[9], preserving the point symmetry 2: Tilt #1, rotation of T_1 tetrahedra around the O_B-O_D edge; Tilt #2, rotation of T_2 tetrahedra around the O_B-O_D edge; Tilt #3, mutual rotation of the two T_2 by equal but opposite amounts around a*; Tilt #4, shear of the ring within the (010) plane. Black arrows indicate the most significant displacements of oxygen atoms.

Going back to our Raman data, we observe that all the investigated modes show a monotonic evolution (with a resulting stiffening of the structure) from ambient *P* to about 6 GPa. Except for υ_e, they display a change in behaviour at a pressure of ~6.5 GPa. Raman data suggest that the internal structural changes are confined to a small pressure interval, localized around 6 GPa, not spread out from 4 to 8 GPa as suggested by previous X-rays studies on elasticity. This behaviour is more similar to that expected for a phase transition; however, it is not a true transition, as proved by the X-ray structure refinements, which show only a change of the elastic behaviour. Moreover, whereas most modes again evolve smoothly above 7 GPa, some high-frequency modes (*e.g.*, υ_f) show additional changes in slope at 8-9 GPa. The Na modes (*e.g.*, υ_e) show the most pronounced changes

in slope with pressure, consistent with the idea that Na atoms are just 'pushed around' by the framework and that the cavity is rapidly compressed.

Interesting similarities can be found if we compare Raman and structural data. If we look at the pressure evolution of the T-O-T bond angles and the O-O-O angles measured by Benusa *et al.*[34], we see that they show a change in slope at $P \geq 6$ GPa. In particular, the most spectacular structural changes reflect the reduction in the T-O_B(o)-T and T-O_C(o)-T bond angles, which results in the closing-up of the crankshaft chains, and the shear of the four-membered rings of tetrahedra. The latter phenomenon results in the narrowing of the channels, which is responsible for the softness along the (100) plane normal, that is typical of the compression of all feldspars[34,62,72]. If we consider the structural changes in terms of tetrahedral tilts, we have to keep in mind that tilts are only a measure of the response of the structure interpreted in terms of non-deforming tetrahedra, and so tilts do not include the internal deformation of the tetrahedra. Therefore, the variation in tilts might be expected to correlate especially with the framework bending modes (*i.e.*, υ_a, υ_b and υ_c). In triclinic feldspars, there are four non-equivalent tetrahedra, so four individual tilts of the tetrahedra with respect to the ring: tilt #1 will be split in T_1(o) and T_1(m) tilts, as tilt #2 in T_2(o) and T_2(m) tilts. In refs[9,63] these pairs of tilts were averaged. The pressure evolution of tilts in triclinic structures is shown in Figure 4.7. They have been recalculated from the experimental data of Benusa *et al.*[34] and Downs *et al.*[72], using the definition and the protocol of calculation reported in Angel *et al.*[9]. In Figure 4.8, the correlation between the change in O-O-O angles and tilt #4 (*i.e.*, shear of the ring) is displayed. It is clear that the rate in the variation of all tilts changes significantly at 6 GPa.

Raman mode υ_b shows the most pronounced Raman shifts within the investigated pressure-range (*i.e.*, ~29.1 cm^{-1}). If we compare the vibrational patterns of υ_b with those of υ_a and υ_c, it is apparent, especially in the *ab* projection, that the oxygen atoms of the tetrahedral cage move to opposite directions: mode υ_b squeezes the cage inwards, whereas the other two modes stretch the cage outwards (see Figure 4.9). Change in the T-O-T and O-O-O angles result in the narrowing of the tetrahedral cages, which implies an increase in the Coulomb repulsion between atoms, resulting in a blue-shift in the spectrum. The atomic configuration of mode υ_b suggests a major repulsion between oxygen atoms than the other studied bending modes.

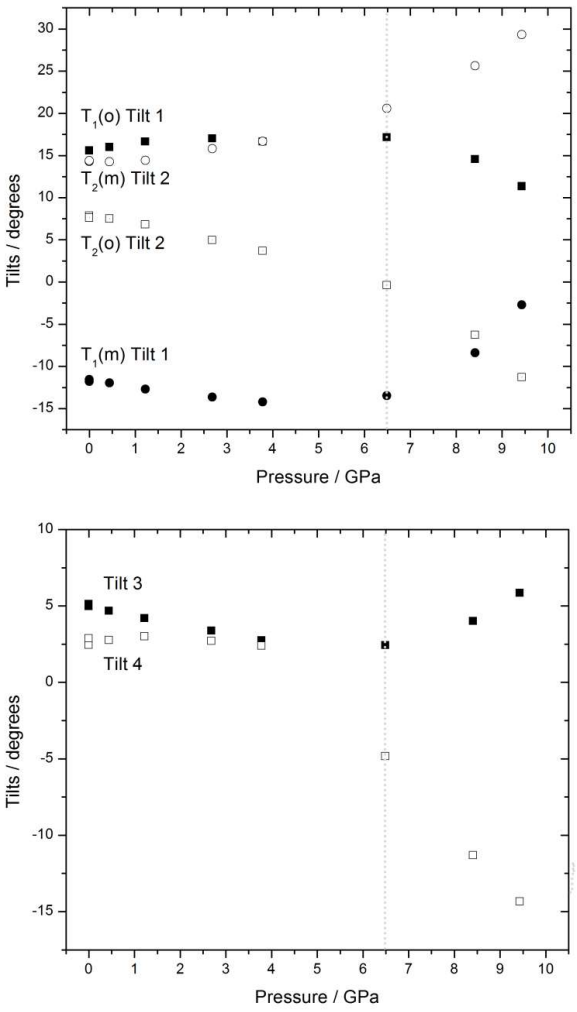

Figure 4.7: Plots of the four possible tilts in the alkali-feldspar structure as a function of pressure. Tilts have been defined and calculated according to Angel *et al.*[9]. Data come from the refinements of Benusa *et al.*[34] and the lower-P refinements by Downs *et al.*[72].

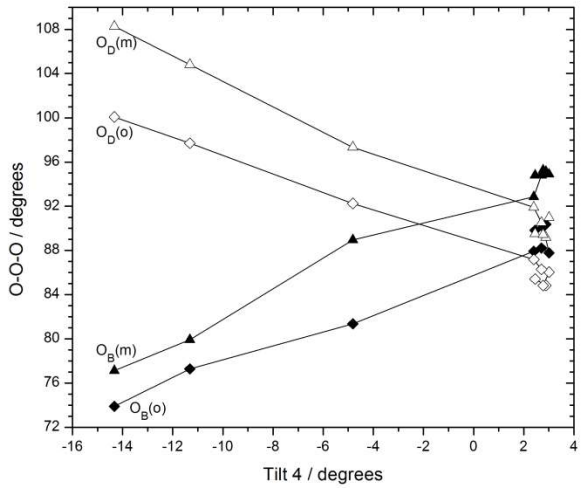

Figure 4.8: The shear of the four-membered ring of tetrahedra. O-O-O angles come from Benusa *et al.*[34]; tilt #4 is defined in Angel *et al.*[9] along with the protocol for its calculation. Lines are drawn as guide to the eye.

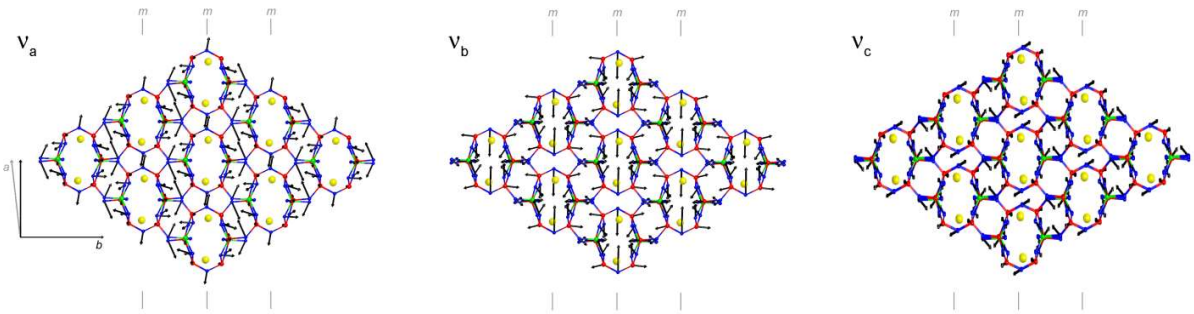

Figure 4.9: Vibrational patterns of the modes corresponding to the Raman bands υ_a, υ_b and υ_c.

At pressures above 6.5 GPa, an opposite behaviour for the bending modes υ_a, υ_b and υ_c is observed: Raman band υ_a exhibits steeper $\Delta\upsilon/\Delta P$ than the modes υ_b and υ_c, whose slope changes its sign, too (see Table 4.1). A different relationship is also found if we plot the bending modes as a function of both tilts #2 (*i.e.*, rotation of T_2 tetrahedra around O_B and O_D edge). To do this, we extracted the values of tilts corresponding to our set of pressures by linear interpolations from literature data [34,72]. Only υ_a shows a single linear trend (see Figure 4.10). Similar trends have been found between the three investigated bending modes and the other possible tilts: in Figure 4.11, the correlation between υ_a, υ_b and υ_c with tilt #4 is shown as an example. A deeper discussion on the vibrational behaviour of these modes above 6.5 GPa would need new DFT simulations at high pressure, in order to understand how the compression affects the different modes.

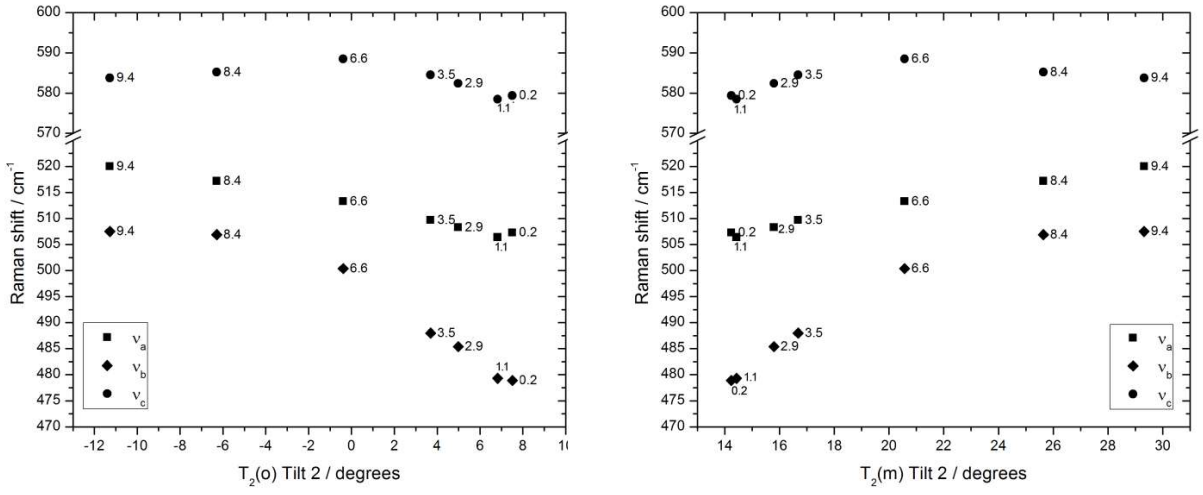

Figure 4.10: Correlation between the bending modes υ_a, υ_b and υ_c and the two tilt #2 (*i.e.*, rotation of T_2 tetrahedra around O_B-O_D edges). Labels show the pressure values at which we performed the Raman analyses.

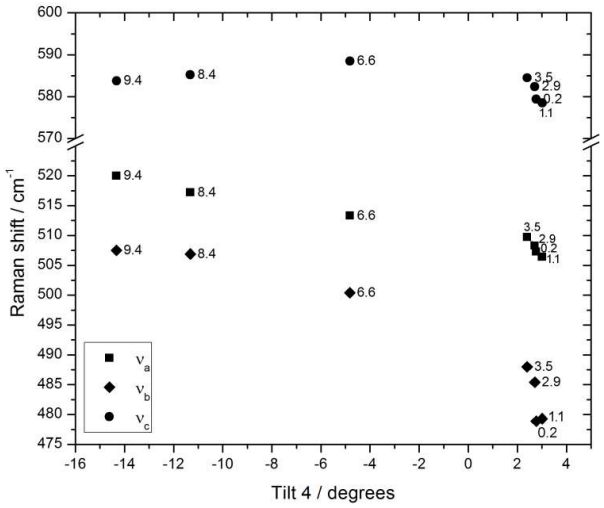

Figure 4.11: Correlation between the bending modes υ_a, υ_b and υ_c and tilt #4 (*i.e.*, shear of the ring). Labels show the pressure values at which we performed the Raman analyses.

Raman mode υ_f is a deformation mode, mainly of the T_1(m) and T_2(o) tetrahedra, but with a stretching component. Its behaviour with pressure has been described by three linear fittings: a first change in slope at 6.5 GPa and a further one at 8.5 GPa. The latter variation coincides with the severe softening of the structure as a whole observed above 8 GPa in X-rays data[34].

Raman mode υ_d consists mainly of rotations of the tetrahedra. Diffraction data[34] showed a significant rotation of the T_1 tetrahedra from P = 4-5 GPa, similar to that observed in coesite at lower pressure, leading to the softening of the structure. The vibrational mode localizes the structural changes at a higher pressure than that observed by X-ray diffraction (*i.e.*, 6.5 GPa).

Raman mode υ_e changes linearly over the entire pressure range. This band is related mostly to the Na atomic vibrations, in particular it was assigned to Na translations within the tetrahedral cage. Consistent with the model that the Na atoms are just 'pushed around' by the framework above pressure[34,72], and that the cavity tends to be rapidly compressed, the mode exhibits the largest change with pressure. Its vibrational behaviour under compression suggests that Na atoms play a completely passive role in the deformation of the structure. In fact, Na atom does not change its coordination number at all the investigated pressures, despite the significant decrease in the Na-O distances, in contrast to microcline, where K atoms increases its coordination number, by bonding the additional O_B(m) atom as the framework is compressed[64].

Changes in peak linewidth are not significant and confirm the hypotheses reported by Angel *et al.*[66] that the state of Al-Si order within the feldspar framework does not have a major effect on the compressibility of the alkali structure, as already observed comparing the compressional behaviours of low albite and high sanidine.

In conclusion, we can summarize our results as:

- the six investigated Raman modes show a smooth evolution (stiffening) from room pressure to about 6.5 GPa and, excluding the mode involving Na atoms, a significant change in their vibrational behaviour at about 6.5 GPa;
- the mode at 815 cm^{-1} shows a further change at about 8 GPa;
- both the evolution of spectra (in terms of number of observed modes) and the discontinuity in the *P*-induced shift of individual band positions might suggest the presence of a phase transition, but this assumption is invalidated by the in-situ SC-XRD data collected at high pressure[34,72];
- in albite, the dominant compression mechanisms act *via* tetrahedral tilting[9,63], therefore, T-O-T bending modes are the most affected by pressure;
- Raman spectroscopy has allowed localizing around 6.5 GPa the change in the compressional behaviour of albite, whereas elastic effects[34,72] are spread out over a large *P* range (*i.e.*, 4-8 GPa).

5. THE Al-Si DISORDERING IN LOW ALBITE

Al-Si distribution in Na-feldspars has been an important topic since the discovery that albite changes its unit-cell parameters after annealing at high temperatures, and that this is due to a change of the ordering scheme in the tetrahedral sites (see Chapter 2 for more details). Much work was done to explain the kinetic behaviour of Al-Si ordering in feldspars and the formation of non-equilibrium states, with the expectation that a careful characterization of the degree of the Al-Si order and its fluctuations in natural minerals may lead to a quantitative interpretation of the thermal history of the surrounding rocks.

The most direct method for estimating the degree of order in feldspars is by structure refinement (see Appendix C), but there are some difficulties. Because Al^{3+} and Si^{4+} cations are very similar in scattering powers by X-ray diffraction (XRD), they cannot be distinguished by X-ray structure refinements, and thus the site occupancies cannot be determined by direct refinement of site occupancies. Several other methods have been devised for using X-ray structural data to determine Si, Al proportions in each tetrahedral site and hence the degree of order, mainly using the T-O bond distances. As neutron diffraction, XRD provides only a long-range order, *i.e.* an average of the site occupancies of all the examined unit-cells. The short-range order, *i.e.* the ordering coming from the nearest neighbour interaction, can be investigated only by spectroscopic methods.

Neutron Magnetic Resonance (in particular, magic-angle-spinning NMR) was employed to investigated the local order in aluminosilicates[80]. Infrared Spectroscopy (IR) was used by Salje *et*

al.[55] to correlate the shifts in positions, linewidths and intensity changes of infrared absorption bands with the degree of Al-Si ordering in disordered Na-feldspars. Already in 1986, Raman spectroscopy has proved to be extremely sensitive to phase transitions, ordering processes and early stage of exsolution in hypersolvus alkali feldspars[41].

A crucial point in handling with these techniques is that X-rays, NMR, infrared and Raman see different length scales: a feldspar like orthoclase will look fully ordered to NMR, but disordered to X-ray structure refinement, simply because NMR only measures immediate neighbour environments. So, the question is: is Raman spectroscopy suitable for the determination of the degree of Al-Si order in disordered albites?

Nowadays, the high spectral and spatial resolutions of the micro-Raman technique, combined with crystal structure data and recent mode assignments, could allow a deeper understanding on the ordering process and on how it affects the vibrational modes.

5.1 Description of the thermal treatment

The thermal treatments have been performed in the DIFEST Department of the University of Parma, following the experimental details reported by refs[55,56,81]. A LTD tube furnace, with a maximum operating temperature of 1200 °C, has been used. An Eurotherm PID temperature controller provided a temperature stability within ± 1 °C.

The starting material for the experimental runs was a low albite from Minas Gerais (Brazil). Its chemical analysis and its lattice parameters are given in Appendix A and Appendix B (see "untreated"). The albite block was crushed into fragments; 24 fragments with almost the same size were handpicked and loaded on an alumina crucible. The crucible was inserted in the furnace tube and heated at 1076 °C for 12 times, up to a total annealing time of 40 days. At each annealing stage, the crucible was extracted from the furnace and two fragments were collected and rapidly cooled in air. After cooling, each couple of fragments was measured by Raman spectroscopy at RT.

5.2 Description of the experimental setup

5.2.1 The Raman measurements

Raman analyses have been performed by a Horiba Jobin-Yvon LabRAM apparatus. A detailed description of the instrument can be found at paragraph 3.2.1.

A minimum of eight up to twenty spectra, equally divided between the two fragments, were collected for each annealing time. Before each measurement session, the system was calibrated against the 520.6 cm^{-1} phonon mode of pure silicon. Typical exposure times were of about 60-120 seconds, accumulated 3-6 times. Spectra were measured in the range 100-1100 cm^{-1} with a spectral resolution 1.5 cm^{-1}. The peak position was determined, with accuracy better than 0.5 cm^{-1}, by peak fitting, made with LABSPEC 5.78.24 software package, Jobin Yvon/Horiba, using pseudo-Voigt profiles, subdividing each spectrum in three spectral ranges. A 2^{nd} degree polynomial curve was subtracted as baseline to remove fluorescence background before peak fitting.

For each peak position and linewidth, the average value, the standard deviation (SD) and the standard error of mean (SEM) were calculated. Measurements from the same experimental run show SDs and SEMs of peak positions not larger than ± 1 cm^{-1} and ± 0.5 cm^{-1}, respectively, for the two most intense Raman bands at 507 and 478 cm^{-1} and the weaker band at 578 cm^{-1}, whereas they get worse (*i.e.*, ± 1.6 and ± 0.8 cm^{-1}) for the Raman band at 290 cm^{-1}. As regard peak linewidths, SDs vary between 0.9 and 3.4 cm^{-1}, according to the investigated band and time, and SEMs are in the range 0.3-1.1 cm^{-1}. Differences in peak broadenings, observed in Raman spectra collected on the same experimental run, are caused by inter-crystalline inhomogeneity, *i.e.*, by the presence of internally homogeneous crystals with different degrees of disorder coexisting in the polycrystalline sample. Similar results were found by Meneghinello *et al.*[81] in powder patterns of Stintino albites crystals, heated in the range 1050-1090 °C for different times.

The absolute intensities observed in our spectra change according to the crystallographic orientation of the sample with respect to the polarization of the laser beam.

5.2.2 The single crystal X-ray diffraction analyses

Single crystal X-Ray diffraction has been performed by an Xcalibur 4-circle diffractometer in order to have a direct determination of the degree of order. This was necessary for a comparison between the degree of order measured by Raman and a common measurement used in literature.

X-ray experiments have been executed at seven annealing stages (*i.e.*, 0, 11, 20, 25, 28, 32 and 40 days) on single crystals sampled from the polycrystalline fragments previously investigated by Raman. A detailed description of the instrument and the results of the structure refinements can be found in Appendix B . The formula used to calculate the order parameter Q_{od} by structure refinements is explained in detail in Appendix C .

5.3 Results

The good quality of the single crystal refinements (see *R* indexes in Table B. 1) rules out a degradation of the crystals after the investigated annealing stage, so we can suppose that this behaviour is shared by all the experimental configurations. On the 40th annealing day the albite structure is fully disordered (Q_{od} = 0.05).

Changes in unit-cell parameters at each annealing steps confirm that samples disorder with time. Unit-cell volumes are little influenced by Al-Si distribution (they change from 664.35 to 667.22 Å^3), whereas unit-cell parameters changes as expected from literature[82]: *a* changes little, *b* increases, whereas *c* decreases (see the *b*-*c* plot in Figure 5.1); β angle remained ~116°, whereas α and γ are sensitive to Al-Si order and both exceed 90° (the unit-cell parameters measured at each investigated stage are displayed in Table B. 1 in Appendix B). Anomalous values were measured at the 25th and 28th annealing day. They will be discussed in the following paragraph.

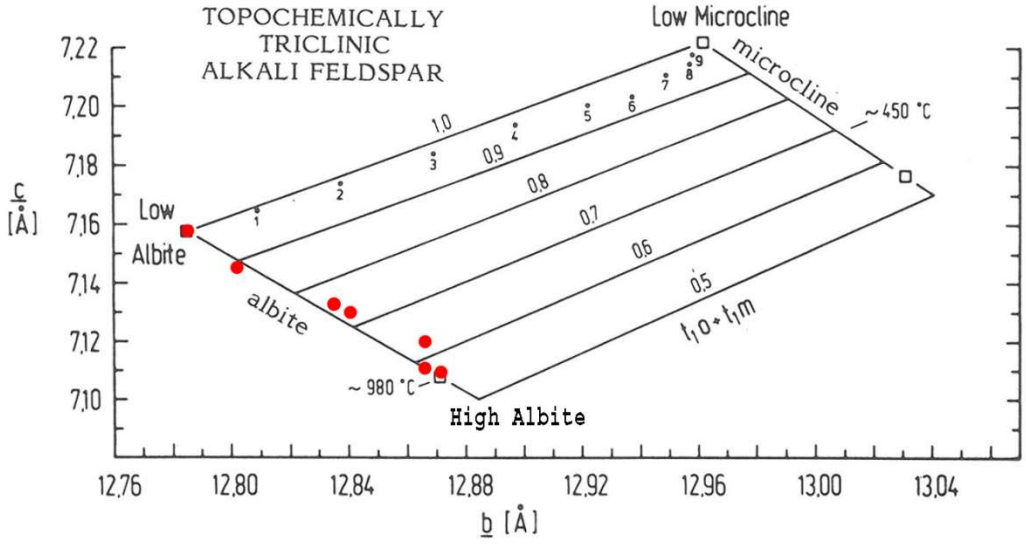

Figure 5.1: The *b-c* plot[83] to estimate ($t_{1(o)}$+$t_{1(m)}$). Our data (indicated as red circles) sit on the low albite-high albite line.

The order parameter Q_{od}, calculated as reported in Appendix C , shows a linear trend with the annealing time (see Figure 5.2). Bond distances of the four non-equivalent tetrahedral sites change linearly with the Al content, as expected from literature. The depletion of Al in T_1(o) produces a shortening in the T-O distances of the site, because of the difference in cation size and charge; vice versa, the migration of Al in T_1(m), T_2(o) and T_2(m) sites increased their sizes (Figure 5.3). In both graphs, two outliers are displayed again corresponding to the 25th and 28th step.

Changes in Al-Si order can be also described by the evolution of the spontaneous strain, *i.e.* the strain between the unit cells of albite with respect to that of the fully disordered one. Among the components of the spontaneous strain tensor, it was found the x_6 off diagonal component is most sensitive to changes in Al-Si distribution. As $x_6 = b\,cos\gamma/b_0 \sim \cos\gamma$, changes in cosγ are a probe of the Al-Si order[53,84]. In Figure 5.4 (*right*), a good correlation (R^2=0.99) between the cosγ and the order parameter Q_{od} of our samples, as well as those from the single crystal refinements from Meneghinello *et al.*[81], is found. In Figure 5.4 (*left*), the heating time evolution of cosγ is shown.

Analogous results can be obtained if other cell parameters are used to estimate the degree of order[82,85].

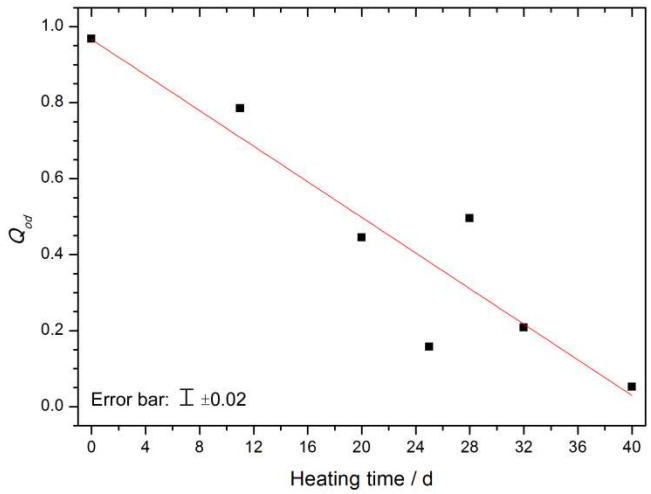

Figure 5.2: Time evolution of the order parameter Q_{od}, calculated from the refined T-O distances. A linear fit is shown (R^2=0.84).

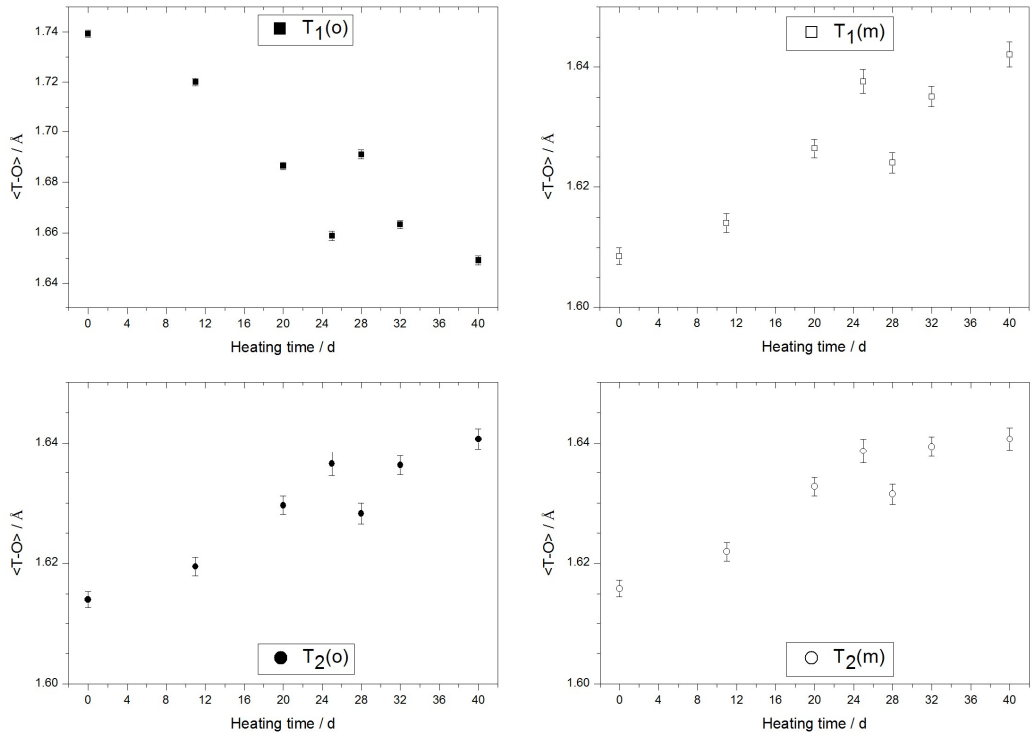

Figure 5.3: Evolution of the T-O distances as a function of heating time. The error bars range between 0.13 and 0.21 Å, according to the measurement point.

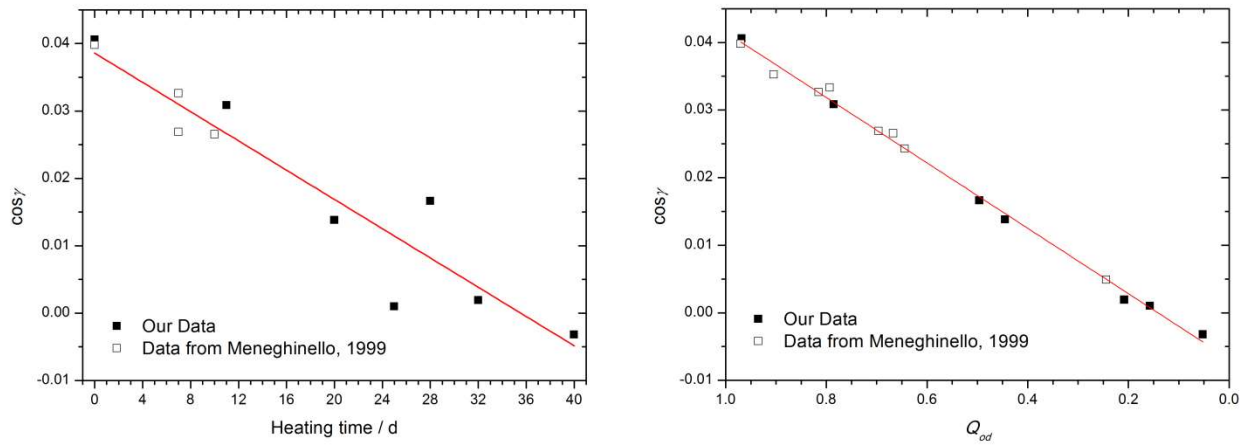

Figure 5.4: Correlation between cosγ and the heating time (*left*) and cosγ and the order parameter Q_{od} (*right*). Filled symbols indicate our data, empty symbols represent samples taken from literature[81]. Linear fits are shown (R^2=0.91 and R^2=0.99, left and right, respectively).

A sequence of 12 Raman spectra of albite, heated at a temperature of 1076 °C for different annealing times, is shown in Figure 5.5.

The spectrum of the starting material shows sharp Raman peaks. As the annealing time is increased, the Raman bands become broader, as expected, and the number of resolved bands decreases from 39 to 20 after 40 annealing days. This is particular evident at low and high wavenumbers where weaker and closer Raman features have been detected. As a signal broadening due to thermal degradation of the samples may be excluded, because the internal *R* agreement factors in single crystal measurements are low, we can affirm that the observed variations in the Raman spectra are related to changes in the Al-Si distribution.

To constrain the relations between shifts in position and linewidth of the Raman bands and the degree of order, we have chosen some peaks which could be resolved through all the annealing stages. After a visual inspection of the Raman spectra, we identified four modes as possible candidates: the doublet at 478 and 507 cm^{-1}, the peaks at 290 and 578 cm^{-1}. They will be labelled in the following as: υ_a = 507 cm^{-1}, υ_b = 478 cm^{-1}, υ_c = 578 cm^{-1} and υ_d = 290 cm^{-1}, because their positions will change during the experiment.

Because of Raman spectra were recorded at each annealing stage, and hence in different days, various calibrations of the spectrometer were performed before each measurement session. To

avoid errors in the comparison among the spectra, we checked both the shifts in positions and the wavenumber differences between peaks.

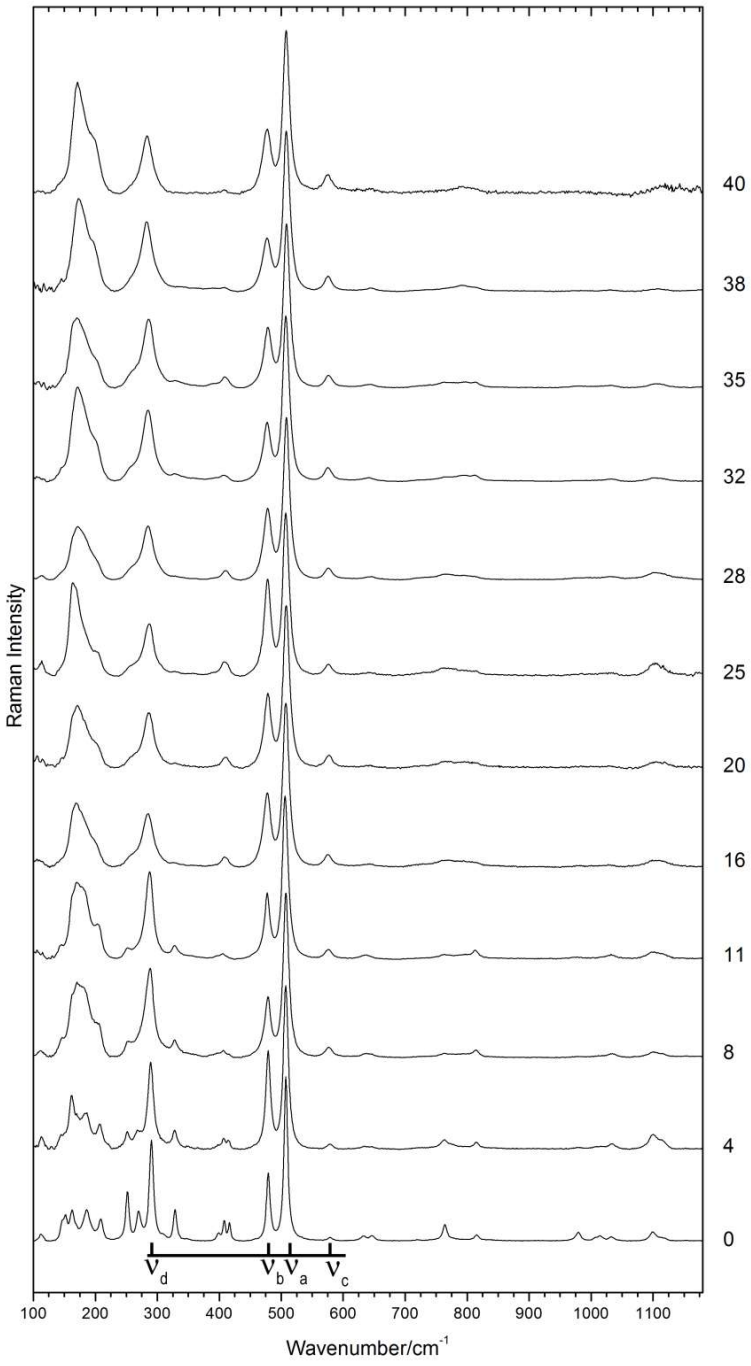

Figure 5.5: Raman spectra at RT of albite for various annealing times at 1076 °C in the spectral range 100-1100 cm^{-1}. The labels outside the right axis denote the annealing times (days).

In Figure 5.6, the time evolution of the positions of four Raman bands and their relative differences is displayed. For each Raman band, the average value of wavenumber is reported for each annealing step.

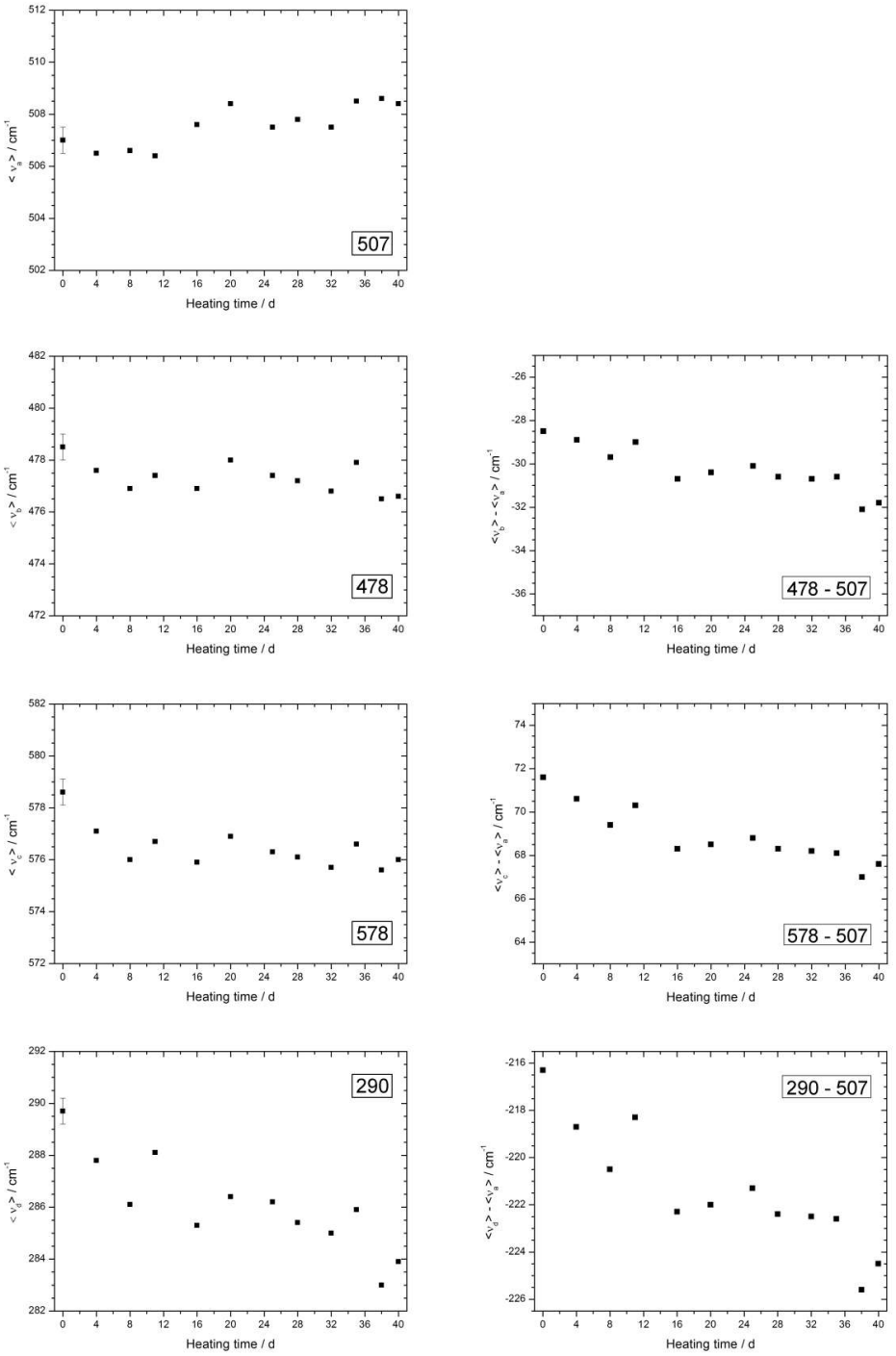

Figure 5.6: Evolution of the Raman bands and their respective wavenumber differences during the annealing. The estimated error on position (±0.5 cm^{-1}) is indicated only on the first point.

The wavenumbers of υ_a increase, whereas those of υ_b, υ_c and υ_d decrease with time. The relative distances between υ_b and υ_a, υ_c and υ_a and υ_d and υ_a decrease during the experiment. As concerns the changes in position, the measured absolute shifts are: $\Delta\upsilon_a = 2$ cm^{-1}, $\Delta\upsilon_b = 0.9$ cm^{-1}, $\Delta\upsilon_c = 1.7$ cm^{-1} and $\Delta\upsilon_d = 4.8$ cm^{-1}. Nevertheless, the SDs associated to each measurement are significantly high and this prevents a reliable interpretation.

If we consider peak linewidths, the measured shifts are: $\Delta\Gamma_a = 5.4$ cm^{-1}, $\Delta\Gamma_b = 8.1$ cm^{-1}, $\Delta\Gamma_c = 3.1$ cm^{-1} and $\Delta\Gamma_d = 12.8$ cm^{-1}.

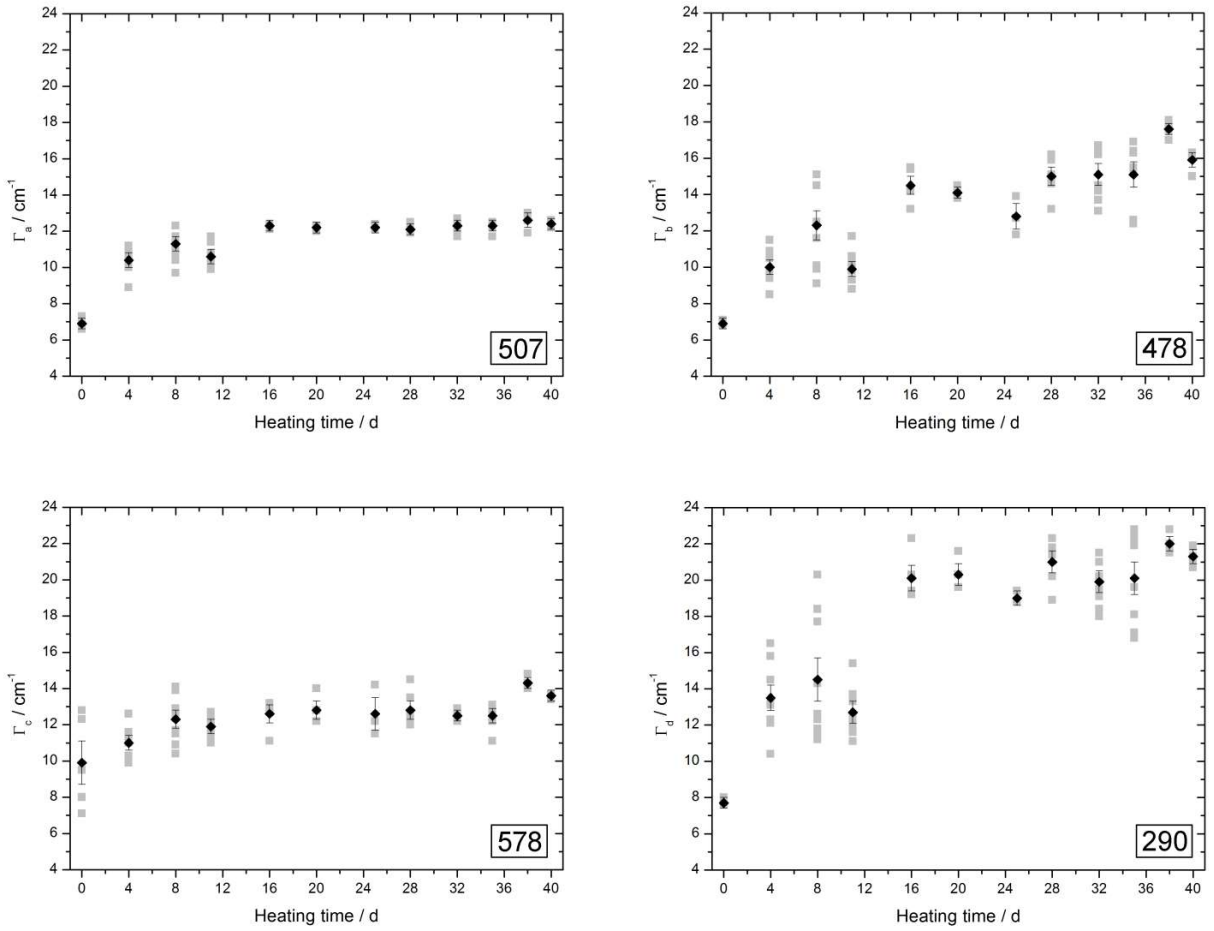

Figure 5.7: Evolution of linewidths of the four Raman bands during the heating experiment. Grey squares represent raw data; black diamonds are the average values with their errors.

In Figure 5.7, time evolutions of the four peak linewidths are shown, both as raw data and as average values. Looking at raw data, they are very much scattered at each annealing step, suggesting a heterogeneous disordering process within the samples probably due to the local defect density. On the contrary, average values highlight clearer trends, where the rates in peak broadening is faster in the first steps (till 11 annealing days) than in the further ones. From the 16th days, all the four linewidths get their maximum values. Γ_a seems to be less sensitive to local defect density from the 5th step forward, whereas the other three Γ are influenced at all times.

5.4 Discussion

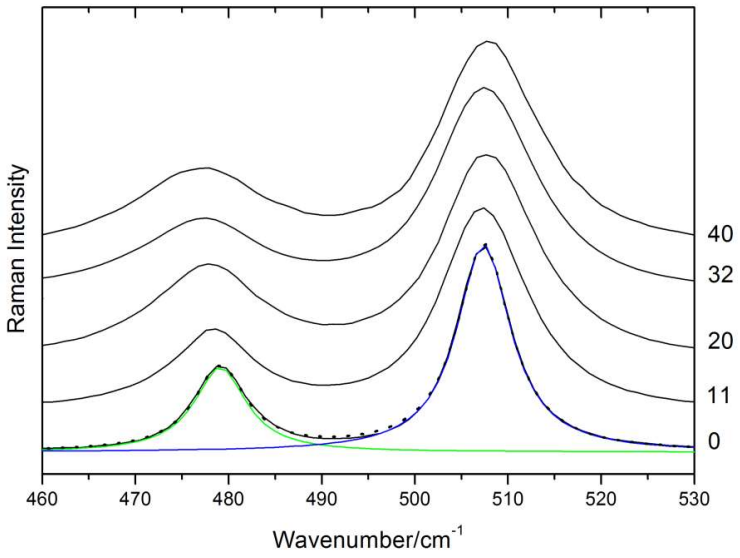

Figure 5.8: Evolution of the two most intense Raman peaks υ_a and υ_b at five characteristic annealing stages. Pseudo-Voigt profile analysis is displayed for the starting material.

The wavenumbers of the feldspars sharp characteristic peaks at 507 and 478 cm^{-1} can be determined with the highest accuracy (Figure 5.8). Their wavenumber difference decreases with time, but their absolute shifts are too small with respect to their SDs to be suitable for a deeper discussion. Raman band υ_d shows the highest shifts, both in position and in linewidth, but its $\Delta\upsilon_d$

and $\Delta\Gamma_d$ values could be overestimated. Even though it is a strong feature too, its behaviour with time could be influenced by the presence of the weaker band at 269 cm^{-1}, merging with it after 11 annealing days (see Figure 5.9). This band overlap could explain why band υ_d shifts about twice the amount of the other investigated bands. For this reason, we do not consider this band in the following discussion. Also the too weak Raman band at 578 cm^{-1} is not employed further.

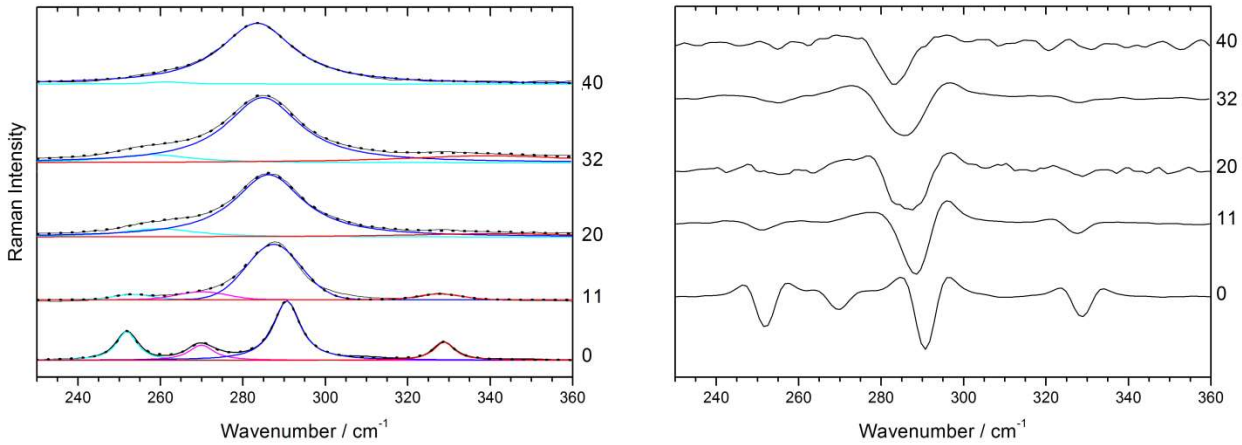

Figure 5.9: Evolution of the Raman bands in the range 230-360 cm^{-1} at five characteristic annealing steps (*left*) and the 2nd derivative of the spectra (*right*). Pseudo-Voigt profiles are displayed: 4 peaks have been used for steps 0 and 11, 3 peaks for the further steps in the peak fitting procedure. The weaker band at 269 cm^{-1} (magenta profile) vanishes after 11 days.

Peak broadening is therefore more sensitive than peak position to changes in the Al-Si distribution. Even though Raman data are scattered and there are outliers in the calculated Q_{od} values, the average linewidths of the Raman bands υ_a and υ_b as a function of the order parameter Q_{od} increase up to a saturation value (Figure 5.10).

The heterogeneity both in position and time of the disordering process was suggested by SC-XRD analysis and confirmed by Raman measurements. First of all, time evolution of Q_{od}, T-O distances and unit-cell parameters showed outliers at the 25th and 28th steps (see, for example, Q_{od} values in Figure 5.2). The anomalies found in SC-XRD can be explain if we look at the Raman data, which being more abundant have additional statistical information. Peak linewidths measured at each annealing step in different points are scattered (see Figure 5.7), because Raman analyses have been carried out on millimetre multi-grain samples. The inter-crystalline inhomogeneity, *i.e.*,

the presence of internally homogeneous crystals with different degrees of disorder coexisting in the polycrystalline sample, was already suggested by Meneghinello *et al.*[81] as a possible cause to explain line broadening observed in powder patterns of Stintino albite crystals, heated in the range 1050-1090 °C for different times. Raman analyses support this thesis and the absence of strongly developed microstructures in the used single crystals excludes the presence of intra-crystalline inhomogeneity. Heterogeneous disordering is probably due to the local defect density, which plays a crucial role during heat treatments of natural samples, locally favouring and accelerating the Al-Si distribution.

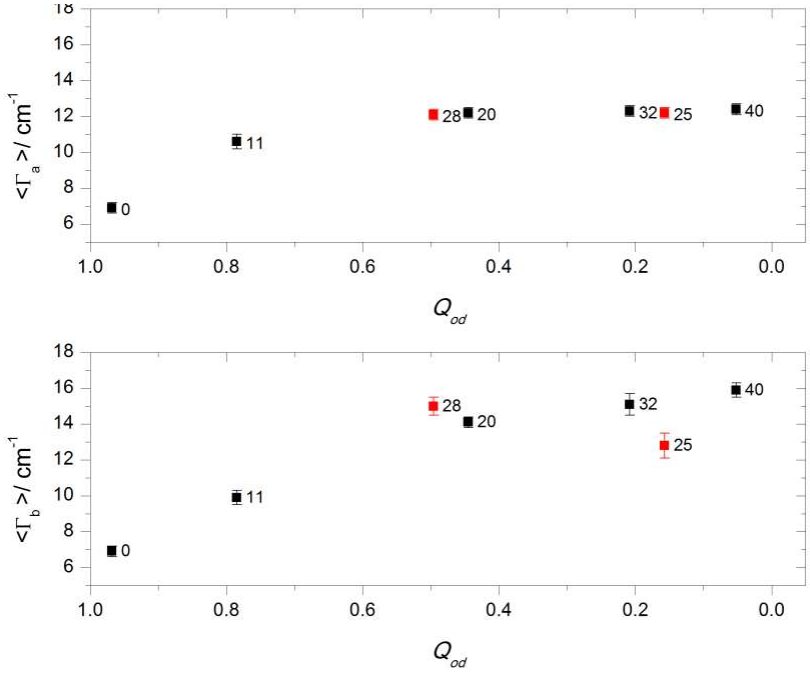

Figure 5.10: Average peak linewidths as a function of the order parameter Q_{od}. The outliers measured at the 25th and 28th steps are shown in red.

Our results are consistent with the high albite Raman spectrum reported by Freeman *et al.*[2], where a slight downshift in peak positions, except for the Raman band υ_a, and band broadening were observed compared to the corresponding peaks of low albite. In the heating study described by McKeown[38], peak broadening ranges from 9 cm^{-1} at RT to approximately 25 cm^{-1} at 1100 °C, whereas no shifting takes place for some features, such as modes υ_d and υ_a. The triclinic to

monoclinic transition is measured near 980 °C but no dramatic effects on the unpolarized Raman spectrum are noticed. An analogous spectroscopic behaviour is observed for infrared bands[55–57], where frequency shifts below 5 cm^{-1} and band broadening were measured. Moreover, Salje *et al.*[55] found that infrared spectral features, such as line position (Δν), linewidth (ΔΓ), and peak intensity (ΔA), scale with the square of the order parameter in alkali feldspars. The following relation is suggested:

$$\Delta\upsilon \propto \Delta\Gamma \propto \Delta A \propto Q_{od}^2,$$

where Δ indicates the difference between the measured value (*i.e.*, position, linewidth and intensity) and the reference value found at $Q_{od} = 0$ (the relation was applied also by refs[56,57]).

Assuming the same arguments, we could expect a similar trend between our ΔΓ *versus* the square of Q_{od}. The trends for the doublet υ_a and υ_b are shown in Figure 5.11.

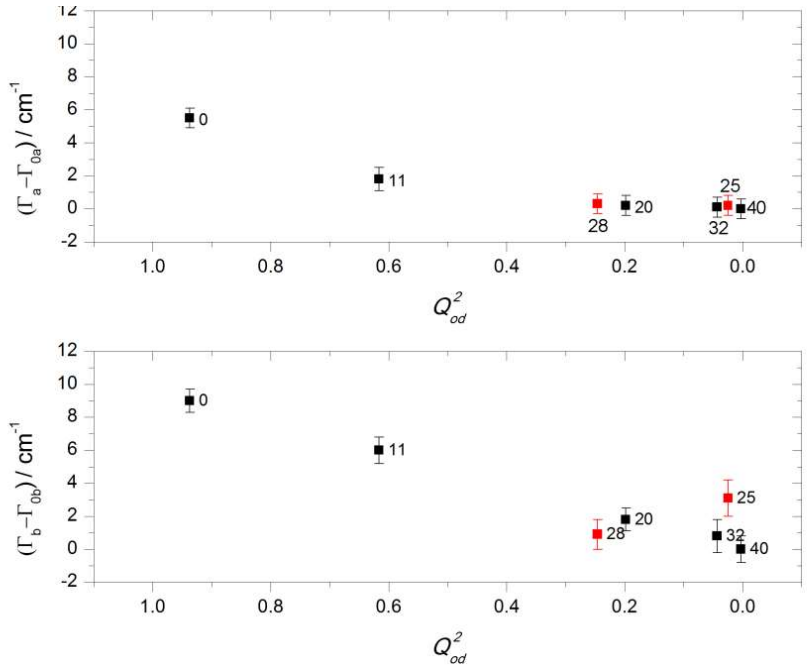

Figure 5.11: Correlation between the broadening shifts of Raman bands υ_a and υ_b, as calculated by Salje *et al.*[55], and the square of the order parameter Q_{od}. The outliers are shown in red.

In conclusion, albite Raman features (*i.e.*, peak positions and peak linewidths) are differently influenced by the Al-Si disordering process. Peak linewidths are more affected than peak positions. Raman spectroscopy is found to be a good probe for local ordering behaviour, in particular it is sensitive to the first annealing steps, when the macroscopic order parameter is still high. From Q_{od} values lower than 0.6, peak broadening attains its maximum value and it is no more affected by the Al-Si distribution.

5.4.1 An attempt to model the disordering process in Na-feldspars

To explain the increase in peak linewidth when the order parameter decreases, a simple model is tested. We know from literature that low albite follows one-step disordering path when it is heated, *i.e.* Al atoms migrate from $T_1(o)$ site to the other three sites. From the T-O bond distances, measured by SC-XRD, it is possible to estimate the Al content (see Table 5.1) in each tetrahedral site as described in Appendix C .

Table 5.1: Al content in tetrahedral sites of albite, calculated as reported in Kroll and Ribbe[82]. Asterisks indicate the outliers.

	Al content			
Annealing days	$t_{1(o)}$	$t_{1(m)}$	$t_{2(o)}$	$t_{2(m)}$
0	0.96	-0.01	0.03	-0.10
11	0.82	0.03	0.07	0.09
20	0.57	0.12	0.15	0.17
25*	0.37	0.21	0.20	0.22
28*	0.60	0.10	0.13	0.16
32	0.41	0.20	0.21	0.23
40	0.30	0.24	0.23	0.23

We would like to verify if the peak broadening could be explained by the simple superimposition of four vibrational modes, each associated to a different position of Al in the tetrahedral sites. Each Lorentzian band represents the vibrational contribution of a specific ring configuration (with Al in a specific position). The amplitude of each peak is therefore weighted by the Al distribution in the different sites. As a first attempt, we consider the four Lorentzian curves, equidistant from each other and having the same linewidth of low albite (Γ = 7 cm^{-1}). A starting value for the distance between the peaks (d = 2.5 cm^{-1}) was chosen in order to obtain a final broadening similar to the measured one.

In the simulation, the linewidth of the four bands, the distance between them, the position of the Raman band measured at 0 day (low albite) and an Al content equal in the three T_1(m), T_2(o) and T_2(m) sites are assumed as known. Given the Al content in T_1(o), the program simulates the four bands and gives the linewidth of the band sum (see the values in Table 5.2). In Figure 5.12, the measured peak linewidths of the Raman band υ_a *versus* the calculated Al content in T_1(o) site is displayed (*squares*). The theoretical curve, obtained assuming that the Raman peak υ_a is due to the convolution of four Lorentzian bands, is also drawn in Figure 5.12 (*circles*).

Table 5.2: Experimental and simulated Al content in T_1(o) and linewidths of the Raman band at 507 cm^{-1}.

Experimental		Simulation	
t_{1o}	Γ_{507} (cm^{-1})	t_{1o}	Γ_{507} (cm^{-1})
0.95	6.9	1	7.0
0.82	10.6	0.80	8.1
0.57	12.2	0.60	10.6
0.41	12.3	0.40	12.2
0.3	12.4	0.25	12.0

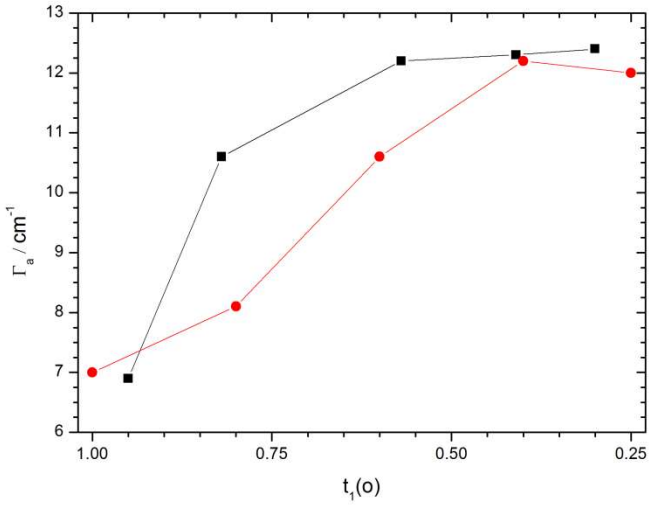

Figure 5.12: Experimental (*black squares*) and simulated (*red circles*) linewidths of the Raman band υ_a *versus* the Al content in the tetrahedral site T_1(o). Lines are guide to the eye.

The results show that the proposed model does not mimic very well the measured trend. Even changing the starting parameters, the simulated curve has a different behaviour than the experimental one. In particular, the model shows a greater broadening rate in the last part of the disordering, while in the experimental data, a value of the broadening near to the maximum was reached in the earliest stage of the process. That means that the vibrational behaviour of the low albite in the high-temperature disordering process is more complex than the one hypothesised in the model. A possible explanation of the immediate broadening could be related to the loss of the translational order. During heat treatment there is a successive loss of order due to the migration of the Al atoms from the T_1(o) site (low albite structure) to the other sites (high albite structure). This leads to the loss of the translational order and, hence, of the Raman selection rules. The vibrational behaviour of the disordered crystal cannot anymore be simply described at $\mathbf{\Gamma} = 0$, but we have to consider the phonon density of the states with $\mathbf{\Gamma} \neq 0$, involving a frequency range around the one at $\Gamma = 0$. This phenomenon, producing a peak broadening, is similar to what happens in nanoparticles due to the phonon confinement[86].

6. THE Ca-Na SUBSTITUTION: THE PLAGIOCLASE SOLID-SOLUTION

Feldspars and, more precisely, plagioclases are key mineral phases in planetary bodies: on Earth, feldspars are the most common rock-forming minerals of igneous, metamorphic and sedimentary rocks, plagioclases compose most of the Moon surface and they are the major constituents of basaltic rocks on Mars and in asteroids like Vesta.

In situ analysis of extra-terrestrial samples has reached overwhelming interest in recent time. Explorations using robot probed spectroscopy and X-ray diffraction are currently done in spacecraft exploration of Mars[87]. In the last decade, Raman spectra of the most important minerals and their solid solutions have been actively investigated[2,44,88–90], in order to provide models for the interpretation of the spectra from planetary exploration. A Raman spectrometer (MMRS) is actually planned for the NASA Mars 2020 mission.

The chemical composition of plagioclases is very important to understand the petrologic evolution of the parent rocks, because they are involved in several key reactions of petrologic interest, as igneous and metamorphic reactions. In this chapter we propose Raman spectroscopy as a technique suitable to gain chemical information on plagioclases. An analogous and successful study has been done for garnets[90].

The major problem in plagioclases is their mixing behaviour, which is complicated by compositional-driven phase transitions and by the Al-Si ordering. Natural Ab-rich plagioclases have average $C\bar{1}$ symmetry (some have e_2 on top of $C\bar{1}$) and display decreasing order with increasing An content. The An-rich plagioclases (from An_{50} up to An_{90}) have $I\bar{1}$ average symmetry, with increasing Al-Si order with increasing An content. The complete order with strictly alternating Al-Si is achieved only in pure anorthite.

Raman spectroscopy has been rarely used in literature to study the plagioclase solid solution. Energy dispersive spectrometry (EDS), wavelength dispersive spectrometry (WDS) or laser ablation are the most common techniques used to get information about their chemical composition, but these analyses require the preparation of the sample, are time-consuming and expensive. The most comprehensive Raman investigation on feldspars[2], after the preliminary results from Mernagh[48], led to a classification of the major structural types without a detailed study of the changes of the Raman features within the plagioclase composition. Indeed, Freeman *et al.*[2] did not show clear trends relating the position of a given Raman peak with the composition of plagioclase. In 1989, Raman spectroscopy was employed to study three synthetic diaplectic plagioclase feldspars at different shock pressures[43]. In 2005, Fritz *et al.*[47] reported on a micro-Raman spectroscopic investigation of plagioclases of different degree of shock metamorphism in Martian meteorites.

6.1 The experimental setup

We performed Raman investigation on a series of well-characterized natural plagioclases, kindly supplied by M. A. Carpenter of the Cambridge University (see Table 6.1). These samples have been previously analysed by powder-XRD[91] (P-XRD), SC-XRD at ambient condition[15] and at high-pressure[62], and recently by high-resolution P-XRD with synchrotron radiation[69,70]; transmission electron microscopy[91,92] (TEM), infrared spectroscopy[57,93] and calorimetry[91,94–96]. Sample names are given in refs[91,97].

The samples are all natural and have a chemical composition ranging from An_0 to An_{100}, with a mean orthoclase (*Or*) content less than 3 mol% and FeO content less than 0.45 wt%. Single-crystal structure refinements and TEM observations show that the samples are homogeneous low structural state plagioclases, with the highest degree of Al-Si order possible at each composition. The increasing degree of disorder away from the end-members, as measured by decreasing values of Q_{od}, is solely due to the exchange of Al and Si with changing composition.

Except for low albites, all samples were prepared from natural rocks by Carpenter *et al.*[16,91] in the following way: crushed, mechanical purified through a 76 μm sieve, separated by flotation in water and split by density. The fraction with the cleanest looking grains and the narrowest composition range was selected for the final purification by heating in air at 800 °C for 12 hours. As the last step, impurity grains were removed by handpicking under a microscope. The prepared powder has impurity content less than 1% and consists of equidimensional or slightly acicular crystals in the size range 50-200 μm. Low albite sample #7010 has been supplied by G. L. Hovis of Lafayette College, Easton, PA (USA), whereas low albite from Minas Gerais belongs to the Mineralogical Collection of the DIFEST Department (University of Parma).

Unpolarized Raman spectra were measured on loose plagioclase crystals and analysed with a 100X objective (NA = 0.9). A minimum of ten spectra was acquired for each sample at different spots, using exposure times of about 60-180 seconds, repeated 3-6 times, depending upon the crystal size, the Raman scattering efficiency and the intensity (if any) of the background fluorescence. Due to the small grain size no attempt was made to take Raman spectra from oriented single crystals and then to evidence orientation effects. The system was calibrated before each sample acquisition by measuring the main Raman mode (520.6 cm^{-1}) of silicon. Spectra were collected in the range 50-1200 cm^{-1} with a spectral resolution of 1.5 cm^{-1}. A 6^{th} degree polynomial curve was subtracted as baseline to remove fluorescence background. Peak fitting was made with LABSPEC 5.78.24 software package, Jobin Yvon/Horiba, using pseudo-Voigt profiles. Peak positions and linewidths are given by averaging data from different points of each sample. The characteristic feldspar doublet peak shows SEMs in the range 0.1 and 0.3 cm^{-1} for peak positions and between 0.1 and 0.6 cm^{-1} for peak linewidths. Larger standard deviations of mean occur for weaker bands, because of the low signal to noise ratio.

Table 6.1: Provenance, composition, structural state and degree of order of natural plagioclases used in this study.

Mean An content (mol %)	Sample name	Origin and Locality	Mean composition	Structural state	Q_{od}
1	Minas Gerais albite	Pegmatitic, Minas Gerais, Brazil	$An_1Or_2Ab_{97}$	$C\bar{1}$	1
1	Amelia albite	Pegmatitic cleavelandite, Amelia Courthouse, Virginia	$An_1Or_1Ab_{98}$	$C\bar{1}$	1
20	Hawk b	Pegmatitic, Hawk Mine, Bakersville, Mitchell County, N. Carolina	$An_{20}Or_3Ab_{77}$	e_2	-
27	97490	Pegmatitic, Head of Little Rock Creek, Mitchell County, N. Carolina	$An_{27}Or_2Ab_{71}$	e_2	0.55
35	91315c	Metamorphic, North Mine, Broken Hill, New South Wales	$An_{35}Or_1Ab_{64}$	e_2	0.35
40	T-12-22a	Metamorphic, Belleau-Desaulniera area, Quebec	$An_{40}Or_1Ab_{59}$	e_2	-
46	67783	Anorthositic granulite, Tanganyika	$An_{46}Or_2Ab_{52}$	e_1	0.33
49	91413b	Metamorphic, Stirling Hill, New South Wales	$An_{49}Or_0Ab_{51}$	e_1	-
60	11044pl	Igneous, Duluth, Minnesota	$An_{60}Or_2Ab_{38}$	e_1	-
60	67796b	Metamorphic, Gulela Hills, Tanzania	$An_{60}Or_1Ab_{39}$	e_1	0.26
65	SKHHM	Igneous, Skaergaard intrusion, Greenland	$An_{67}Or_1Ab_{32}$	e_1	-
68	Lake Co.	Volcanic, Lake County, Oregon	$An_{68}Or_1Ab_{31}$	$I\bar{1}$	0.56
71	42771b	Igneous, Bushveld complex, Transvaal	$An_{71}Or_1Ab_{28}$	e_1	-
72	Crystal Bay	Igneous, Crystal bay, Lake Superior, Minnesota	$An_{72}Or_0Ab_{28}$	$I\bar{1}$	-
78	101377a	Igneous, Silver Bay, Lake Superior, Minnesota	$An_{78}Or_0Ab_{22}$	$I\bar{1}$	0.72
86	21704a	Igneous, Vlakfontein, Bushveld complex, Transvaal	$An_{86}Or_0Ab_{14}$	$I\bar{1}$	0.85

89	87975a	Metamorphic, Sittampundi, Madras	$An_{89}Or_0Ab_{11}$	$I\bar{1}$	0.85
96	115082a	Metamorphic, S. of Blantyre Nyasaland	$An_{96}Or_0Ab_4$	$P\bar{1}$	0.88
98	Somma	Volcanic, Vesuvius, Italy	$An_{98}Or_0Ab_2$	$P\bar{1}$	0.91
99	Pasmeda	Metamorphic, Pasmeda Alp, Fassa Valley, Trentino, Italy	$An_{99.3}Or_{0.4}Ab_{0.3}$	$P\bar{1}$	0.92

6.2 Results

In plagioclases, the number of formula units per primitive cell (Z) ranges between 2 and 8 according to symmetry. The number of atoms per formula unit is 13. Hence, there are 26 atoms in low albite and albite-rich plagioclase, 52 atoms in anorthite-rich plagioclase with $I\bar{1}$ symmetry and 104 atoms in anorthite-*P*. Factor group analysis predicts:

- 39 A_g and 39 A_u modes for albite-rich plagioclases with $C\bar{1}$ structures (Z=2)
- 78 A_g and 78 A_u modes for anorthite-rich plagioclases with $I\bar{1}$ symmetry (Z=4)
- 156 A_g and 156 A_u modes for anorthite-rich plagioclases with $P\bar{1}$ structures (Z=8).

Only the A_g modes are Raman active.

Figure 6.1 shows Raman spectra collected on the 20 powdered plagioclases. After visual inspection, we observe that low albites have the best signal to noise ratios. The number of the observable Raman bands ranges from 10 to 56 according to the sample. In particular, 39 and 34 peaks have been recorded on low albite from Minas Gerais and Amelia Courthouse, respectively; ~19 Raman bands on incommensurate plagioclases with e_2 and e_1 structures; ~25 Raman bands on anorthite-rich plagioclases with $I\bar{1}$ structure and, finally, ~56 Raman peaks on anorthites. The lack of many Raman features in anorthite spectra is probably due to degeneracy and weakness of the intensity of some modes, as already pointed out[98,99].

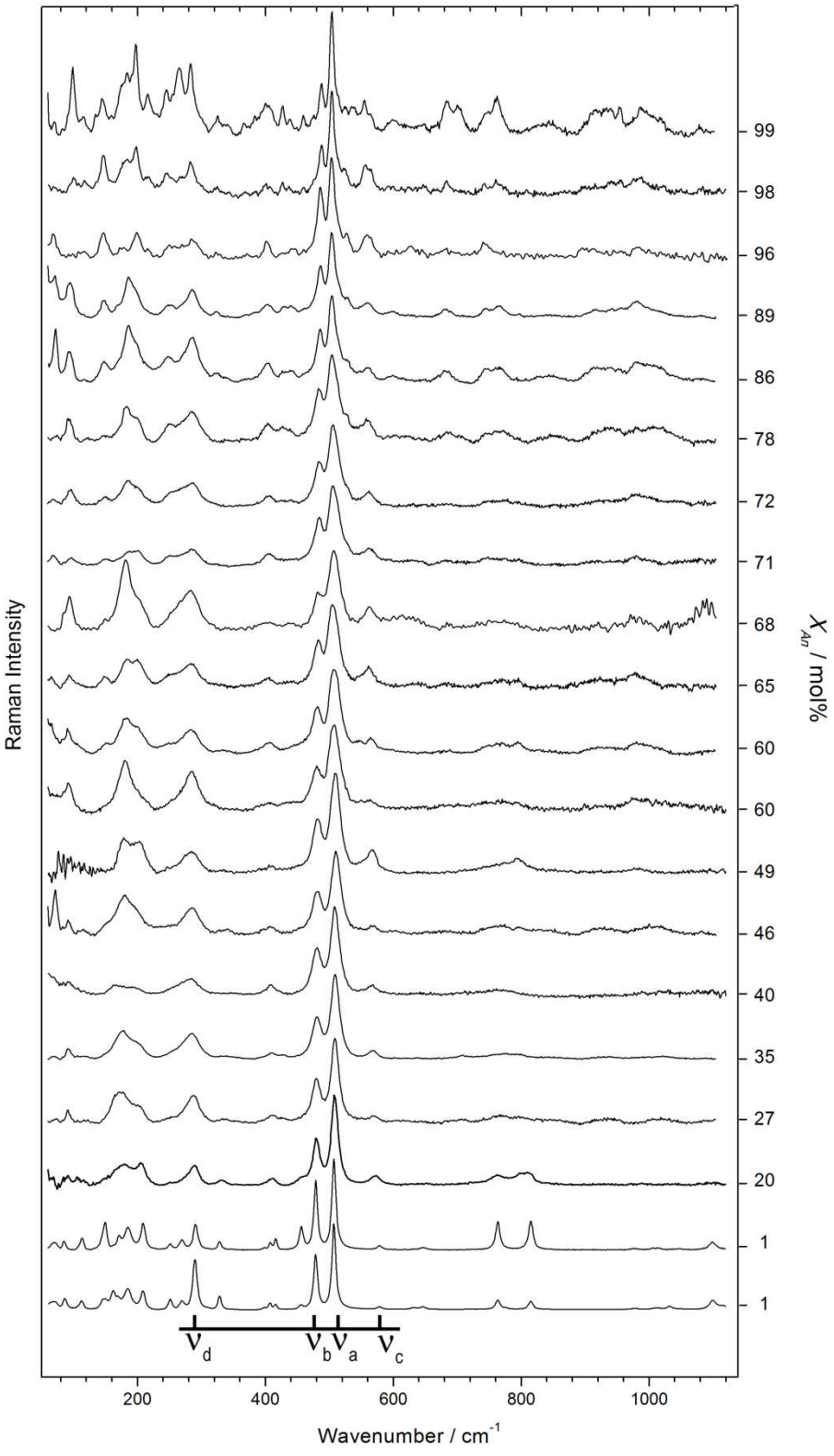

Figure 6.1: Raman spectra collected on the 20 natural plagioclases.

Differences in the intensity among the collected spectra are due to orientation effects: *e.g.*, the Raman spectra measured on the two low albites have vibrational features in the same positions, but with different relative intensities, because low albite from Minas Gerais occurs as platy crystals twinned on (010) face, whereas Amelia albite is generally crushed along the (001) cleavage surface.

Consistently with previous chapters, feldspar characteristic peaks in the range 470-510 cm^{-1} will be labelled as υ_a and υ_b; the Raman bands at 578 and 290 cm^{-1} as υ_c and υ_d, respectively. The aforementioned wavenumbers refer to low albite.

The evolution of the four Raman bands υ_a, υ_b, υ_c and υ_d, as a function of composition, is shown in Figure 6.2.

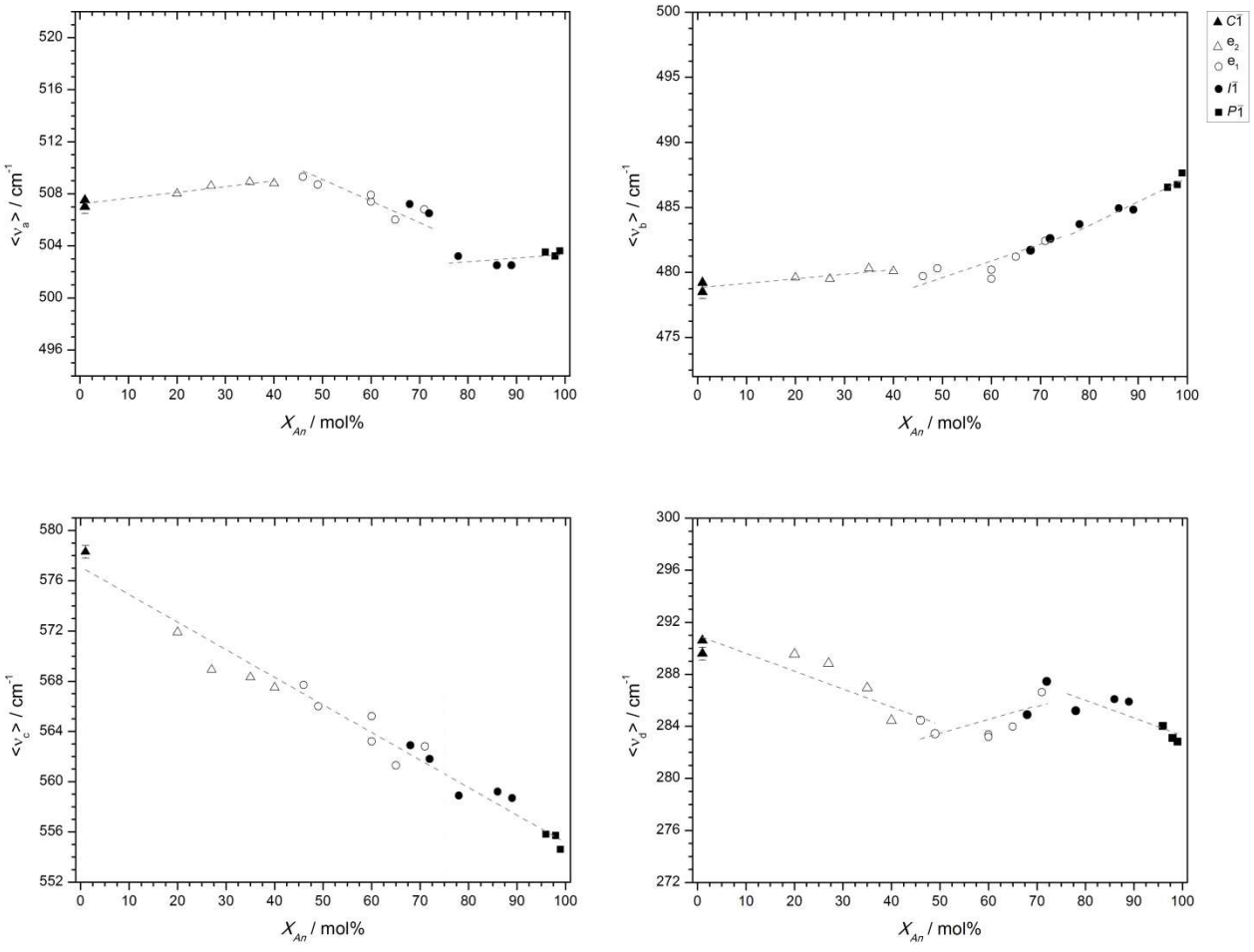

Figure 6.2: Raman shifts as a function of composition for the υ_a, υ_b, υ_c and υ_d bands. Different symbols show the different symmetries as measured by TEM[91]. The error bars are ± 0.5 cm^{-1} and are shown on the first point for each graph. The dashed lines are least square fits to the data to use only as guide for the eye.

The strongest Raman band υ_a moves with the An content, with a maximum absolute shift of 6 cm^{-1}: 507 cm^{-1} in low albite, a maximum of 510 cm^{-1} in *e* plagioclases and 504 cm^{-1} in anorthite-*P* structures. The group of anorthite-*I* can be divided into two sub-groups: structures having a vibrational patterns similar to Ab-rich plagioclases (υ_a = ~507 cm^{-1}) and those displaying Raman features resembling the anorthite characteristic bands (υ_a = ~504 cm^{-1}). This division is confirmed by the diffraction patterns: the first group gives rise to elongate *b* reflections, whereas the latter shows both sharp *b* and diffuse *c* reflections, typical of primitive unit cells.

Moving from the Na-endmember to the Ca-endmember, the Raman band υ_b up-shifts of about 9 cm^{-1} and additional Raman modes appear between 450 and 550 cm^{-1}. In low albites and e-plagioclases spectra three modes are counted (*i.e.*, 456-458, 478-480 and 507-510 cm^{-1}), whereas in more anorthitic samples with $I\bar{1}$ and $P\bar{1}$ structures there are six bands (*i.e.*, ~459, ~476, ~486, ~504, ~513 and ~524 cm^{-1}). In Figure 6.3 are compared the Raman spectra of the two end members in the range 450-530 cm^{-1}.

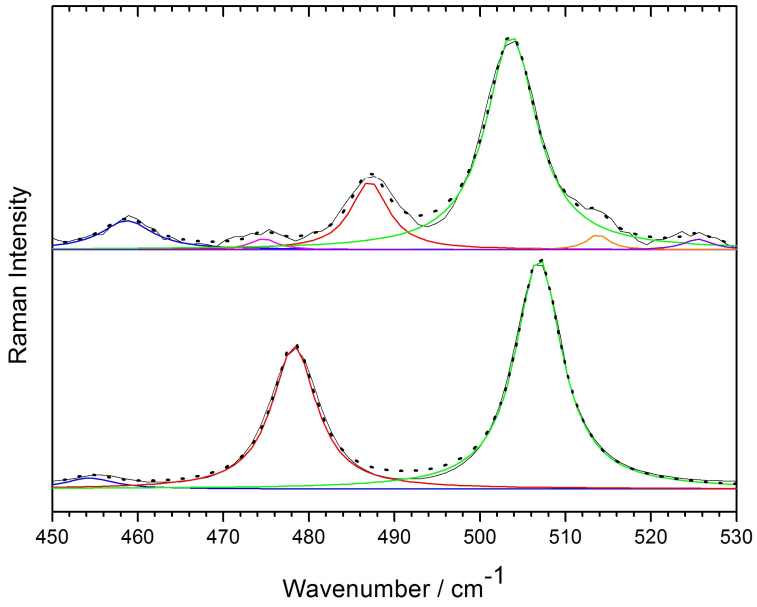

Figure 6.3: Comparison between Lorentzian profiles made on anorthite (*above*) and low albite (*below*): six and three curves are used in the peak fitting procedure, respectively.

In some spectra collected on anorthite crystals from Pasmeda Alp, an additional Raman feature appears at ~536 cm^{-1} to be ascribed to thomsonite[100] and not to anorthite. Thomsonite ($NaCa_2Al_5Si_5O_{20}\cdot 6H_2O$) belongs to the "fibrous zeolite" group[68]. Anorthite crystals can be replaced by thomsonite due to alteration processes. The backscattered electron images (BES), taken on a cross section of some Pasmeda anorthite crystals have confirmed the presence of two different chemical compositions and showed a blotched appearance of crystals, typical of extensive replacement by thomsonite. Raman spectra collected on the two different areas of the crystals display different vibrational features (see Figure 6.4).

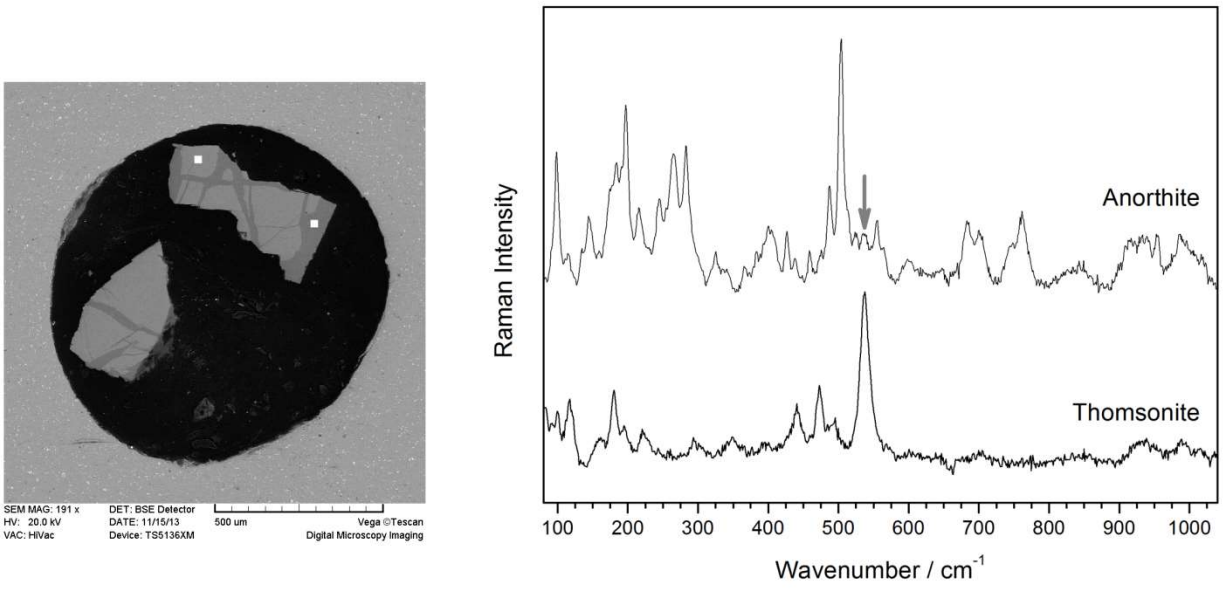

Figure 6.4: Backscattered electron image of anorthite crystals from Val Pasmeda sample, embedded in resin, revealing a blotched appearance due to the replacement by thomsonite (*left*); Raman spectra collected on the light grey area (anorthite) and on the dark grey one (thomsonite) (*right*).

Raman band υ_c down-shifts with increasing An content and shows the highest variation (24 cm^{-1}): its weak intensity, mainly in the anorthitic samples, prevents the identification of a reliable trend along the solid solution.

The position of the Raman band υ_d changes of about 7 cm^{-1} between the two end members (290 cm^{-1} in low albite and 283 cm^{-1} in anorthite). Within the plagioclase samples it fluctuates

around 287 cm^{-1} and three approximate trends can be suggested. Its position is probably also influenced by the contribution of near weak bands. In anorthitic samples with $I\bar{1}$ and $P\bar{1}$ symmetries, any peak fitting procedure is unreliable due to the large number of modes with unknown wavenumber.

For these reasons, both Raman bands υ_c and υ_d will not be used in the following discussion.

As regards the spectral region at higher wavenumbers, the peak number changes between the two end members. According to Freeman *et al.*[2], the number of the observable features in the 900-1200 cm^{-1} spectral range reflects the variation in Al-Si distribution, induced by varying proportions of Ca and Na in the structures (*i.e.*, 1:3 in Na-feldspar and 2:2 in Ca-feldspar). The increase in the number of anorthite Raman bands is consistent with increased contributions of the Al–O–Al and Al–O–Si bonds to the vibrations. Moreover, the lowering in symmetry from $C\bar{1}$ to $I\bar{1}$ and from $I\bar{1}$ to $P\bar{1}$, when moving away from Na-endmember, leads to an increase in the expected Raman modes because the population of the unit-cell changes from 2 to 8 formula units. Unfortunately, these features are very weak and they could not be reliably resolved in our anorthitic samples. Anyhow, five modes at about 914, 931, 941, 954 and 988 cm^{-1} have been fitted in the anorthite Raman spectra, whereas a single mode at 978 cm^{-1} is observed in low albite.

In Figure 6.5, the evolution of all the Raman bands used in the peak fitting procedure is displayed. The very weak features between 600 and 750 cm^{-1} and above 1000 cm^{-1} are not shown.

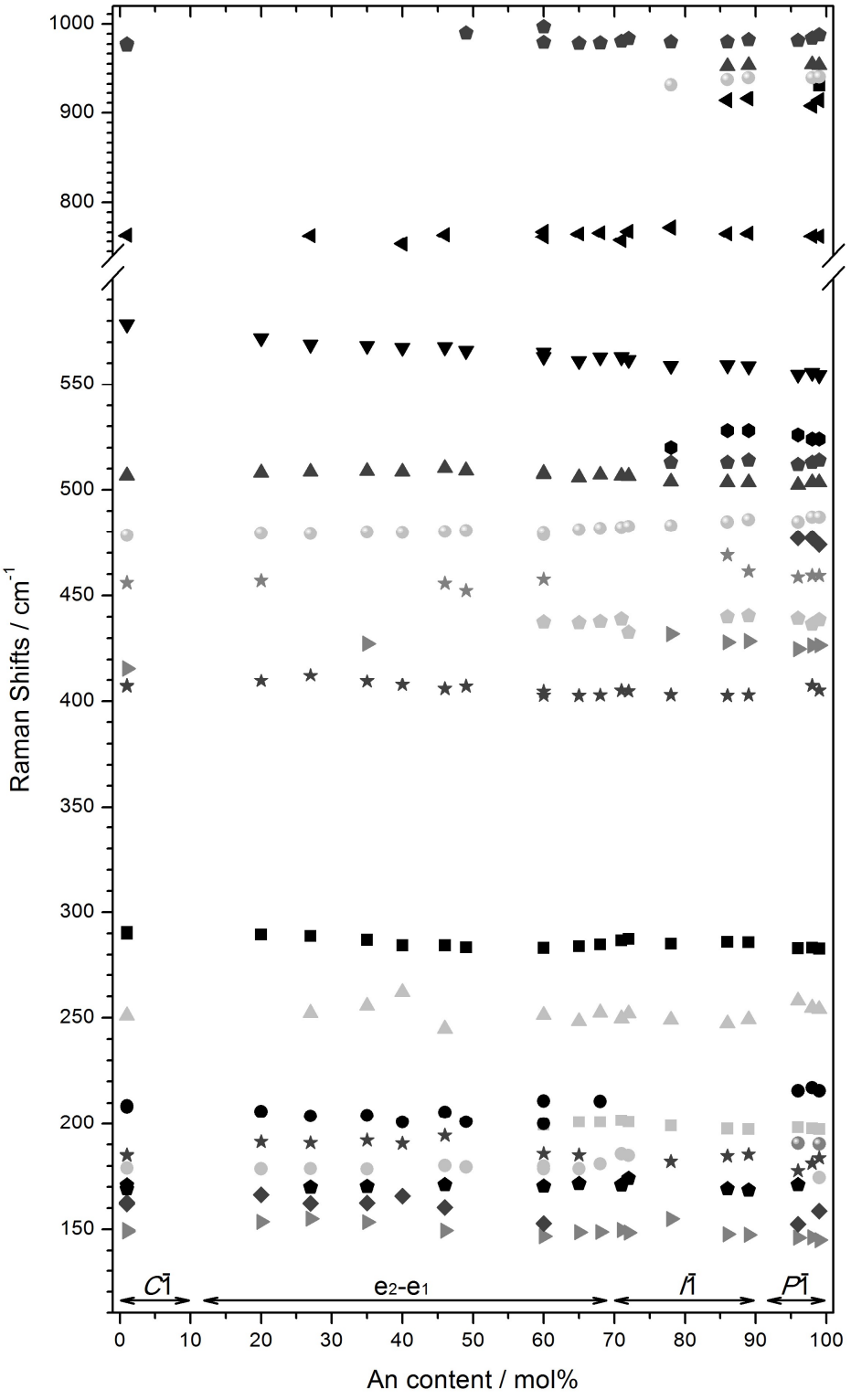

Figure 6.5: Shifts of the Raman bands along the solid solution. The different symmetry regions are indicated near the horizontal scale.

Peak linewidths increase moving away from the two end members (see Figure 6.6), as expected, because the order parameters Q_{od} decrease within the solid solution with respect to the end members (Figure 6.7). Low albite and anorthite, showing the fully ordered Al-Si configuration, display the narrowest bands. The highest disorder (*i.e.*, Q_{od} = 0.26) is measured for sample #67796b (An_{60}).

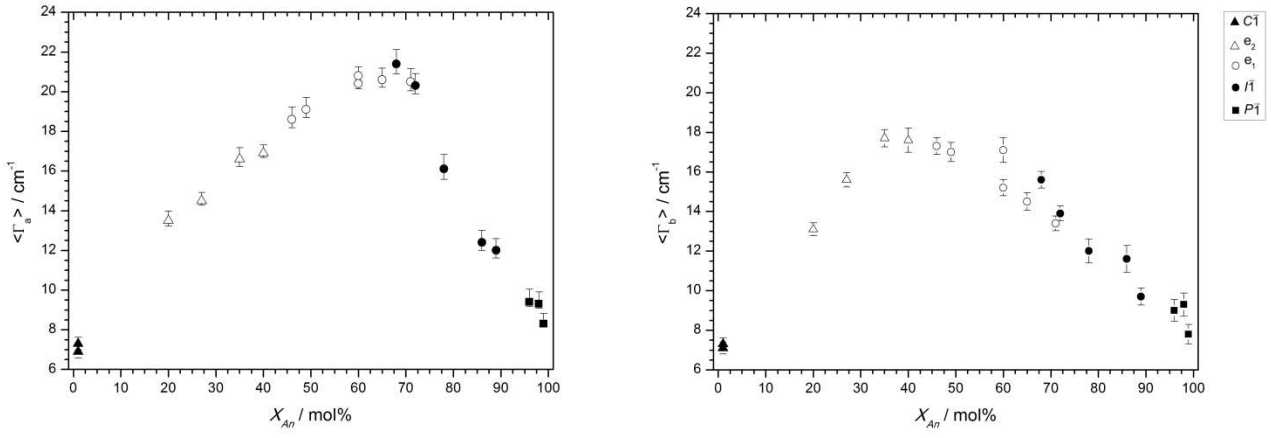

Figure 6.6: Average linewidths of the Raman peaks υ_a and υ_b within the solid solution. Different symbols show the different symmetries as measured by TEM.

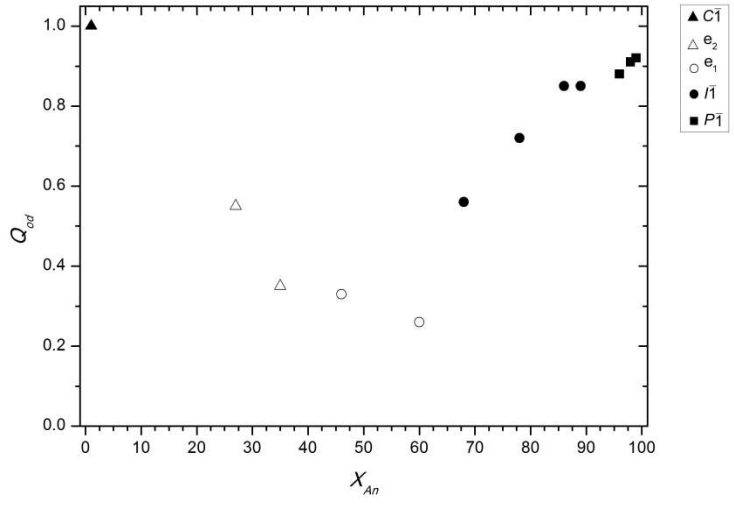

Figure 6.7: Values of Q_{od} calculated by X-ray data (from refs[15,69]) as a function of the An content.

6.3 Discussion

In general, the number of the observed Raman bands in each spectrum gives information about the unit-cell symmetry: moving away from the $C\bar{1}$ structures, the peak number increases as expected by factor group analysis. The peak positions shift with changing An content and new bands appear (Figure 6.5). In particular, the average difference in wavenumber between Raman band υ_a and υ_b is found to be diagnostic to discriminate among plagioclase symmetries. The average difference measured in plagioclases is 28.4 cm^{-1} in low albites, 29.0 cm^{-1} for e-plagioclases, 21.4 cm^{-1} in the $I\bar{1}$ plagioclases and 17.0 cm^{-1} in anorthites (see Table 6.2). This difference has been already employed by Freeman *et al.*[2] to discriminate among the three natural feldspar endmembers.

Table 6.2: Average wavenumber differences between Raman bands υ_a and υ_b in the different plagioclase structures.

	Low albite	e-plagioclase	$I\bar{1}$ plagioclase	Anorthite
υ_a-υ_b (cm^{-1})	28.4	29.0	21.4	17.0

Interesting trends with the An content can be suggested for all the four investigated bands: we focus on the behaviour of the strongest Raman peaks in the range 470-510 cm^{-1} with the aim to determine the Na/Ca ratio in plagioclase minerals.

We know[2,4,101] that changes in extra-framework cations have a moderate influence on the positions of Raman bands ν_a and ν_b, because the interactions between the M cations and the oxygen atoms are weaker than the M–O interactions in other minerals, such as olivine and pyroxene. The maximum Raman shifts are 6 cm^{-1} for υ_a and 9 cm^{-1} for υ_b. Moreover, it is well known that the position of Raman band υ_a shows an inverse correlation with the size of the tetrahedral ring[101]: *e.g.*, quartz (SiO_2) has a six-membered ring and its strongest Raman peak occurs at 464 cm^{-1}; spodumene-II ($LiAlSi_2O_6$) has a five-membered ring subunit and its strongest Raman peak is at 492 cm^{-1}, feldspars, with a four-membered ring, show the strongest Raman peak to be near 510 cm^{-1}.

From a more careful inspection of Raman band υ_a, we observed that between An_{72} and An_{78} the feature centred at ~508 cm^{-1} (average value between plagioclases with $C\bar{1}$ symmetry) shifts to lower wavenumbers and becomes a triplet (centred at ~504 cm^{-1}, with shoulders at ~513 and ~524 cm^{-1}). This change occurs when *c* reflections arise in the diffraction patterns (*i.e.*, from sample An_{78} onwards) and corresponds to the modification from an "albite-like" Raman spectrum to a more "anorthite-like" spectrum (see Figure 6.1).

In Figure 6.2, both the evolutions of Raman bands υ_a and υ_b as a function of the An content display two changes in slope at ~An_{45} and ~An_{75}. The first one occurs between e_2 and e_1 plagioclases, the second separates e_1 and $I\bar{1}$ species with only b reflections in their diffraction patterns from $I\bar{1}$ and $P\bar{1}$ plagioclases having b and c reflections, too. The first discontinuity represents exactly the $e_2 \rightarrow e_1$ phase transition, whereas the second one corresponds to a good approximation to the $C\bar{1} \rightarrow I\bar{1}$ transition, which has been determined at ~An_{70} by previous analyses[57,91]. The $I\bar{1} \rightarrow P\bar{1}$ phase transition in the anorthite-rich side of the solid solution has not been detected.

Variations in peak broadening provide insights into the behaviour of the order parameter on a local scale, as already observed for the low albite-high albite thermal crossover (see Chapter 5). Moving inside the solid solution, peak linewidths (Figure 6.6) and the disorder (Figure 6.7) increase, as the structures have to incorporate more Al atoms to balance the change from monovalent to divalent cations. If we plot the peak linewidth Γ_a as a function of the order parameter Q_{od}, and we look at the anorthite-rich side, the presence of the $I\bar{1} \rightarrow P\bar{1}$ transition is clearly seen (Figure 6.8).

Similar trends have been found by Atkinson *et al.*[57]: they performed on the same samples infrared analyses. Changes in wavenumber and linewidth with composition and degree of order have been evidenced at ~An_{45}, ~An_{70} and ~An_{90}, but the variation from "albite-like" to more "anorthite-like" infrared spectrum was observed at lower anorthite content than in Raman spectra: the change occurs between An_{40} and An_{49}, *i.e.* between e_2 and e_1 structures.

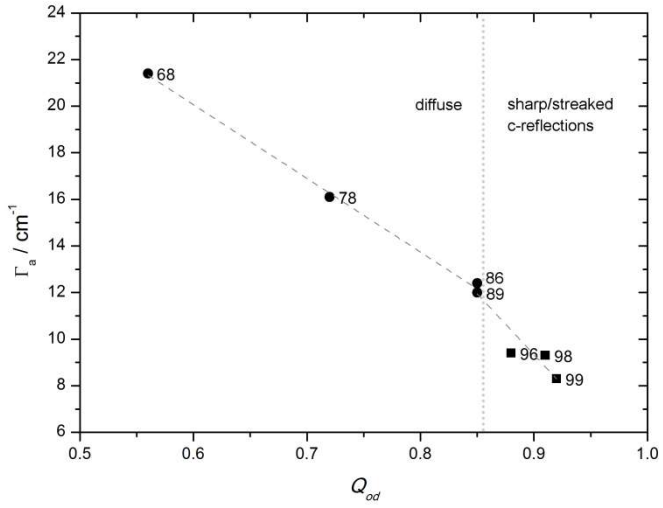

Figure 6.8: Correlation of the peak linewidth Γ_a with the order parameter Q_{od} in the anorthite-rich side of the solid solution. The dashed lines are both least square fits to the data, for $I\bar{1}$ structures and then for $P\bar{1}$ structures. The dotted line shows the boundary between samples with diffuse c reflections in their diffraction patterns and those with sharp and streaked c reflections.

In Figure 6.9 is shown the correlation between the x_6 component of the spontaneous strain tensor ($\sim cos\gamma$) and Raman band υ_a: a linear fit extrapolates the e_2 data through the points of low albite and an equivalent fit is used for e_1 data and anorthite-rich samples. The discontinuity is set between ~A_{40} and ~An_{50}. This confirms the infrared data.

Unlike infrared spectra, where the e_2 ordering scheme seems to be related to the $C\bar{1}$ albite structure and e_1 to the anorthite-*I* structure, Raman features for both incommensurate types are more similar to those observed in low albite than in anorthite. Moreover, the Raman spectra collected on An_{68} and An_{72} samples show vibrational patterns more similar to those of incommensurate phases (*i.e.*, An_{46}-An_{71}) than the $I\bar{1}$ structures (*i.e.*, An_{78}-An_{89}), even though previous TEM analyses indicated $I\bar{1}$ symmetry for both samples[91]. The answer may be in the length scales probed by the two techniques and in the b domain sizes. Indeed, the microstructures described in An_{68} and An_{72} samples are on a scale ranging from 0.1 up to few μm[91].

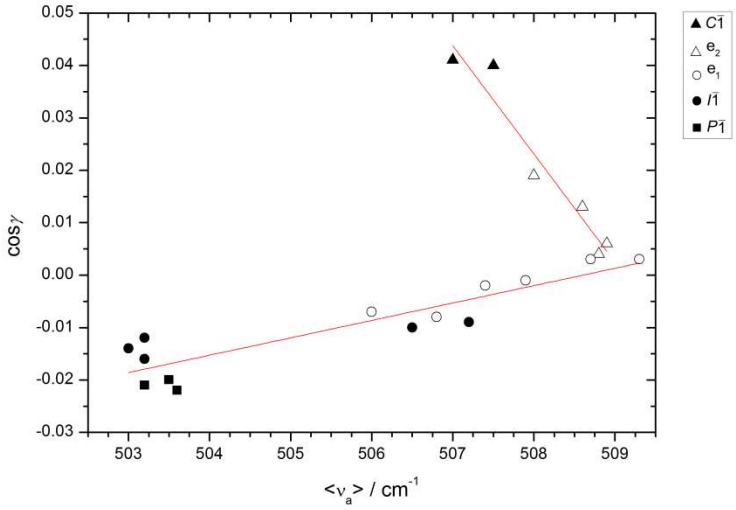

Figure 6.9: Correlation between the macroscopic strain component cosγ (~ x_6)[70,91] and the wavenumber of the Raman band υ_a. Red lines are least square fits to data to use as guide to the eye.

6.3.1 The determination of the Na/Ca ratio from the plagioclase Raman spectrum

From the Raman spectroscopic investigation of the 20 low structural plagioclases and the correlations found in the previous paragraph, we can provide a tool for the determination of the chemical composition directly from the plagioclase Raman features. Two calibration curves may be proposed between the peak broadening of the most intense Raman bands and the An content: the first curve is used to estimate the An content in albite-rich plagioclases, the second one is suitable for the anorthite-rich plagioclases (Figure 6.10). In order to provide a method independent from the experimental Raman setup, we used the intrinsic peak linewidth, instead of the measured one, correcting for the instrumental broadening (Γ_s), estimated (by calibration with a spectroscopic Ar lamp) to be 1.7 cm^{-1}. The intrinsic linewidth can be calculated as:

$$\Gamma_i = \sqrt{\Gamma_m{}^2 - \Gamma_s{}^2},$$

where Γ_m and Γ_s are the measured and instrumental linewidths, respectively.

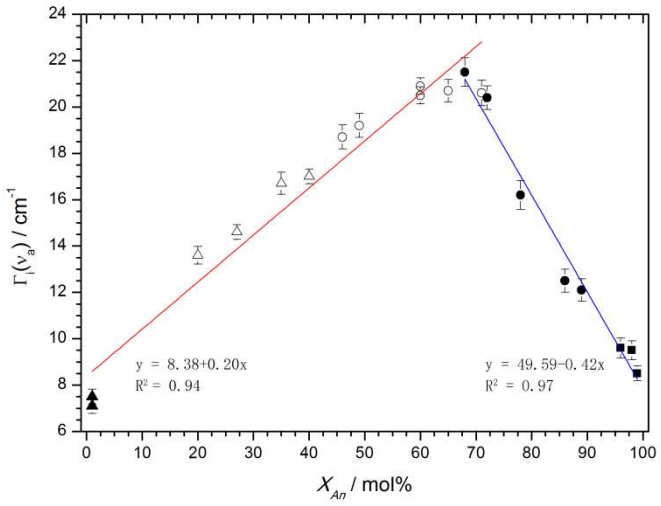

Figure 6.10: Average intrinsic linewidth of the most intense Raman peak in feldspars as a function of the An content. Red and blue lines are least square fits to the data (R^2 = 0.94 and 0.97).

The protocol we suggest is composed of two steps: first, we measure the wavenumber difference between Raman bands υ_a and υ_b to roughly establish the symmetry of the investigated mineral. If the difference is between 27 and 30 cm^{-1}, we deal with a plagioclase having $C\bar{1}$ structure, if it is below 26 cm^{-1}, the studied sample has $I\bar{1}$ or $P\bar{1}$ symmetry (Figure 6.11).

In 2008, Freeman *et al.*[2] suggested the wavenumber difference between υ_a and υ_b as diagnostic feature among feldspar compositions, but they stated that, unlike olivine, pyroxene and some Fe-oxides, the Raman peak positions of feldspars cannot be used to extract quantitative information about cation proportions. Indeed, this difference is diagnostic only for anorthite-rich plagioclases, because in albite-rich plagioclases it is essentially constant (Figure 6.11, Table 6.2). In order to obtain compositional information for Na-plagioclases too, we need to plot υ_a and υ_b differences *versus* the linewidth of the most intense Raman mode, as shown in Figure 6.12.

In the second step, we estimate the An content of the unknown plagioclase from the two calibration equations obtained by fitting the linewidths of the Raman band ν_a. We point out that the relationship between composition and linewidth can be obtained only for low structural plagioclases with a degree of order not far away from our references. For minerals showing $C\bar{1}$ symmetry, the equation of the first calibration curve (*red curve* in Figure 6.10) will be used:

$$y = 8.38 + 0.20x,$$

whereas for minerals having lower symmetries, the equation of the second calibration curve (*blue curve* in Figure 6.10) will be employed:

$$y = 49.59 - 0.42x.$$

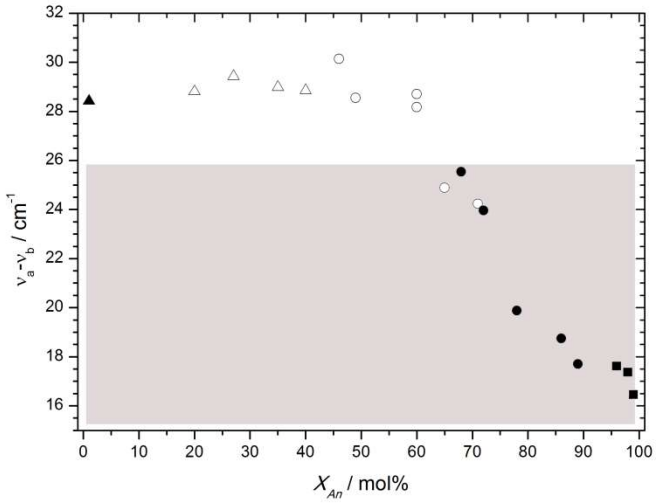

Figure 6.11: Wavenumber differences between the Raman bands υ_a and υ_b as a function of the An content. The grey area marks the $\boldsymbol{I\bar{1}}$ and $\boldsymbol{P\bar{1}}$ regions from the $\boldsymbol{C\bar{1}}$ one.

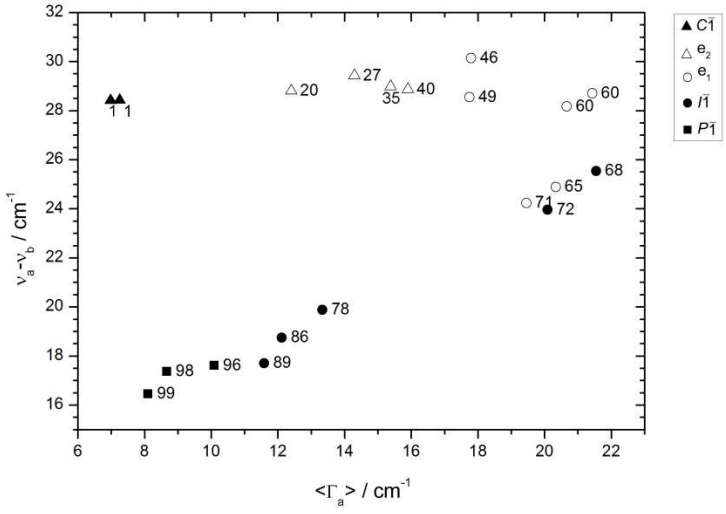

Figure 6.12: Correlation of the wavenumber differences between the Raman bands υ_a and υ_b with the average peak linewidth Γ_a.

A major problem in handling with plagioclase behaviour is that a careful analysis of the degree of order, microstructures, phase transitions and composition has to be undertaken. Until now, different analytical techniques have to be employed to get both structural and chemical information on plagioclase samples. Raman spectroscopy is found to be a suitable technique to provide a preliminary investigation on composition, symmetry, order and, if present, microstructures.

The proposed tool has been tested on three different mineralogical samples: two thin section of meteorites containing anorthitic plagioclases, supplied by M. Tribaudino (DIFEST Department, University of Parma), and a thin section from the Marsili Vulcan, kindly supplied by T. Trua (DIFEST Department, University of Parma).

Extra-terrestrial samples come from the Juvinas eucrite, an achondritic stony meteorite, fallen on 15 June 1821 in Ardèche, France, and from the Renazzo meteorite, a carbonaceous chondrite fallen on 5 January 1824, near Cento (FE), Italy. In the first one, pyroxenes, as augite and pigeonite, quartz and Fe-bearing minerals, such as troilite, ilmenite and chromite, have been found by Raman spectroscopy together with plagioclase crystals. In the Renazzo meteorite, Raman analysis was focused on the Ca, Al inclusion (CAI): spinel, melilite, fassaite, calcite, sodalite together with plagioclase have been identified. Plagioclase Raman spectra collected on both thin sections displayed vibrational patterns typical of anorthite-rich plagioclase, with the main peak showing a triplet shape (see Figure 6.13). The average difference between υ_a and υ_b was 19 and 17 cm^{-1}, respectively. The estimated average An contents were 90.5 for Juvinas meteorite and 92.7 mol% for Renazzo meteorite, in good agreement with the compositions reported in literature[102,103].

Raman spectra collected on the thin section from Marsili Vulcan (Figure 6.14.) show different vibrational patterns according to the points of analysis within the same plagioclase crystal. Laser ablation analysis performed on this sample showed that plagioclase crystals within the section have inter- and intra-crystalline heterogeneous composition varying from Ab-rich plagioclases with an An content ranging from 32 to 55 mol% and An-rich plagioclases with 78-90 An mol%. The An contents estimated by the Raman analyses show good agreement with those measured by laser ablation, with a maximum error of ±10 mol%.

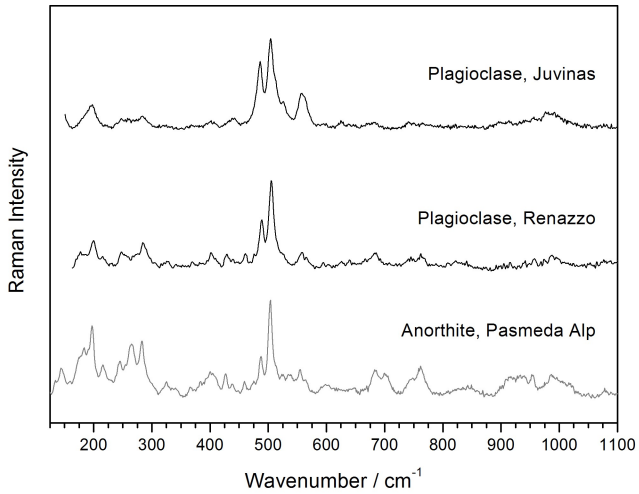

Figure 6.13: Comparison between the Raman spectra collected on thin sections of Juvinas and Renazzo meteorites and the Raman spectrum of anorthite from Val Pasmeda.

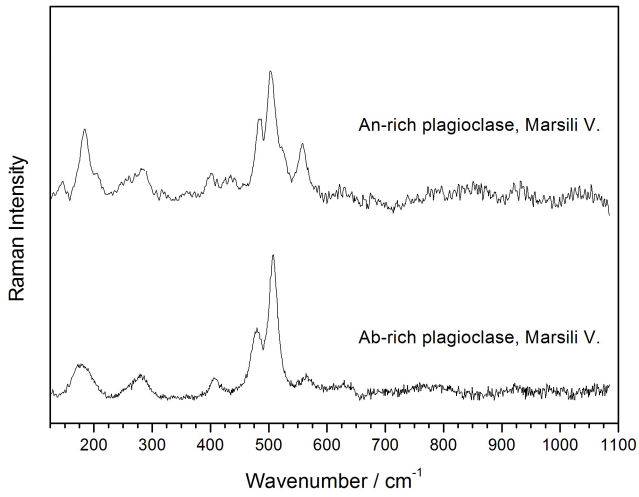

Figure 6.14: Raman spectra collected on the thin section of Marsili Vulcan sample.

In order to illustrate the investigated chemical compositions, the measured wavenumber differences and linewidths found in our samples have been plotted together with our plagioclases

references in Figure 6.15. Chemical analysis results by Raman spectroscopy are compared with those obtained by elemental techniques in Figure 6.16.

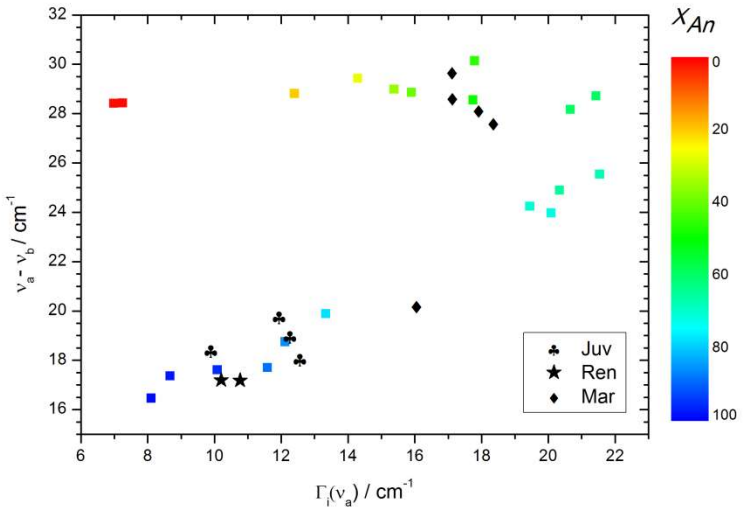

Figure 6.15: Wavenumber differences υ_a - υ_b *versus* the intrinsic linewidth of Raman band υ_a of plagioclases crystals from Juvinas meteorite (♣), Renazzo meteorite (★) and Marsili Vulcan (♦), having unknown compositions. The composition of the 20 references is shown as colour map.

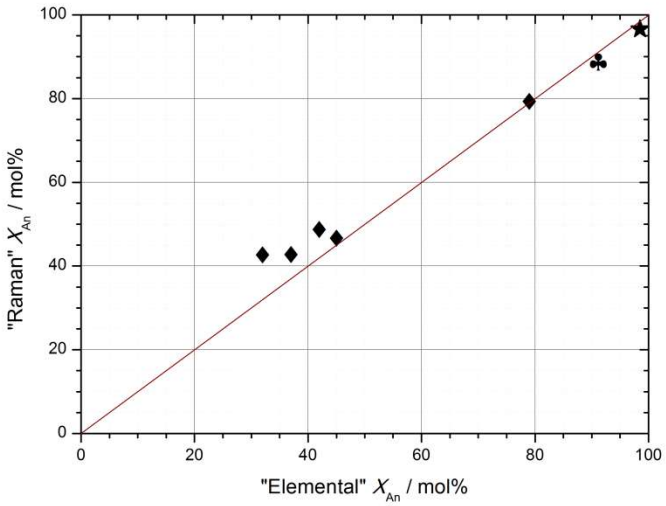

Figure 6.16: Comparison between the An contents estimated by Raman analysis and those measured by elemental techniques.

7. CONCLUDING REMARKS

The present study gives a contribution to the knowledge on the Na-feldspar and plagioclases, extending the database of the Raman spectra of plagioclases with different chemical compositions and structural orders. This information may be used for the future planetary explorations by "rovers", for the investigation of ceramics nanocrystal materials and for the mineralogical phase identification in sediments.

Na-feldspar and plagioclase solid solution have been investigated by Raman spectroscopy in order to determine the relationships between the vibrational changes and the plagioclase crystal chemistry and structure. We focused on the Raman micro-spectroscopy technique, being a non-destructive method, suited for contactless analysis with high spatial resolution. Chemical and structural analyses have been performed on natural samples to test the usefulness of Raman spectroscopy as a tool in the study of the pressure-induced structural deformations, the disordering processes due to change in the Al-Si distribution in the tetrahedral sites and, finally, in the determination of the anorthitic content (An_x) in plagioclase minerals.

All the predicted 39 A_g Raman active modes have been identified and assigned to specific patterns of atomic vibrational motion. A detailed comparison between experimental and computed Raman spectra has been performed and previous assignments have been revised, solving some discrepancies reported in recent literature. The *ab initio* calculation at the hybrid HF/DFT level with

the WC1LYP Hamiltonian has proven to give excellent agreement between calculated and experimentally measured Raman wavenumbers and intensities in triclinic minerals. A short digression on the 36 infrared active modes of Na-feldspar has been done too. The identification of all 39 computed Raman modes in the experimentally measured spectra of the fully ordered Na-feldspar, known as *low albite*, along with the detailed description of each vibrational mode, has been essential to extend the comparative analysis to the high pressure and high temperature structural forms of albite, which reflect the physical–chemical conditions of the hosting rocks.

The understanding of feldspar structure response to pressure and temperature is crucial in order to constrain crustal behaviour. The compressional behaviour of the Na-feldspar has been investigated for the first time by Raman spectroscopy. The absence of phase transitions and the occurrence of two secondary compression mechanisms acting at different pressures have been confirmed. Moreover, Raman data suggest that the internal structural changes are confined to a small pressure interval, localized around 6 GPa, not spread out from 4 to 8 GPa as suggested by previous X-rays studies on elasticity. The dominant compression mechanisms act *via* tetrahedral tilting, while the T-O bond lengths remain nearly constant at moderate compressional regimes. At the spectroscopic level, this leads to the strong pressure dependencies of T-O-T bending modes, as found for the four modes at 478, 508, 578 and 815 cm^{-1}.

The Al-Si distribution in the tetrahedral sites affects also the Raman spectrum of Na-feldspar. In particular, peak broadening is more sensitive than peak position to changes in the degree of order. Raman spectroscopy is found to be a good probe for local ordering, in particular being sensitive to the first annealing steps, when the macroscopic order parameter is still high. Even though Raman data are scattered and there are outliers in the estimated values of the degree of order, the average peak linewidths of the Na-feldspar characteristic doublet band, labelled here as υ_a and υ_b, as a function of the order parameter Q_{od} show interesting trends: both peak linewidths linearly increase until saturation. From Q_{od} values lower than 0.6, peak broadening is no more affected by the Al-Si distribution. Moreover, the disordering process is found to be heterogeneous. SC-XRD and Raman data have suggested an inter-crystalline inhomogeneity of the samples, *i.e.*, the presence of regions with different defect density on the micrometric scale.

Finally, the influence of Ca-Na substitution in the plagioclase Raman spectra has been investigated. Raman spectra have been collected on a series of well characterized natural, low structural plagioclases. The variations of the Raman modes as a function of the chemical

composition and the structural order have been determined. The number of the observed Raman bands at each composition gives information about the unit-cell symmetry: moving away from the $C\bar{1}$ structures, the number of the Raman bands enhances, as the number of formula units in the unit cell increases. The modification from an "albite-like" Raman spectrum to a more "anorthite-like" spectrum occurs from sample An_{78} onwards, which coincides with the appearance of *c* reflections in the diffraction patterns of the samples. The evolution of the Raman bands υ_a and υ_b displays two changes in slope at ~An_{45} and ~An_{75}: the first one occurs between e_2 and e_1 plagioclases, the latter separates e_1 and $I\bar{1}$ plagioclases with only *b* reflections in their diffraction patterns from $I\bar{1}$ and $P\bar{1}$ samples having *b* and *c* reflections too. The first variation represents exactly the $e_2 \rightarrow e_1$ phase transitions, whereas the second one corresponds in good approximation to the $C\bar{1} \rightarrow I\bar{1}$ transition, which has been determined at ~An_{70} by previous works. The $I\bar{1} \rightarrow P\bar{1}$ phase transition in the anorthite-rich side of the solid solution is not highlighted in the collected Raman spectra. Variations in peak broadening provide insights into the behaviour of the order parameter on a local scale, suggesting an increase in the structural disorder within the solid solution, as the structures have to incorporate more Al atoms to balance the change from monovalent to divalent cations.

All the information acquired on these natural plagioclases has been used to produce a protocol able to give a preliminary estimation of the chemical composition of an unknown plagioclase from its Raman spectrum. Two calibration curves, one for albite-rich plagioclases and the other one for the anorthite-rich plagioclases, have been proposed by relating the peak linewidth of the most intense Raman band υ_a and the An content. It has been pointed out that the dependence of the composition from the linewidth can be obtained only for low structural plagioclases with a degree of order not far away from the references. The proposed tool has been tested on three mineralogical samples, two of meteoric origin and one of volcanic origin. Chemical compositions by Raman spectroscopy compare well, within an error of about 10%, with those obtained by elemental techniques. Further analyses on plagioclases with unknown composition will be necessary to validate the suggested method and introduce it as routine tool for the determination of the chemical composition from Raman data in planetary missions.

APPENDICES

Appendix A

Chemical analysis

Chemical analyses have been performed by a TESCAN VEGA TS 5136XM scanning electron microscope at the Earth and Environmental Sciences Department, University of Milano-Bicocca. Measurements have been executed by P. Gentile (DISAT Department, University of Milano-Bicocca). The microscope is equipped with a YAG Crystal detector for secondary electrons (SE), a YAG Crystal detector for backscattered electrons (BSE), a LVSTD secondary electrons detector for low vacuum operations, an electron beam induced current detection (EBIC) and a sample current meter. The microscope employs a tungsten heated filament as electron source, with an accelerating voltage between 0.3 and 30 kV and a probe current from 1 pA to 2 μA. The maximum resolution at high vacuum is lower than 3.5 nm (at 30 kV and SEI detector), whereas the resolution at low vacuum at 150 pA is lower than 5 nm (at 30 kV and BSE detector). The magnifications range between X2 and X2000000. The sample chamber (300 x 250 mm large, 280 mm height) has a 3-axis motorized stage (360° continuous rotation and -10° to 75° tilt).

An EDAX GENESIS 4000 XMS Imaging 60 SEM is used for microanalyses.

The measurement conditions used for the analyses are: accelerating voltage 20 kV, current 190 ± 1 pA, working distance 200 nm, spot size ~ 228 nm and accumulation time 100 s. The references minerals (ASTIMEX, Toronto) used for the quantitative elemental analysis are:

- an albite crystal from Strickland Quarry, Haddam, CT, USA (wt.% SiO_2 = 68.52, Al_2O_3 = 19.54, CaO = 0.13, Na_2O = 11.59 and K_2O = 0.22),
- a plagioclase crystal with an anorthitic content of 65 mol% from Sonora, Mexico (wt.% SiO_2 = 54.23, Al_2O_3 = 28.54, CaO = 11.80, Na_2O = 4.35, K_2O = 0.41, MgO = 0.13, BaO = 0.01, TiO_2 = 0.07, FeO = 0.37 and SrO = 0.08),
- a sanidine crystal from Hohenfels, Germany (wt.% SiO_2 = 64.79, Al_2O_3 = 18.79, Na_2O = 3.02, K_2O = 12.13, BaO = 1.09 and FeO = 0.18).

The sample was prepared by handpicking some crystals in the sample holder (Figure A. 1) and covering them with some resin drops (Araldite DBF by HUNTSMAN). The surface was then polished and graphitized.

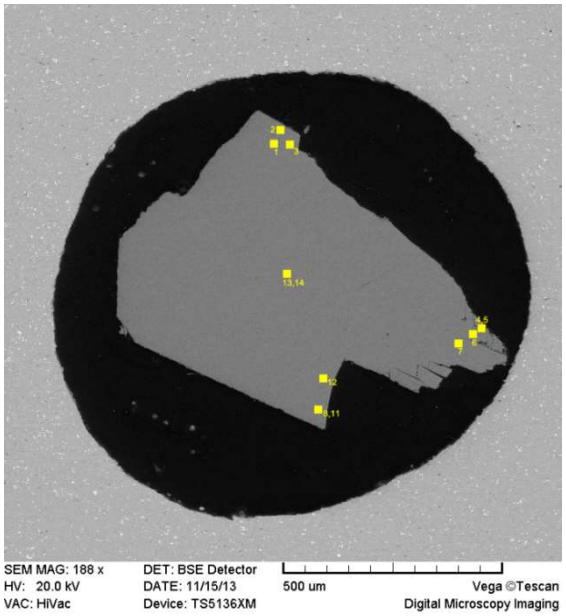

Figure A. 1: Backscattered electron image of the sample showing the points of measurement.

In the following tables, the chemical data are reported. Analyses of point 8 and 11 have been rejected because they close too low (<98%).

Table A. 1: The chemical analysis after the correction on the reference materials.

Oxide (wt.%)	1	2	3	4	5	6	7	12	13	14	Avg.	2σ
SiO_2	67.88	68.40	68.31	67.27	67.45	68.27	67.37	67.64	68.20	68.03	67.88	0.84
Al_2O_3	19.54	19.54	19.51	19.31	19.55	19.43	18.88	19.35	19.33	19.40	19.39	0.40
CaO	0.26	0.11	0.22	0.22	0.17	0.20	0.26	0.18	0.17	0.15	0.19	0.10
Na_2O	11.57	11.34	11.34	11.30	11.28	11.37	11.18	11.21	11.56	11.37	11.35	0.26
K_2O	0.43	0.26	0.33	0.32	0.28	0.33	0.30	0.31	0.31	0.27	0.32	0.10
Tot.	99.67	99.65	99.71	98.42	98.73	99.60	97.99	98.70	99.57	99.22	99.13	1.24

The chemical formula has been calculated on the basis of the theoretical number of cations, as suggested by the protocol by Venturelli and Salvioli, assuming a total amount of cations of 5 *apfu* (atom per formula unit). This method is suitable for minerals free of anions other than oxygens. The chemical formula, averaged on 10 analysis point, is: $(K_{0.02},Na_{0.97})Ca_{0.009}Al_{1.01}Si_{2.99}O_8$.

Table A. 2: Calculation of the crystallographic formula on the basis of the theoretical number of cations.

Oxide (wt.%)	1	2	3	4	5	6	7	12	13	14	Avg.	2σ
SiO_2	1.13	1.14	1.14	1.12	1.12	1.14	1.12	1.13	1.13	1.13	1.13	0.01
Al_2O_3	0.38	0.38	0.38	0.38	0.38	0.38	0.37	0.38	0.38	0.38	0.38	0.01
CaO	0.005	0.002	0.004	0.004	0.003	0.004	0.005	0.003	0.003	0.003	0.003	0.002
Na_2O	0.37	0.37	0.37	0.36	0.36	0.37	0.36	0.36	0.37	0.37	0.37	0.01
K_2O	0.009	0.006	0.007	0.007	0.006	0.007	0.006	0.007	0.007	0.006	0.01	0.002
Sum	1.90	1.89	1.90	1.87	1.88	1.89	1.86	1.88	1.90	1.89	1.89	0.03

Cation	1	2	3	4	5	6	7	12	13	14	Avg.	2σ
Si	2.97	3.01	3.00	2.99	2.99	3.00	3.01	3.00	2.99	3.00	2.99	0.02
Al	1.01	1.01	1.01	1.01	1.02	1.01	0.99	1.01	1.00	1.01	1.01	0.01
Ca	0.012	0.005	0.010	0.010	0.008	0.009	0.012	0.009	0.008	0.007	0.009	0.004
Na	0.98	0.96	0.96	0.97	0.97	0.97	0.97	0.96	0.98	0.97	0.97	0.01
K	0.024	0.015	0.018	0.018	0.016	0.019	0.017	0.018	0.018	0.015	0.018	0.005
Sum	5.00	5.00	5.00	5.00	5.00	5.00	5.00	5.00	5.00	5.00	5.00	0.06

Table A. 3: Calculation of the end member composition (from the calculation of the cation formula).

Endmember	1	2	3	4	5	6	7	12	13	14	Avg.	2σ
Kfs	2.4	1.5	1.9	1.8	1.6	1.9	1.7	1.8	1.7	1.5	1.79	0.49
Ab	96.5	98.0	97.1	97.1	97.6	97.2	97.0	97.3	97.5	97.7	97.30	0.86
An	1.2	0.5	1.0	1.0	0.8	0.9	1.2	0.9	0.8	0.7	0.91	0.44

Appendix B

Structural analysis

Single-crystal X-Ray diffraction (SC-XRD) data have been collected with Xcalibur 4-circle diffractometer at the Earth Sciences Department, University of Milan, equipped with CCD and monochromatized Mo-*K*α radiation, operated at 50 kV and 40 mA. The X-ray diffraction experiments have been performed by G. D. Gatta (Earth Sciences Department, University of Milan) on untreated and *T*-treated crystals of albite from Minas Gerais, Brazil (see Chapter 4), selected under a polarized microscope (*i.e.*, free of zoning, twinning or inclusions). The crystal dimensions were approximately 0.3 x 0.3 x 0.2 mm^3.

X-ray intensity data have been collected at 298 K and up to $2\theta_{max} \sim 72°$. The data collection have been performed with a combination of ω and φ scans, fixing a step size of 1° and a time of 10 s/frame. The diffraction patterns have been all indexed with a *C*-centred lattice as reported in the literature. The intensity data have been then integrated with the computer package CrysAlis (distributed by Agilent on 2013) and corrected for Lorentz-polarization and for absorption effects (by Gaussian integration based upon the physical description of the crystal).

The X-ray intensity data have been then processed with a series of programs implemented in the WinGX package[104], aimed to provide a check of the distribution statistics of the normalized structure factors (*E*'s). The anisotropic structure refinements have been performed with the SHELX-97 software[105], against F^2 and using as starting atomic coordinates those of the structural model of Meneghinello *et al.*[81]. The neutral X-ray scattering curves of Na, Al, Si and O were used according to the *International Tables for Crystallography C*[106]. The secondary isotropic extinction effect has been modelled according to the Larson's formalism[107], as implemented in the SHELXL-97 package[105]. The first cycles of refinement were performed with the three independent tetrahedral sites modelled with the scattering curve of Si (*i.e.,* T_1(m), T_2(o) and T_2(m)) and the further one (*i.e.,*

$T_1(o)$) with the scattering curve of Al (see Table B. 2 and Table B. 3); any attempt to use mixed scattering curves of (Si +Al) did not improve the figures of merit if compared to refinements with the curve of Si and Al alone. For all the refinements, good agreement indexes were obtained (R_1 in Table B. 1). Electron density peaks larger than -0.5/+0.5 $e^-/Å^3$ were not present in the final difference-Fourier map of the electron density for low albite ("untreated" in Table B. 1). As heating increases, significant electron density residuals appear close to the Na atom, up to 1.3 $e^-/Å^3$, and the final R_1 index increases. As the R_{int} does not change significantly, the slight increase in the R_1 index is not explained by a degradation of the crystal. The residuals close to the Na atom and lower agreement can then be explained with positional disorder in the non-tetrahedral site of albite. In ordered albite, Na is present as a single site, with pronounced displacement ellipsoid[108]. In disordered albite, the statistical Al-Si tetrahedral distributions affect the Na atomic positions too. As a consequence, higher residuals are found, with a slightly worse agreement factor if compared to the ordered albite; however, the tetrahedral bond distances do not change significantly[109–111] (see Table B. 2). Refined atomic coordinates and displacement parameters are listed in Table B. 3. The refined albite structure is illustrated in Figure B. 1.

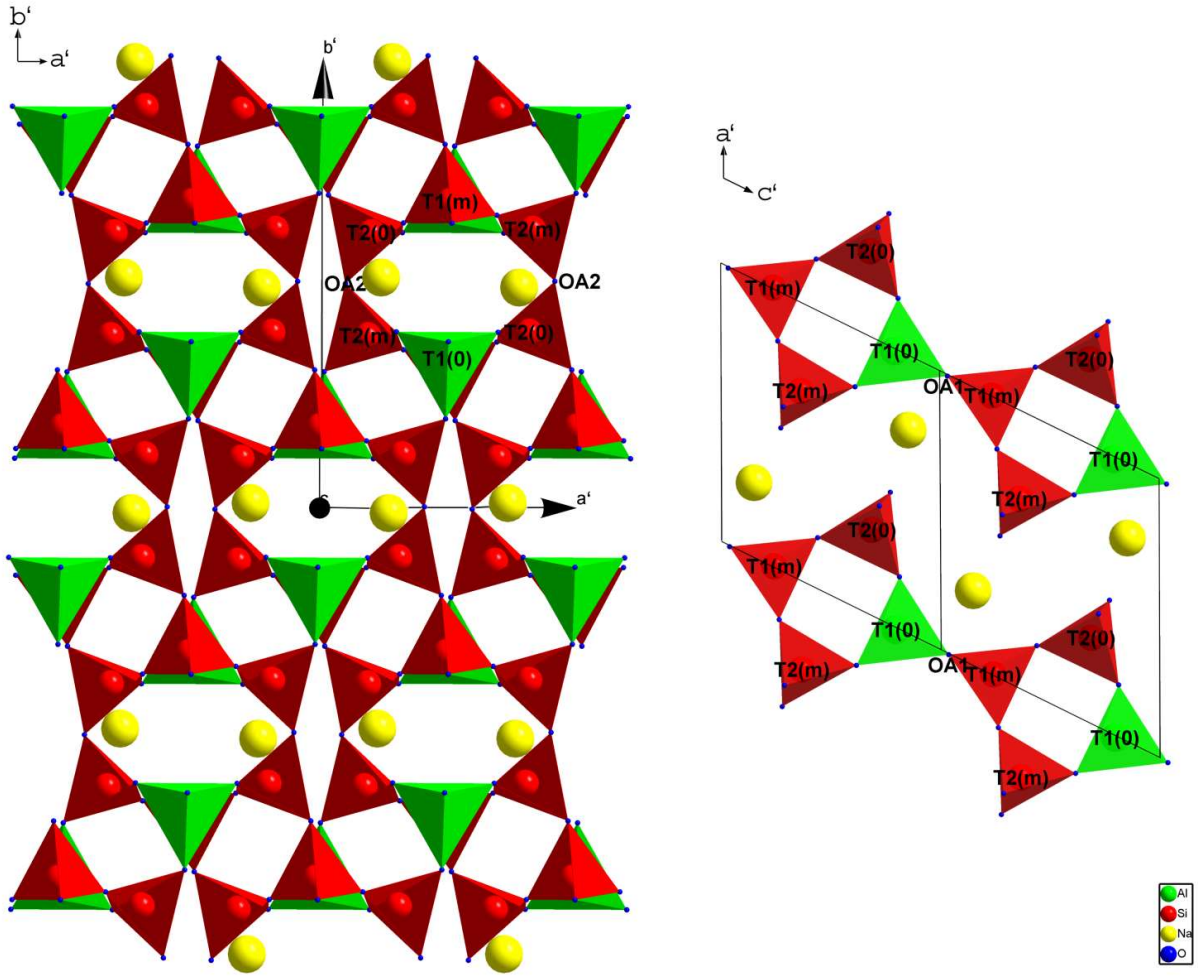

Figure B. 1: Albite structure (*left*: *c* axis projection; *right*: *b* axis projection) obtained by the SC-XRD refinement of a low albite from Minas Gerais (Brazil). The red tetrahedra contain silicon, the green tetrahedra contain aluminium, sodium is shown in yellow. The four non-equivalent tetrahedra are labelled as $T_1(o)$, $T_1(m)$, $T_2(o)$ and $T_2(m)$. The two types of oxygens, *i.e.*, $O_A(1)$ and $O_A(2)$, are also shown.

Table B. 1: Details pertaining to the data collections and structure refinements of albite at different annealing times.

Annealing time (d)	untreated	11	20	25	28	32	40
a (Å)	8.1395(5)	8.1451(3)	8.1563(8)	8.1588(3)	8.1539(4)	8.1588(2)	8.1626(3)
b (Å)	12.7838(7)	12.8053(5)	12.841(1)	12.8663(4)	12.8376(5)	12.8648(4)	12.8724(5)
c (Å)	7.1597(6)	7.1457(3)	7.1285(6)	7.1129(3)	7.1328(3)	7.1202(2)	7.1108(2)
α (°)	94.242(6)	94.164(3)	93.86(1)	93.583(3)	93.933(3)	93.618(2)	93.491(3)
β (°)	116.59(7)	116.556(4)	116.50(1)	116.432(4)	116.521(4)	116.466(3)	116.466(3)
γ (°)	87.674(5)	88.232(3)	89.21(1)	89.943(3)	89.047(3)	89.890(2)	90.184(3)
V (Å^3)	664.35(9)	664.91(9)	668.25(14)	667,00(4)	666.42(5)	667.40(3)	667.22(4)
Space group	$C\bar{1}$	$C\bar{1}$	$C\bar{1}$	$C\bar{1}$	$C\bar{1}$	$C\bar{1}$	$C\bar{1}$
Z	4	4	4	4	4	4	4
T (K)	298	298	298	298	298	298	298
Radiation (Å)	Mo$K\alpha$	Mo$K\alpha$	Mo$K\alpha$	MoKα	MoKα	Mo$K\alpha$	Mo$K\alpha$
Scan type	ω/ϕ scan	ω/ϕ scan	ω/ϕ scan	ω/ϕ scan	ω/ϕ scan	ω/ϕ scan	ω/ϕ scan
Time for step (s)	10	10	10	10	10	10	10
Step width (°)	1	1	1	1	1	1	1
Max 2θ (°)	72.16	72.33	72.03	71.9	72.21	72.34	71.88
	$-12 \le h \le 12$	$-13 \le h \le 13$	$-13 \le h \le 13$	$-12 \le h \le 12$	$-9 \le h \le 10$	$-10 \le h \le 10$	$-11 \le h \le 11$
	$-17 \le k \le 16$	$-17 \le k \le 16$	$-21 \le k \le 21$	$-21 \le k \le 21$	$-20 \le k \le 21$	$-20 \le k \le 20$	$-21 \le k \le 21$
	$-11 \le l \le 11$	$-11 \le l \le 11$	$-9 \le l \le 9$	$-9 \le l \le 9$	$-11 \le l \le 11$	$-11 \le l \le 11$	$-9 \le l \le 8$
No. Measured refl.	9431	8866	9138	9375	9330	9291	9296
No. Unique refl.	1961	1932	1959	1983	1962	1939	1973
No. Unique refl. Fo > 4σ(Fo)	1625	1683	1832	1692	1647	1741	1759
No. Refined parameters	118	118	118	118	118	118	118
R_{int}	0.0336	0.03	0.0173	0.0277	0.0282	0.0199	0.0212
R_1	0.0288	0.0363	0.0345	0.0432	0.0359	0.0342	0.0347
wR_2(all reflections)	0.0587	0.0615	0.0777	0.0827	0.0718	0.0749	0.0839
Residual (e$^-$A^{-3})	-0.50/+0.52	-0.82/+0.87	-1.32/+1.12	-1.22/+1.27	'-1.00/+0.8	-1.35/1.32	-1.36/1.35

$$R_{int} = \sum|F^2_{obs} - F^2_{obs}(\text{mean})|/\sum[F^2_{obs}];\ R_1 = \sum(|F_{obs}| - |F_{calc}|)/\sum|F_{obs}|;$$

$$wR_2 = [\sum[w(F^2_{obs} - F^2_{calc})^2]/\sum[w(F^2_{obs})^2]]^{0.5}$$

Table B. 2: T-O and Na-O distances (Å) as a function of the annealing time.

Annealing time (d)	untreated	11	20	25	28	32	40
$T_1(o)$-$O_A(1)$	1.7456(13)	1.7263(14)	1.6863(17)	1.6541(22)	1.6939(16)	1.6627(16)	1.6431(22)
$T_1(o)$-$O_B(o)$	1.7384(13)	1.7207(13)	1.6846(14)	1.6620(19)	1.6887(20)	1.6621(29)	1.6508(18)
$T_1(o)$-$O_C(o)$	1.7298(15)	1.7121(18)	1.6806(15)	1.6513(18)	1.6867(17)	1.6587(15)	1.6469(17)
$T_1(o)$-$O_D(o)$	1.7435(16)	1.7212(17)	1.6942(17)	1.6679(19)	1.6947(17)	1.6695(16)	1.6557(16)
$<T_1(o)$-O>	1.7393	1.7201	1.6864	1.6588	1.691	1.6633	1.6491
$T_1(m)$-$O_A(1)$	1.5996(14)	1.6084(15)	1.6324(16)	1.6469(22)	1.6285(16)	1.6451(16)	1.6569(20)
$T_1(m)$-$O_B(m)$	1.5966(14)	1.6018(15)	1.6127(14)	1.6254(20)	1.6061(19)	1.6205(20)	1.6294(21)
$T_1(m)$-$O_C(m)$	1.6209(12)	1.6254(18)	1.6338(14)	1.6442(18)	1.6348(16)	1.6433(15)	1.6462(16)
$T_1(m)$-$O_D(m)$	1.6173(14)	1.6207(14)	1.6266(17)	1.6341(19)	1.6266(18)	1.6316(17)	1.6359(16)
$<T_1(m)$-O>	1.6086	1.6141	1.6264	1.6377	1.624	1.6351	1.6421
$T_2(o)$-$O_A(2)$	1.6303(10)	1.6352(16)	1.6425(14)	1.6532(18)	1.6405(17)	1.6497(19)	1.6533(15)
$T_2(o)$-$O_B(o)$	1.5957(13)	1.6046(14)	1.6227(15)	1.6311(21)	1.6213(18)	1.6325(20)	1.6411(21)
$T_2(o)$-$O_C(m)$	1.6141(16)	1.6185(18)	1.6294(15)	1.6323(18)	1.6257(17)	1.6322(16)	1.6357(16)
$T_2(o)$-$O_D(m)$	1.6160(14)	1.6196(14)	1.6237(18)	1.6293(21)	1.6254(16)	1.6304(15)	1.6325(19)
$<T_2(o)$-O>	1.6140	1.6195	1.6296	1.6365	1.6282	1.6362	1.6407
$T_2(m)$-$O_A(2)$	1.6413(16)	1.6444(18)	1.6514(14)	1.6499(18)	1.6475(15)	1.6518(15)	1.6481(16)
$T_2(m)$-$O_B(m)$	1.6219(13)	1.6241(14)	1.6294(15)	1.6275(21)	1.6324(18)	1.6298(20)	1.6273(22)
$T_2(m)$-$O_C(o)$	1.6001(13)	1.6062(14)	1.6250(15)	1.6379(18)	1.6192(18)	1.6332(19)	1.6391(16)
$T_2(m)$-$O_D(o)$	1.6002(14)	1.6130(14)	1.6249(18)	1.6391(22)	1.6266(16)	1.6426(15)	1.6481(19)
$<T_2(m)$-O>	1.6159	1.6219	1.6327	1.6386	1.6314	1.6394	1.6407
<<T-O>>	1.6445	1.6439	1.6438	1.6429	1.6437	1.6435	1.6431
Na-$O_A(2)$	2.3755(16)	2.3657(17)	2.3517(19)	2.3468(22)	2.3537(22)	2.3495(23)	2.3506(21)
Na-$O_D(o)$	2.4421(15)	2.4468(18)	2.4632(20)	2.4911(25)	2.4632(20)	2.4863(21)	2.5008(25)
Na-$O_B(o)$	2.4599(15)	2.4647(16)	2.4912(22)	2.5124(26)	2.4844(20)	2.5055(20)	2.5143(25)
Na-$O_A(1)$	2.5400(16)	2.5647(18)	2.6304(22)	2.6184(27)	2.6204(25)	2.6148(25)	2.6112(25)
Na-$O_A(1)$	2.6702(20)	2.6726(22)	2.6465(22)	2.6847(28)	2.6552(23)	2.6855(27)	2.6961(26)
Na-$O_C(o)$	2.9650(19)						
Na-$O_D(m)$	3.0026(19)	3.0166(21)					
Na-$O_C(m)$				2.9624(29)		2.9651(27)	2.9333(27)
Na-$O_B(m)$							

Table B. 3: Atomic coordinates and U_{eq} ($Å^2$).

untreated					11 d				
Site	x	y	z	U_{eq}	Site	x	y	z	U_{eq}
T_1(o)	0.00874(8)	0.16863(5)	0.20817(9)	0.00700(15)	T_1(o)	0.00874(8)	0.16783(6)	0.20928(9)	0.00852(16)
T_1(m)	0.00377(7)	0.82047(5)	0.23737(8)	0.00646(13)	T_1(m)	0.00386(7)	0.81900(6)	0.23578(8)	0.00885(15)
T_2(o)	0.69180(7)	0.11032(4)	0.31497(8)	0.00636(13)	T_2(o)	0.69151(7)	0.10987(5)	0.31552(8)	0.00918(15)
T_2(m)	0.68153(7)	0.88197(4)	0.36074(8)	0.00659(13)	T_2(m)	0.68241(7)	0.88101(5)	0.35970(8)	0.00913(15)
Na	0.26853(12)	0.98884(9)	0.14646(15)	0.03241(30)	Na	0.26977(13)	0.99158(12)	0.14543(18)	0.04853(42)
O_A(1)	0.00504(19)	0.13129(11)	0.96683(20)	0.01093(33)	O_A(1)	0.00485(20)	0.13222(13)	0.96964(21)	0.01489(38)
O_A(2)	0.59293(18)	0.99738(11)	0.28079(20)	0.00794(31)	O_A(2)	0.59301(18)	0.99592(13)	0.28013(20)	0.01123(36)
O_B(o)	0.81245(19)	0.11043(11)	0.19030(21)	0.01258(34)	O_B(o)	0.81371(19)	0.11007(13)	0.1910(22)	0.01579(40)
O_B(m)	0.82044(20)	0.85096(12)	0.25864(23)	0.01604(36)	O_B(m)	0.82022(20)	0.84997(14)	0.25617(23)	0.01864(42)
O_C(o)	0.01311(18)	0.30217(11)	0.27035(21)	0.01088(33)	O_C(o)	0.01421(19)	0.29968(13)	0.27216(21)	0.01435(38)
O_C(m)	0.02411(18)	0.69377(11)	0.23017(21)	0.01074(32)	O_C(m)	0.02342(19)	0.69224(13)	0.22783(21)	0.01415(38)
O_D(o)	0.20728(18)	0.10931(11)	0.38943(20)	0.01152(33)	O_D(o)	0.20422(19)	0.10997(13)	0.38811(20)	0.01404(38)
O_D(m)	0.18346(19)	0.86803(11)	0.43622(21)	0.01345(34)	O_D(m)	0.18407(19)	0.86783(13)	0.43456(21)	0.01636(40)

20 d					25 d				
Site	x	y	z	U_{eq}	Site	x	y	z	U_{eq}
T_1(o)	0.00877(8)	0.16636(4)	0.21179(11)	0.00813(15)	T_1(o)	0.00901(9)	0.16554(5)	0.21366(13)	0.00776(19)
T_1(m)	0.00440(7)	0.81669(4)	0.23270(10)	0.01058(14)	T_1(m)	0.00465(9)	0.81529(5)	0.22989(13)	0.01205(19)
T_2(o)	0.69125(7)	0.10895(4)	0.31765(10)	0.01052(15)	T_2(o)	0.69075(9)	0.10841(5)	0.31934(14)	0.01197(19)
T_2(m)	0.68399(7)	0.87927(4)	0.35732(10)	0.01062(14)	T_2(m)	0.68481(9)	0.87824(5)	0.35486(13)	0.01174(19)
Na	0.27176(16)	0.99882(15)	0.14090(27)	0.07979(64)	Na	0.27297(19)	1.00497(19)	0.13486(32)	0.09158(89)
O_A(1)	0.00493(21)	0.13375(11)	0.97672(26)	0.01838(37)	O_A(1)	0.00493(25)	0.13479(14)	0.98228(33)	0.01949(48)
O_A(2)	0.59274(20)	0.99358(10)	0.27955(26)	0.01509(34)	O_A(2)	0.59214(23)	0.99152(13)	0.27852(32)	0.01561(46)
O_B(o)	0.81753(20)	0.10917(11)	0.19480(28)	0.01909(37)	O_B(o)	0.81989(25)	0.10909(14)	0.19829(35)	0.02063(50)
O_B(m)	0.81969(21)	0.84810(12)	0.25101(29)	0.02179(39)	O_B(m)	0.81876(25)	0.84733(15)	0.2470(36)	0.02369(53)
O_C(o)	0.01518(20)	0.29520(11)	0.27515(27)	0.01753(36)	O_C(o)	0.01619(23)	0.29179(14)	0.27627(33)	0.01816(47)
O_C(m)	0.02234(20)	0.68977(11)	0.22339(27)	0.01796(36)	O_C(m)	0.02200(24)	0.68795(14)	0.21960(32)	0.01902(49)
O_D(o)	0.20033(20)	0.11074(11)	0.38829(26)	0.01746(35)	O_D(o)	0.19731(24)	0.11205(13)	0.38824(32)	0.01758(47)
O_D(m)	0.18577(21)	0.86714(11)	0.43125(27)	0.01892(36)	O_D(m)	0.18733(24)	0.86734(14)	0.42805(33)	0.01993(50)

28 d

Site	x	y	z	U_{eq}
T_1(o)	0.00863(11)	0.16652(5)	0.21125(9)	0.00867(17)
T_1(m)	0.00412(10)	0.81699(5)	0.23319(9)	0.01102(17)
T_2(o)	0.69125(10)	0.10902(4)	0.31717(9)	0.01100(16)
T_2(m)	0.68358(10)	0.87947(4)	0.35760(9)	0.01112(16)
Na	0.27187(18)	0.99743(15)	0.14195(24)	0.07557(63)
O_A(1)	0.00493(24)	0.13351(12)	0.97535(23)	0.01826(42)
O_A(2)	0.59334(24)	0.99381(12)	0.28001(23)	0.01459(38)
O_B(o)	0.81665(25)	0.10949(12)	0.19358(25)	0.01924(42)
O_B(m)	0.82010(26)	0.84817(13)	0.25176(27)	0.02181(43)
O_C(o)	0.01514(24)	0.29595(12)	0.27429(24)	0.01720(40)
O_C(m)	0.02268(24)	0.68996(12)	0.22351(24)	0.01748(40)
O_D(o)	0.20043(23)	0.11077(12)	0.38786(23)	0.01719(41)
O_D(m)	0.18564(25)	0.86733(12)	0.43151(24)	0.01841(41)

32 d

Site	x	y	z	U_{eq}
T_1(o)	0.00878(9)	0.16554(4)	0.21352(8)	0.00743(16)
T_1(m)	0.00446(9)	0.81540(4)	0.23027(8)	0.01130(16)
T_2(o)	0.69097(9)	0.10846(4)	0.31902(8)	0.01137(16)
T_2(m)	0.68477(9)	0.87827(4)	0.35506(8)	0.01135(16)
Na	0.27289(21)	1.00504(17)	0.13471(28)	0.09194(78)
O_A(1)	0.00503(25)	0.13464(12)	0.98130(22)	0.01967(42)
O_A(2)	0.59259(24)	0.99187(11)	0.27876(22)	0.01595(37)
O_B(o)	0.81947(26)	0.10889(12)	0.19708(25)	0.02047(41)
O_B(m)	0.81925(26)	0.84763(13)	0.24743(26)	0.02258(42)
O_C(o)	0.01602(24)	0.29246(11)	0.27565(23)	0.01770(39)
O_C(m)	0.02220(24)	0.68813(11)	0.21989(23)	0.01868(40)
O_D(o)	0.19741(24)	0.11179(11)	0.38764(22)	0.01755(39)
O_D(m)	0.18680(25)	0.86722(11)	0.42840(23)	0.02000(41)

40 d

Site	x	y	z	U_{eq}
T_1(o)	0.00897(8)	0.16522(4)	0.21434(11)	0.00712(17)
T_1(m)	0.00474(8)	0.81487(4)	0.22912(11)	0.01160(18)
T_2(o)	0.69061(8)	0.10815(4)	0.31999(11)	0.01144(18)
T_2(m)	0.68497(8)	0.87785(4)	0.35391(11)	0.01119(18)
Na	0.27341(18)	1.00646(18)	0.13346(32)	0.09232(88)
O_A(1)	0.00512(24)	0.13486(12)	0.98456(30)	0.01957(45)
O_A(2)	0.59258(21)	0.99087(11)	0.27815(28)	0.01570(43)
O_B(o)	0.82076(23)	0.10902(12)	0.19854(31)	0.02010(46)
O_B(m)	0.81865(24)	0.84721(14)	0.24596(32)	0.02287(47)
O_C(o)	0.01612(21)	0.29113(12)	0.27590(30)	0.01759(43)
O_C(m)	0.02168(22)	0.68746(12)	0.21888(29)	0.01850(45)
O_D(o)	0.19589(22)	0.11243(12)	0.38768(28)	0.01761(44)
O_D(m)	0.18680(25)	0.86722(11)	0.42840(23)	0.02000(41)

Appendix C

Estimation of the order parameter

The most direct method for estimating degree of Al-Si order in feldspars is by structure determination, even if Si and Al having similar scattering powers. Several methods have been devised for using X-ray structural data to determine Al/Si proportions in each site and hence the degree of order.

The most common method is based on the (Si,Al)-O bond distances and their relation to distances for sites with only Si and only Al. Distances for Si-O and Al-O bonds have been proposed by various workers. Ribbe and Gibbs[112] used values of 1.605 Å and 1.757 Å to derive the simple relationship:

$$\frac{Al}{(Al+S)} = 6.58(< T-O > -1.605) \qquad (1)$$

where $< T-O >$ is the mean T-O distance for a tetrahedron.

Individual T-O bond lengths in aluminosilicates are affected by many factors[15]. The Al-Si content of the site is the primary factor, but also the Al-Si content of the second tetrahedral site, to which the oxygen is bonded, influences too. Indeed, an individual Si-O bond could be ~ 0.03 Å longer, if the oxygen atom is bonded to another Si than if it is bonded to Al in albites. However, the fact that $\ll T-O \gg$ is invariant with Q_{od} demonstrates that in $C\bar{1}$ albites, as in $I\bar{1}$ feldspars, this linkage factor is internally compensated within each individual tetrahedron. The bonding of extra framework cations to the bridging oxygen tends to increase the T-O bond lengths, whereas an inverse correlation of T-O bond lengths with T-O-T angles exists in framework silicates. Studies on fully ordered framework structures have also suggested that the T-O distance is correlated with the O-T-O angles.

In 1975, Ribbe proposed using differences in T-O distances rather than absolute values as follows:

$$t_{1(0)} - t_{1(m)} = (< T_{1(0)} - O > - < T_{1(m)} - O >)/0.13 \qquad (2)$$

$$t_{1(0)} - t_{2(0)} = (< T_{1(0)} - O > - < T_{2(0)} - O >)/0.13 \quad (3)$$

$$t_{1(0)} - t_{2(m)} = (< T_{1(0)} - O > - < T_{2(m)} - O >)/0.13 \quad (4)$$

where, together with $t_{1(0)} + t_{1(m)} + t_{2(0)} + t_{2(m)} = 1$, give $t_{1(0)}, t_{1(m)}, t_{2(0)}, t_{2(m)}$. Kroll and Ribbe[82] recommended the use of the constant 0.130 for K-rich and 0.125 for Na-rich alkali feldspars and plagioclase. Moreover, they related the Al content of a tetrahedral site to T-O bond distances as follows:

$$t_i = 0.25 * (1 + n_{an}) + (< T_i - O > - << T - O >>)/constant. \quad (5)$$

t_i is the average Al content of a tetrahedron, also called its Al site occupancy, *i.e.*, the number of Al atoms occupying T_i tetrahedra divided by the number of tetrahedra. t_i ranges between 0 and 1; the Si content is $1 - t_i$. n_{an} is the mole fraction of Ca-feldspar. The number of Al atoms in one feldspar formula unit, *i.e.*, $(K, Na)_{1-x}Ca_xAl_{1+x}Si_{3-x}O_8$, is $1 + x$, where x is equivalent to n_{An}. One unit cell (with c ~ 7 Å) contains four formula units, *i.e.* $4(1 + n_{An})$ Al atoms. There are 16 tetrahedra in one unit cell, therefore the average tetrahedral Al content is:

$$< t >= 0.25(1 + n_{An}) \quad (6)$$

and the sum of individual occupancies corresponding to one formula unit is:

$$\Sigma t = 2(t_1 + t_2) = (1 + n_{An}), \text{ for monoclinic structures} \quad (7)$$

$$\Sigma t = t_1 o + t_1 m + t_2 o + t_2 m = (1 + n_{An}), \text{ for triclinic structures.} \quad (8)$$

$< T_i - O >$ is the mean of four (Si,Al)-O bond lengths for the T_i tetrahedron, and $<< T - O >>$ is the grand mean of all non-equivalent T-O bond lengths in the unit cell (16 and 8 for triclinic and monoclinic feldspars, respectively).

The constant is $\ll Al - O \gg - << Si - O >>$, and is 0.130 Å and 0.125 Å for K- and Na-rich feldspars respectively, assuming that low microcline and low albite are fully ordered.

Equation (5) eliminates some uncertainties of the previous Ribbe's model, that arose from the fact that the mean Al-O and Si-O distances are different in the different ordered structures (*e.g.*, low albite, microcline and anorthite-*P*), but it does not permit an independent determination of Σt apart from a knowledge of n_{An}.

We can eliminate the knowledge of the An content (*i.e.*, n_{An}), if we express $< t >$ in terms of $\ll T - O \gg$. We have to keep in mind that the $\ll T - O \gg$ distances of ordered feldspars

(especially alkali feldspars and sodic plagioclases) are slightly larger than those of their disordered equivalents. Excluding An-rich plagioclases, the following equation has been found (for more details about the numerical terms, see the regression analysis of data listed in Table 1, 2 and 3 in the work by Kroll and Ribbe[82]):

$$< t > = 0.25(1 + n_{An}) =$$

$$-11.215 + 6.981 \ll T - O \gg + 0.124\,(< T_1o - O > - < T_1m - O >). \qquad (9)$$

The third term on the right accounts for the amount of the order present. The values of $< t >$ expected from chemical composition are reproduced with a standard deviation of ± 0.005 $\mathrm{Al/Al + Si}$, corresponding to ± 2 mol % An.

An analogous equation for An-rich plagioclases is:

$$< t > = -12.088 + 7.491 \ll T - O \gg. \qquad (10)$$

Combination of Eq. (9) or (10) with Eq. (5) allows to derive site occupancies from $< T_i - O >$ distances without making reference to chemical composition. In Table C. 1, the comparison between the results obtained by the two methods for a Na-feldspar is presented.

Table C. 1: Al contents in tetrahedral sites of albite. Method A: it is calculated as reported in Eq. (5), n_{An} is estimated 0.009 mol%; method B: it is calculated following Eq. (9), without using the An content.

	Method A				Method B				
	Al content				Al content				
Annealing days	$t_{1(o)}$	$t_{1(m)}$	$t_{2(o)}$	$t_{2(m)}$	$t_{1(o)}$	$t_{1(m)}$	$t_{2(o)}$	$t_{2(m)}$	<t>
0	0.96	-0.01	0.03	-0.10	0.98	0.02	0.06	0.07	0.27
11	0.82	0.03	0.07	0.09	0.84	0.05	0.09	0.11	0.26
20	0.57	0.12	0.15	0.17	0.58	0.14	0.16	0.19	0.26
32	0.41	0.20	0.21	0.23	0.41	0.20	0.21	0.23	0.26
40	0.30	0.24	0.23	0.23	0.30	0.25	0.24	0.24	0.26

From the amount of the Al content, we can estimate the degree of order in the structure. A quantitative assessment of the disordering process is obtained by the order parameter Q_{od}.

Q_{od} can be calculated using different relations according to the structure type.

In pure anorthite (An_{100}), the order parameter Q_{od} for Al-Si ordering can be defined in terms of actual site occupancies as:

$$Q_{od} = < Al >_{Al} - < Al >_{Si} \qquad (11)$$

where $< Al >_{Al}$ is the average fractional occupancy by Al of the Al-rich sites, and $< Al >_{Si}$ is the average fractional occupancy by Al of the Si-rich sites[15]. If a linear relationship between the $< T - O >$ distances and the site occupancies is assumed, Q_{od} may be given directly in terms of the bond lengths:

$$Q_{od} = \ll Al - O \gg - \ll Si - O \gg / K \qquad (12)$$

where $\ll Al - O \gg$ is the mean bond length of the four Al-rich sites in $I\bar{1}$ structures, and $\ll Si - O \gg$ is the mean bond lengths of the four Si-bearing sites, and $K = < Al - O > - < Si - O > = 0.135(2)$ Å. Q_{od} is thus normalized to vary between zero (fully disordered) and unity (fully ordered).

Following Carpenter[84], the relation can be simplified for ordering under $C\bar{1}$ symmetry as:

$$Q_{od} = < T_1o - O > - < T_1m - O > / K \qquad (13)$$

The Q_{od} reported in Chapter 5 have been calculated from the average bond lengths obtained by SC-XRD refinements following Eq. (13).

More general equations to estimate the degree of order are the following:

$$Q_{od} = (t_1 - t_2)/(t_1 + t_2) \text{ for monoclinic structures} \qquad (14)$$

or

$$Q_{od} = (t_{1(0)} - t_{1(m)})/(t_{1(0)} + t_{1(m)}) \text{ for triclinic structures.} \qquad (15)$$

In Table C. 2, the comparison between the results of the untreated and *T*-treated albite crystals obtained by Eq. (13) and (15) are listed.

Table C. 2: Order parameters Q_{od} estimated for each annealing step. Method A: it is calculated as reported in Eq. (13); method B: it is calculated following Eq. (15), using the An content calculated with Eq. (5).

	Method A	Method B
Annealing days	Q_{od}	Q_{od}
0	0.968	1.028
11	0.785	0.926
20	0.445	0.643
32	0.157	0.342
40	0.052	0.096

8. Bibliography

1. W. H. Taylor, *Zeitschrift für Krist. Mater.*, 1933, **85**, 425–442.
2. J. J. Freeman, A. Wang, K. E. Kuebler, B. L. Jolliff, and L. A. Haskin, *Can. Mineral.*, 2008, **46**, 1477–1500.
3. A. Wang, K. Kuebler, B. Jolliff, and L. a. Haskin, *J. Raman Spectrosc.*, 2004, **35**, 504–514.
4. V. Bendel and B. C. Schmidt, *Eur. J. Mineral.*, 2008, **20**, 1055–1065.
5. Machatschki, *Zentralbl. Miner. Abt A*, 1928, 97–104.
6. J. V. Smith, *Feldspar Minerals I. Crystal Structure and Physical Properties.*, Heidelberg (Germany), Springer V., 1974.
7. J. V. Smith and F. Rinaldi, *Mineral. Mag.*, 1962, **33**, 202–212.
8. H. D. Megaw, in *The Feldspars*, eds. W. S. MacKenzie and J. Zussman, Manchester University Press, 1974, pp. 2–24.
9. R. J. Angel, L. M. Sochalski-Kolbus, and M. Tribaudino, *Am. Mineral.*, 2012, **97**, 765–778.
10. A. Putnis, *Introduction to mineral sciences*, Cambridge University Press, Edinburgh, 1992.
11. P. H. Ribbe, *Feldspars in Mineralogy. Reviews in Mineralogy.*, Mineralogical Society of America, 2nd edn., 1983.
12. W. A. Deer, R. A. Howie, and J. Zussman, in *Rock forming minerals*, The Geological Society, London, 2nd edn., 2001.
13. P. H. Ribbe, in *Feldspar Mineralogy (Reviews in Mineralogy)*, ed. P. H. Ribbe, Mineralogical Society of America, Washington (USA), 2nd edn., 1983, pp. 1–19.
14. J. V. Smith and V. L. Brown, *Feldspar Minerals. 1. Crystal Structures, Physical, Chemical and Microtextural Properties*, Berlin (Germany), Springer V., 1988.
15. R. J. J. Angel, M. a. Carpenter, and L. W. Finger, *Am. Mineral.*, 1990, **7**, 150–162.
16. M. A. Carpenter, *Phys. Chem. Miner.*, 1986, **53**, 119–139.
17. M. A. Carpenter, *Am. Mineral.*, 1991, **76**, 1110–1119.

18. W. L. Brown and I. Parson, *Mineral. Mag.*, 1989, **53**, 25–42.
19. J. W. Anthony, R. A. Bideaux, K. . W. Bladh, and M. C. Nichols, Eds., *Handbook of Mineralogy*, Mineralogical Society of America, Chantilly, VA 20151-1110, USA, 1995.
20. M. Prencipe, Y. Noel, B. Civalleri, C. Roetti, and R. Dovesi, *Phys. Chem. Miner.*, 2006, **33**, 519–532.
21. M. Prencipe, Y. Noel, M. Bruno, and R. Dovesi, *Am. Mineral.*, 2009, **94**, 986–994.
22. M. Prencipe, L. Mantovani, M. Tribaudino, D. Bersani, and P. P. Lottici, *Eur. J. Mineral.*, 2012, **24**, 457–464.
23. M. Prencipe, L. Maschio, B. Kirtman, S. Salustro, A. Erba, and R. Dovesi, *J. Raman Spectrosc.*, 2014, **45**, 703–709.
24. L. Maschio, R. Demichelis, R. Orlando, M. D. La Pierre, A. Mahmoud, and R. Dovesi, *J. Raman Spectrosc.*, 2014, **45**, 710–715.
25. I. Aliatis, E. Lambruschi, L. Mantovani, D. Bersani, S. Andò, G. D. Gatta, P. Gentile, E. Salvioli-Mariani, M. Prencipe, M. Tribaudino, and P. P. Lottici, *J. Raman Spectrosc.*, 2015, **46**, 501–508.
26. V. M. Goldschmidt, in *Atlas der Krystallformen*.
27. R. Dovesi, V. R. Saunders, C. Roetti, R. Orlando, C. M. Zicovich-Wilson, F. Pascale, B. Civalleri, K. Doll, N. M. Harrison, I. J. Bush, P. D'arco, M. Llunel, M. Causà, and Y. Noel, *Crystal 2014 User's Manual*, University of Torino, Torino, 2013.
28. Z. Wu and R. Cohen, *Phys. Rev. B*, 2006, **73**, 235116.
29. C. Lee, W. Yang, and R. G. Parr, *Phys. Rev. B*, 1988, **37**, 785–789.
30. H. J. Monkhorst and J. D. Pack, *Phys. Rev. B*, 1976, **13**, 5188–5192.
31. B. Civalleri, P. D'Arco, R. Orlando, V. R. Saunders, and R. Dovesi, *Chem. Phys. Lett.*, 2001, **348**, 131–138.
32. M. Prencipe, I. Scanavino, F. Nestola, M. Merlini, B. Civalleri, M. Bruno, and R. Dovesi, *Phys. Chem. Miner.*, 2011, **38**, 223–239.
33. F. Birch, in *Handbook of physical constants*, ed. S. P. Clark, Geol. Soc. Am. Mem., 1966, pp. 97–174.
34. M. D. Benusa, R. J. R. J. Angel, and N. L. Ross, *Am. Mineral.*, 2005, **90**, 1115–1120.
35. F. Pascale, *J. Comput. Chem.*, 2004, **25**, 888–897.
36. L. Maschio, B. Kirtman, R. Orlando, and M. Rèrat, *J. Chem. Phys.*, 2012, **137**, 204113.
37. L. Maschio, B. Kirtman, M. Rérat, R. Orlando, and R. Dovesi, *J. Chem. Phys.*, 2013, **139**, 164101.
38. D. A. McKeown, *Am. Mineral.*, 2005, **90**, 1506–1517.
39. R. Loudon, *J. Phys. Fr.*, 1965, **26**, 677–683.
40. M. Zhang, B. Wruck, A. G. Barber, E. K. H. Salje, and M. A. Carpenter, 1996, **81**, 92–104.
41. E. Salje, *Phys. Chem. Miner.*, 1986, **13**, 340–346.
42. B. Velde and H. Boyer, *J. Geophys. Res.*, 1985, **90**, 3675–3682.
43. B. Velde, Y. Syono, M. Kikuchi, and H. Boyer, *Phys. Chem. Miner.*, 1989, **16**, 436–441.
44. H. G. M. Edwards, S. E. J. Villar, J. Jehlicka, and T. Munshi, *Spectrochim. Acta Part A Mol. Biomol. Spectrosc.*, 2005, **61**, 2273–2280.
45. S. E. Jorge Villar and H. G. M. Edwards, *Vib. Spectrosc.*, 2005, **39**, 88–94.

46. P. Makreski, G. Jovanovski, and B. Kaitner, *J. Mol. Struct.*, 2009, **924-926**, 413–419.

47. J. Fritz, A. Greshake, and D. Stoffler, *Antarct. Meteor. Res.*, 2005, **18**, 96–116.

48. T. P. Mernagh, *J. Raman Spectrosc.*, 1991, **22**, 453–457.

49. M. O. von Stengel, *Z. Krist.*, 1977, **146**, 1–18.

50. M. Méheut and E. A. Schauble, *Geochim. Cosmochim. Acta*, 2014, **134**, 137–154.

51. J. P. Perdew, K. Burke, and M. Ernzerhof, *Phys. Rev. Lett.*, 1996, **77**, 3865.

52. W. B. White, in *Infrared and Raman spectroscopy of lunar and terrestrial materials*, ed. C. Karr, New York, Academic P., 1975, p. 343.

53. E. Salje, *Phys. Chem. Miner.*, 1985, **12**, 93–98.

54. E. Salje, B. Kuscholke, B. Wruck, and H. Kroll, *Phys. Chem. Miner.*, 1985, **12**, 99–107.

55. E. Salje, B. Guttler, and C. Ormerod, *Phys. Chem. Miner.*, 1989, **16**, 576–581.

56. M. Zhang, E. K. H. Salje, M. A. Carpenter, I. Parsons, H. Kroll, S. J. B. Reed, and A. Graeme-Barber, *Am. Mineral.*, 1997, **82**, 849–857.

57. A. J. Atkinson, M. A. Carpenter, and E. K. H. Salje, *Eur. J. Mineral.*, 1999, **11**, 7–21.

58. R. Couty and B. Velde, *Am. Mineral.*, 1986, **71**, 99–104.

59. I. Daniel, P. Gillet, and S. Ghose, *Am. Mineral.*, 1995, **80**, 645–648.

60. I. Daniel, P. Gillet, P. F. McMillan, G. Wolf, and M. a. Verhelst, *J. Geophys. Res.*, 1997, **102**, 10313.

61. R. J. Angel, *Am. Mineral.*, 1992, **77**, 923–929.

62. R. J. Angel, *Contrib. to Mineral. Petrol.*, 2004, **146**, 506–512.

63. R. J. Angel, N. L. Ross, J. Zhao, L. M. Sochalski-Kolbus, H. Kruger, and B. C. Schmidt, *Eur. J. Mineral.*, 2013, **25**, 597–614.

64. R. T. Downs, H. Yang, R. M. Hazen, L. W. Finger, and C. T. Prewitt, *Am. Mineral.*, 1999, **84**, 333–340.

65. R. Angel, *Am. Mineral.*, 1988, **73**, 1114–1119.

66. R. J. Angel, R. M. Hazen, T. C. McCormick, C. T. Prewitt, and J. R. Smith, *Phys. Chem. Miner.*, 1988, **15**, 313–318.

67. R. J. Angel, D. R. Allan, R. Miletich, and L. W. Finger, *J. Appl. Crystallogr.*, 1997, **30**, 461–466.

68. G. D. Gatta and Y. Lee, *Mineral. Mag.*, 2014, **78**, 267–291.

69. M. Tribaudino, R. J. Angel, F. Cámara, F. Nestola, D. Pasqual, and I. Margiolaki, *Contrib. to Mineral. Petrol.*, 2010, **160**, 899–908.

70. M. Tribaudino, M. Bruno, F. Nestola, D. Pasqual, and R. J. Angel, *Am. Mineral.*, 2011, **96**, 992–1002.

71. L. M. Sochalski-Kolbus, R. J. Angel, and F. Nestola, *Mineral. Mag.*, 2010, **74**, 943–950.

72. R. T. Downs, R. M. Hazen, and L. W. Finger, *Am. Mineral.*, 1994, **79**, 1042–1052.

73. R. J. Angel, M. Bujak, J. Zhao, G. D. Gatta, and S. D. Jacobsen, *J. Appl. Crystallogr.*, 2007, **40**, 26–32.

74. H. K. Mao, J. Xu, and P. M. Bell, *J. Geophys. Res.*, 1986, 91, 4673.

75. A. D. Chijioke, W. J. Nellis, A. Soldatov, and I. F. Silvera, *J. Appl. Phys.*, 2005, **98**, 1–9.

76. R. Miletich, D. R. Allan, and W. F. Kuhs, in *High-temperature and high-pressure crystal chemistry. Reviews in*

Mineralogy and Geochemistry, eds. R. M. Hazen and R. T. Downs, 2000, vol. 41, pp. 445–519.

77. https://en.wikipedia.org/wiki/Diamond_anvil_cell, .
78. Y. Ohashi and C. W. Burnham, *Am. Mineral.*, 1973, **58**, 843–849.
79. H. D. Megaw, in *The Feldspars*, eds. W. S. MacKenzie and J. Zussman, Manchester University Press, 1974, pp. 87–113.
80. X. Rocquefelte, F. Clabau, M. Paris, P. Deniard, T. Le Mercier, S. Jobic, and M. H. Whangbo, *Inorg. Chem.*, 2007, **46**, 5456–5458.
81. E. Meneghinello, A. Alberti, and G. Cruciani, *Am. Mineral.*, 1999, **84**, 1144–1151.
82. H. Kroll and P. H. Ribbe, in *Feldspar Mineralogy (Reviews in mineralogy 2)*, ed. P. H. Ribbe, Mineralogical Society of America, 1983, vol. 2, pp. 57–99.
83. G. L. Hovis, in *Teaching Mineralogy*, eds. J. Brady, D. Mogk, and D. Perkins, Mineralogical Society of America, 1997, pp. 107–118.
84. M. A. Carpenter, in *Physical properties and thermodynamic behaviour of minerals*, ed. E. H. K. Salje, NATO ASI Series C225, Dordrecht, Reidel., 1988, pp. 265–323.
85. H. Kroll, H. U. Bambauer, and U. Schirmer, *Am. Mineral.*, 1980, **65**, 1192–1211.
86. D. Bersani, P. P. Lottici, and X. Z. Ding, *Appl. Phys. Lett.*, 1998, **72**, 73–75.
87. R. T. Downs, *Elements*, 2015, **1**, 45–50.
88. A. Wang, J. J. Freeman, and B. L. Jolliff, *J. Raman Spectrosc.*, 2015, n/a–n/a.
89. J. R. Petriglieri, E. Salvioli-Mariani, L. Mantovani, M. Tribaudino, P. P. Lottici, C. Laporte-Magoni, and D. Bersani, *J. Raman Spectrosc.*, 2015, **46**, 953–958.
90. D. Bersani, S. Andò, P. Vignola, G. Moltifiori, I.-G. Marino, P. P. Lottici, and V. Diella, *Spectrochim. Acta Part A Mol. Biomol. Spectrosc.*, 2009, **73**, 484–491.
91. M. A. Carpenter, J. D. C. McConnell, and A. Navrotsky, *Geochim. Cosmochim. Acta*, 1985, **49**, 947–966.
92. E. H. Slimming, *Am. Mineral.*, 1976, **61**, 54–59.
93. D. I. Godfrey-Smith and M. Cada, *Radiat. Prot. Dosimetry*, 1996, **66**, 379–385.
94. A. Benisek, H. Kroll, L. Cemic, V. Kohl, U. Breit, and B. Heying, *Contrib. to Mineral. Petrol.*, 2003, **145**, 390–390.
95. A. Benisek, E. Dachs, and M. A. Carpenter, *Phys. Chem. Miner.*, 2013, **40**, 167–173.
96. A. Benisek, E. Dachs, and H. Kroll, *Am. Mineral.*, 2009, **94**, 1153–1161.
97. G. L. Hovis, *J. Petrol.*, 1988, **29**, 731–763.
98. R. Le Parc, B. Champagnon, J. Dianoux, P. Jarry, and V. Martinez, *J. Non. Cryst. Solids*, 2003, **323**, 155–161.
99. F. A. Seifert, B. O. Mysen, and D. Virgo, *Am. Mineral.*, 1982, **67**, 696–717.
100. B. Wopenka, J. J. Freeman, and T. Nikischer, *Appl. Spectrosc.*, 1998, **52**, 54–63.
101. S. K. Sharma, B. Simons, and H. S. Yoder, *Am. Mineral.*, 1983, **68**, 1113–1125.
102. E. Stolper, *Geochim. Cosmochim. Acta*, 1977, **41**, 587–611.
103. B. Mason, *Meteoritics*, 1971, **6**, 59–70.

104. L. J. Farrugia, *J. Appl. Crystallogr.*, 1999, **32**, 837–838.

105. G. M. Sheldrick, *Acta Crystallogr. Sect. A*, 2008, **64**, 112–122.

106. E. Prince, Ed., *International Tables for Crystallography, Vol.C: Mathematical, physical and chemical tables*, Kluver academic publishers, Dordrecht, third edit., 2013, vol. C.

107. A. C. Larson, *Acta Crystallogr.*, 1967, **23**, 664–665.

108. J. K. Winter, S. Ghose, and F. P. Okamura, *Am. Miner.*, 1977, **62**, 921–931.

109. J. K. Winter, F. P. Okamura, and S. Ghose, *Am. Miner.*, 1979, **64**, 409–423.

110. J. E. Post and C. W. Burnham, *Am. Mineral.*, 1987, **72**, 507–514.

111. C. T. Prewitt, S. Sueno, and J. J. Papike, *Am. Mineral.*, 1976, **61**, 12313–1225.

112. P. H. Ribbe and G. V. Gibbs, *Am. Miner.*, 1969, **54**, 85–94.

RINGRAZIAMENTI

Ringrazio il Prof. Lottici e il Prof. Bersani per avermi dato l'opportunità di lavorare ancora nel loro gruppo di ricerca. Un grazie particolare va al Prof. Lottici che ha deciso di seguire con meticolosità il mio progetto di tesi. Ringrazio il Prof. Tribaudino per avermi fatto conoscere il mondo dei feldspati, minerali così comuni ma così difficili da studiare. Ringrazio il Prof. Gatta per i consigli e i risultati conseguiti insieme. Ringrazio inoltre tutti coloro che hanno collaborato a questo progetto: il Prof. Baraldi, la Prof.ssa Salvioli, il Prof. Prencipe, il Prof. Andò, il Dott. Gentile. Un grazie particolare al Prof. Angel che ha saputo trasmettermi il suo entusiasmo per lo studio dei feldspati in questo ultimo anno di dottorato. Grazie al Prof. Benisek e al Prof. Carpenter per aver fornito i campioni oggetto dei risultati più interessanti della tesi.

Ringrazio le "ragazze di geologia", Luciana e le Claudie. Ringrazio tutto il gruppo dei dottorandi per aver riempito questi tre anni di momenti divertenti, un particolare grazie ad Alice Chiara, Marco, Gio, Ely, Micio, Laura e Ubi. Da ultimo, ma non ultima, grazie Erica! Con Erica ho condiviso tutti i bei momenti di questi anni, sia lavorativi che extra. Ha affrontato con me le gioie e dolori della ricerca e mi ha dato appoggio nei momenti difficili. Spero che il futuro non ci dividerà.

Un grazie, infine, a Elena, alla mia famiglia e a mio marito Iari.